

# Effects of Assumed Tow Architecture on the Predicted Moduli and Stresses in Woven Composites

Clinton Dane Chapman  
*Texas A&M University*  
*College Station, Texas*

April 1994

Prepared for  
Lewis Research Center  
Under Grant NAG3-1270



National Aeronautics and  
Space Administration

**EFFECTS OF ASSUMED TOW ARCHITECTURE ON THE  
PREDICTED MODULI AND STRESSES IN WOVEN COMPOSITES**

**By**

**CLINTON DANE CHAPMAN**

**Texas A&M University**

**December 1993**



## **ACKNOWLEDGEMENTS**

**Funding for this research was provided by NASA Lewis Research Center, NASA Contract No. NAG3-1270 and by the Air Force Office of Scientific Research (AFOSR) under Grant No. F49620-93-1-0471.**

## TABLE OF CONTENTS

	Page
TITLE PAGE .....	
ACKNOWLEDGEMENT .....	
TABLE OF CONTENTS .....	i
LIST OF TABLES .....	iii
LIST OF FIGURES .....	iv
TITLE, AUTHOR, ABSTRACT .....	viii
 I. INTRODUCTION .....	 1
II. LITERATURE REVIEW .....	6
2.1 Analytic Models .....	7
2.2 Finite Element Work .....	10
III. THEORY .....	17
3.1 Nomenclature .....	17
3.2 Mesh Generation .....	21
3.2.1 Generation of 2D tow by translation of cross-section .....	21
3.2.2 Generation of 2D tow by extrusion of cross-section .....	23
3.2.3 The 90° tows .....	31
3.2.4 Cross-Sections .....	32
3.2.5 Generation of 3D translated tows .....	32
3.2.6 Generation of 3D extruded tows .....	35
3.2.7 Generation of Matrix .....	37
3.2.8 Variation of material properties .....	40
3.2.9 Parameters describing meshes .....	43
3.3 Boundary Conditions .....	46
3.3.1 Periodic boundary conditions of general unit cell .....	48
3.3.2 Extension .....	52

3.3.3 $\epsilon_{xz}$ shear .....	59
3.3.4 $\epsilon_{xy}$ shear .....	64
3.3.5 Savings due to unit cell reduction .....	69
3.4 Material Properties .....	70
3.5 Convergence Study .....	71
3.5.1 Elastic Properties .....	71
Translated Model .....	71
Extruded Model .....	76
3.5.2 Stress Distributions .....	79
3.6 Failure Criteria .....	84
IV. RESULTS AND DISCUSSION .....	88
4.1 Elastic Properties .....	88
4.2 Stress Distributions .....	94
4.2.1 $WR = 1/3$ .....	96
Loading in Warp Direction .....	96
XY Loading .....	105
XZ Loading .....	111
4.2.2 $WR = 1/6$ .....	114
Loading in Warp Direction .....	114
XY Loading .....	117
XZ Loading .....	123
4.2.3 $WR = 1/20$ .....	125
V. CONCLUSIONS .....	130
VI. FUTURE WORK .....	132
REFERENCES .....	133
VITA .....	135

## LIST OF TABLES

	Page
Table 3.1: Summary of periodic boundary conditions for the unit cell in Figure 3.15. ....	49
Table 3.2: CPU times and memory requirement for 111 translated model. ....	69
Table 3.3: Convergence of moduli with model type for translated model with single angle approximation and $WR = 1/3$ . ....	74
Table 3.4: Convergence of moduli with model type for translated model with multiple angle approximation and $WR = 1/3$ . ....	75
Table 3.5: Convergence of moduli with model type for extruded model with single angle approximation and $WR = 1/3$ . ....	77
Table 3.6: Convergence of moduli with model type for extruded model with multiple angle approximation and $WR = 1/3$ . ....	78

# LIST OF FIGURES

	Page
Figure 1.1: Typical plain weave composite unit cell modeled with finite elements with warp and fill tows indicated. ....	4
Figure 2.1: Five-harness satin modeled using mosaic model: (a) cross-sectional view of five-harness satin; (b) idealization using mosaic model. ....	8
Figure 2.2: Typical two dimensional fiber RVE showing parameters for fiber undulation model developed by Ishikawa and Chou [17]. ....	11
Figure 2.3: Quarter unit cell of plain weave textile composite used by Whitcomb [6]. ....	14
Figure 3.1: Cross-section of plain weave showing towpath and parameters used in waviness ratio. ....	19
Figure 3.2: Typical plain weave composite unit cell modelled with finite elements with warp and fill tows indicated as well as coordinate system used in this study. .	20
Figure 3.3: Solid objects created by translating and extruding a cross-section. ...	22
Figure 3.4: High waviness ratio translated tow showing unrealistic tow thicknesses through the tow. ....	24
Figure 3.5: Right triangles used to derive equations for extruded tows. ....	25
Figure 3.6: Parameters involved in the derivation of extruded tows. ....	28
Figure 3.7: Cross section of tow showing function for height, $h(x)$ . ....	33
Figure 3.8: Extruded tows with arrow indicating gap between warp and fill tows.	37
Figure 3.9: Cross-section of extruded tow showing that edge of perpendicular tow does not have same shape as cross-section. ....	39
Figure 3.10: Sectioned view of 1/8th subcell translated mesh showing how matrix is added to tows. ....	41

	Page
Figure 3.11: Sectioned view of 1/8th subcell extruded mesh showing how matrix in regions between tows is combined with rest of matrix. ....	42
Figure 3.12: Unit cells. ....	44
Figure 3.13: Basic building block of unit cells in Figure 3.12. ....	45
Figure 3.14: 1/32nd 243 translated model. ....	47
Figure 3.15: Unit cell used for derivation of boundary conditions. ....	50
Figure 3.16: 1/8th subcell used in derivation of boundary conditions. ....	57
Figure 3.17: 1/32nd subcell used in derivation of boundary conditions. ....	58
Figure 3.18: Meshes used in convergence study for translated tows. Elements are 3D 20-node hexahedrals. ....	72
Figure 3.19: Meshes used in convergence study for extruded tows. Elements are 3D 20-node hexahedrals. ....	733
Figure 3.20: Convergence of $\sigma_{xx}$ stress distributions in warp tows of translated meshes. Meshes were subjected to 1% $\epsilon_{xx}$ . ....	80
Figure 3.21: Comparison of multi-angle and single angle elements in translated 454 models subjected to 1% $\epsilon_{xx}$ strain. Notice that single angle model predicts non-zero stress at 'A'. ....	83
Figure 4.1: Variation of tow volume fraction with waviness ratio for extruded and translated models. ....	89
Figure 4.2: Meshes used for calculation of elastic properties. ....	91
Figure 4.3: Percent difference of translated tow prediction over extruded prediction of $E_x$ . ....	92
Figure 4.4: Percent difference of translated tow prediction over extruded prediction of $E_z$ . ....	92
Figure 4.5: Percent difference of translated tow prediction over extruded prediction of $G_{xy}$ . ....	93

Figure 4.6: Percent difference of translated tow prediction over extruded prediction of $G_{xz}$ . . . . .	93
Figure 4.7: Comparison of prediction of $v_{xy}$ by translated and extruded models. . . . .	95
Figure 4.8: Comparison of prediction of $v_{xz}$ by translated and extruded models. . . . .	95
Figure 4.9: Unit cell used for analysis of plain weave symmetrically stacked woven composite . . . . .	97
Figure 4.10: Comparison of Tsai-Hill failure criteria predicted with translated and extruded models after subjecting RVE to 1% $\epsilon_{xx}$ . . . . .	98
Figure 4.11: Comparison of $\sigma_{xx}$ in translated and extruded models after subjecting RVE to 1% $\epsilon_{xx}$ strain. . . . .	102
Figure 4.12: Comparison of $\sigma_{zz}$ distributions in warp tows after subjecting RVE to 1% $\epsilon_{xx}$ strain. . . . .	104
Figure 4.13: Comparison of Tsai-Hill failure criteria predicted with translated and extruded models for (a) tows and (b) resin after being subjected to a 1% $\epsilon_{xy}$ strain. . . . .	107
Figure 4.14: Comparison of normalized $\sigma_{xy}$ distributions in tows of translated and extruded models with $WR=1/3$ after being subjected to a 1% macroscopic $\epsilon_{xy}$ strain. . . . .	109
Figure 4.15: Comparison of normalized $\sigma_{xy}$ distributions in resin of translated and extruded models with $WR=1/3$ after being subjected to a 1% macroscopic $\epsilon_{xy}$ strain. . . . .	110
Figure 4.16: Comparison of normalized $\sigma_{yz}$ distributions in warp tows of translated and extruded models with $WR=1/3$ after being subjected to a 1% macroscopic $\epsilon_{xy}$ strain. . . . .	112
Figure 4.17: Comparison of predicted Tsai-Hill failure criteria for translated and extruded models with $WR=1/3$ after subjecting RVE to a 1% macroscopic $\epsilon_{xz}$ stain. . . . .	115
Figure 4.18: Comparison of predicted Tsai-Hill failure criteria for translated and extruded models with $WR=1/6$ after subjecting RVE to a 1% macroscopic $\epsilon_{xx}$ strain. . . . .	118

Figure 4.19: Comparison of predicted Tsai-Hill failure criteria for translated and extruded models with $WR=1/6$ after subjecting RVE to a 1% macroscopic $\epsilon_{xy}$ strain. ....	121
Figure 4.20: Comparison of normalized $\sigma_{yz}$ distributions in warp tows of translated and extruded models with $WR=1/6$ after subjecting RVE to a 1% macroscopic $\epsilon_{xy}$ strain. ....	124
Figure 4.21: Comparison of predicted Tsai-Hill failure criteria for translated and extruded models with $WR=1/6$ after subjecting RVE to a 1% macroscopic $\epsilon_{xz}$ strain. ....	126
Figure 4.22: Comparison of normalized $\sigma_{xz}$ distributions of translated and extruded models with $WR=1/6$ after subjecting RVE to a 1% macroscopic $\epsilon_{xz}$ strain. ....	128



# Effects of Assumed Tow Architecture on the Predicted Moduli and Stresses in Woven Composites

By

Clinton Dane Chapman

Texas A&M University

## ABSTRACT

This study deals with the effect of assumed tow architecture on the elastic material properties and stress distributions of plain weave woven composites. Specifically, the examination of how a cross-section is assumed to sweep-out the tows of the composite is examined in great detail. The two methods studied are extrusion and translation. This effect is also examined to determine how sensitive this assumption is to changes in waviness ratio. 3D finite elements were used to study a T300/Epoxy plain weave composite with symmetrically stacked mats. 1/32nd of the unit cell is shown to be adequate for analysis of this type of configuration with the appropriate set of boundary conditions. At low waviness, results indicate that for prediction of elastic properties, either method is adequate. At high waviness, certain elastic properties become more sensitive to the method used. Stress distributions at high waviness ratio are shown to vary greatly depending on the type of loading applied. At low waviness, both methods produce similar results.

## I. INTRODUCTION

As engineering technology continues to increase, more and more demands are placed upon structural materials in many industries, including, aerospace, automotive, and biomedical. Composites are designed in order to fulfill these demands. Fibrous composites are well established as being useful for many demanding structural applications. One method of fabricating fibrous composites is weaving. By grouping the individual fibers into fiber bundles called tows or yarns and weaving them together, preforms can be made in complex shapes. And with the addition of resin, woven composites are produced.

Woven composites have recently been receiving considerable attention due to their beneficial properties compared to laminated composites. Some of these properties include a high resistance to damage and impact [1]. These composites also exhibit a higher transverse moduli than their counterpart, the laminated composite [2]. Since the composites are woven they also exhibit a resistance to delamination which is a major failure mode for laminated composites. The contribution of these composites to manufacturing is also substantial. Due to their ease of handling woven composites reduce manufacturing error as well as provide the ability of *near-net-shape* manufacturing capability [3,4].

To design high performance composites, accurate techniques to predict the material properties of the composite must be developed [5]. Material property prediction can come

from experiments or analysis of the composite by analytical or numerical methods. Due to the immense amount of cost, material and man-power, that would be required in order to get the required properties using experimental methods, analysis of the composite using analytical or numerical methods presents the only cost effective way of predicting properties of woven composites.

Woven composites can be constructed in several different ways depending on how the tows are woven together. These types of weaves can be broken down into two general categories: Two-dimensional and three-dimensional. Some 2D weaves are plain, satin, and tri-axial weaves. The fabrication of three-dimensional composites is very complex. To avoid such complicated geometries, this research will be concerned with the simplest type of 2D textile composite, the plain weave.

As research continues on the analysis of woven composites, many researchers are assuming different cross sections in their analyses. Accurate description of the tow architecture is essential for predicting the mechanical behavior of textile composites [6]. The objective of this research is to determine the effect of assumed tow architecture on the predicted effective elastic properties of woven composites. Since an analysis of this type will require a detailed stress analysis of the composite it is not practical to analyze a complete structure due to the relative size of the structure compared with that of the microstructure. The alternative is to analyze a representative volume element (RVE) to obtain effective properties which can then be used in a structural analysis.

A substantial difficulty encountered when analyzing composites is the size of the inhomogeneities compared to the size of the RVE [7]. When studying unidirectional composites, the RVE can be reduced to a section of a single fiber in matrix material, but

for woven composites, to reduce the analysis to this minute a detail would so complicate the analysis that it would currently be futile to attempt. A larger RVE must be considered when dealing with woven composites. Since the physical size of the fibers is too fine to model these properties must be accounted for using a homogenization process.

Homogenization of the properties of the fiber tows can be performed using several techniques [9]. However, this homogenization must capture the transversely isotropic nature of the fiber tows. After homogenization, the tows can be idealized to any geometry which greatly simplifies the analysis.

Due to the highly complex geometry of the fiber tows inside woven composites which will be modeled in this analysis, it is difficult to model the RVE using analytical methods [2]. Instead, the finite element method will be used due to its ability to represent complex geometries and give detailed stress levels throughout the RVE. By employing traditional 3D finite elements, a detailed analysis will be performed to determine the effect of various geometrical assumptions on the behavior of the composite.

As stated earlier, this research is primarily concerned with the plain weave. A typical plain weave is shown in Figure 1.1 (the resin pockets have been omitted for clarity). This type of composite has only  $0^\circ$  and  $90^\circ$  tows which follow an undulating tow path. In this study, the warp and fill tows will be assumed to be identical. The warp tows run in the primary load carrying direction. For this study, the load carrying direction will be the  $x$  direction. The fill tows run perpendicular to them in the  $y$  direction.

Many cross-sections have been considered in the literature, including the Pierce geometry, race-track, and lenticular. For this research, the lenticular geometry will be



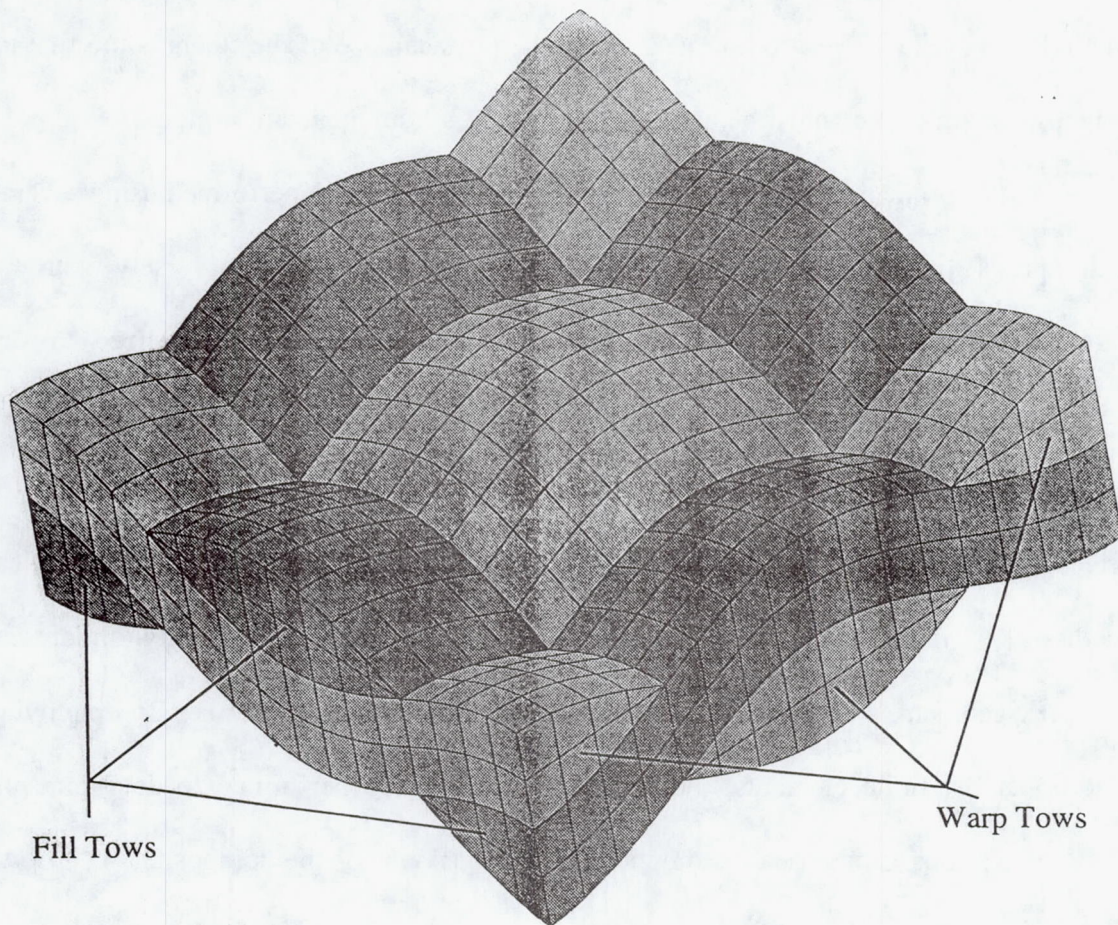


Figure 1.1: Typical plain weave composite unit cell modeled with finite elements with warp and fill tows indicated.



used. The complexity of the analysis is highly dependent on the assumptions made when describing the shape of the tows. Obviously, one does not want to model details which are insignificant. Since there are many assumptions which can be made about the geometry of the composite, these must be considered individually to determine their significance. The objective of this study is to determine the effect on moduli and stress distribution of how the cross-section is assumed to *sweep-out* the volume of the tow. A study of how this effect changes with waviness of the tows will also be considered.

Since the geometry of the unit cell is fairly complex, reduction of the unit cell due to symmetries in the RVE will be exploited to allow a more detailed analysis of the composite. Various load cases produce different boundary conditions and each will be developed in detail for various subcells of the unit cell.

This research will hopefully provide needed information which will help future researchers in the investigation of woven composites. To this end this research is presented in the following chapters.



## II. LITERATURE REVIEW

In the last twenty years, woven composites have received considerable attention due to their complex nature and beneficial properties. Modeling the behavior of woven composites is difficult because of their complex geometry, but it is this geometry which gives these composites their favorable properties.

The scale of woven composites compared to the scale of the fibers used in the tows of the composite is one difficulty in the analysis of woven composites. For finite element modeling it is impractical to try to model a woven composite with a resolution fine enough to capture individual fiber influence due to the enormous amounts of memory and computer time which would be required. One solution to this problem is to combine the properties of the resin and fibers in the tows. This process is known as homogenization. Homogenization theories assume that the scale of the microstructure is small compared to the size of the composite, and that the composite can be represented as an homogeneous medium [8]. Much work has been done on the homogenization of material properties including a text by Mura [9] which covers many applicable methods for homogenization of material properties for unidirectional composites. One particular method which presents an appealing solution due to its ease of implementation and reliable results is the Mori-Tanaka method.

The main focus of research on woven composites has been directed into prediction of effective moduli as well as stress analysis and failure prediction. There have been several attempts to predict effective properties using analytical methods with some relative success. Analytical methods have also been used to try to predict stress distributions with



little success due to the inadequate representation of the three-dimensional nature of these composites [2]. Finite elements have been employed by researchers to model this complex geometry. Several have used 2D and 3D finite element models to try to capture the effective moduli, stress distributions, and some predictions of failure.

Research done on textile composites can be broken down into two main categories: analytic and finite element work. A review of work in these two categories are presented in the following sections.

## 2.1 Analytic Models

Many analytic models were generated using classical laminated plate theory [10,11]. Ishikawa [12], Ishikawa and Chou [1,13-17], and Ishikawa *et al.* [18] have developed several models for the prediction of thermoelastic properties of woven composites using modifications of classical laminated plate theory [10,11], namely, the mosaic model, the fiber undulation model, and the bridging model.

The mosaic model [12,13,17] idealizes a woven composite as a collection of cross-ply laminates and is a simple means for estimating upper and lower bounds on the elastic constants of woven composites. Figure 2.1 shows a cross-section of a five-harness satin composite with its idealization using the mosaic model. As can be seen from the figure, the model ignores fiber undulation as well as fiber continuity. The mosaic model does however provide an upper and lower bounds depending on how the stress and strain are assumed to vary through the cross-ply laminates. The two extreme cases are constant stress and constant strain.



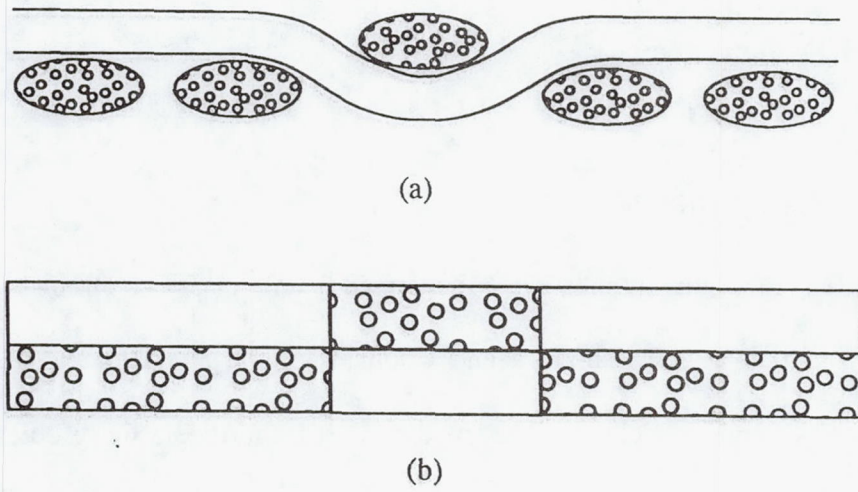


Figure 2.1: Five-harness satin modeled using mosaic model: (a) cross-sectional view of five-harness satin; (b) idealization using mosaic model.

Another model developed by Ishikawa and Chou [17] is the fiber undulation model. Unlike the mosaic model, the fiber undulation model takes into account the continuity and undulation of fibers by assuming that for each infinitesimal slice,  $dx$ , along the  $x$  axis as shown in Figure 2.2, classical laminated plate theory is germane. The compliance of each slice is a function of the amount of undulation which the fiber exhibits. These compliances are averaged along a representative length (See Figure 2.2) of composite and then inverted to give the overall stiffness of the composite.

The bridging model also developed by Ishikawa and Chou [1,16] is an extension of the crimp model to idealize satin weave composites. The representative unit cell of the satin composite is broken down into a region of undulation and several surrounding regions. Continuity and undulation of the warp tow is ignored in this model but is considered insignificant if the composite is loaded in the fill direction only. The stiffness of the undulating region is found using the fiber undulation model mentioned earlier. The stiffness of the surrounding region is found using classical laminated plate theory. By allowing a force to be exerted on the undulation region and the surrounding regions, an average compliance can be determined and then inverted to give an overall stiffness of the composite. The bridging model provides excellent agreement for graphite/epoxy composites when compared to experimental results [3].

In two papers by Naik and Shembekar [4,19], the authors extend the work of Ishikawa *et al.* [17] on the fiber crimp model to two dimensions. The authors present elastic analysis of plain weave textile lamina and laminates. They report large discrepancies using the 1D model, as reported in earlier literature, and fairly good results



using their developed 2D model. In-plane elastic moduli are found to agree well with experimental results. Laminate stacking and their offsets to one-another were also studied.

Ma *et al.* [25] developed a method of analyzing three dimensional composites by representing the composite with a brick like structure whose corners are connected with rods. Variation of elastic moduli with changes in fiber volume fraction as well as fiber spatial orientation were given in closed form expressions.

## 2.2 Finite Element Work

Three dimensional finite element work has only recently become more feasible due to the relatively inexpensive computer time and post analysis software for viewing the computed results of the analysis graphically. Consequently, most pre-90's analysis deals primarily with two dimensional finite element work.

Avery and Herakovich [20] studied two dimensional woven carbon-carbon composites. They used a quasi-three dimensional finite element model to represent the behavior of an eight harness satin in order to get an understanding of what effects the stress distribution in the composite. They predict how stress distributions in the fill and warp tows of the composite are affected by changes in the stacking sequence of the laminates. They also found that when the composite was subjected to in-plane loading, the stress distributions were highly sensitive to changes in the geometry. The authors state that the moduli in the region of undulation of the tows are dependent on the offset ratio and stacking sequence. (Offset ratio refers to the distance between the undulating

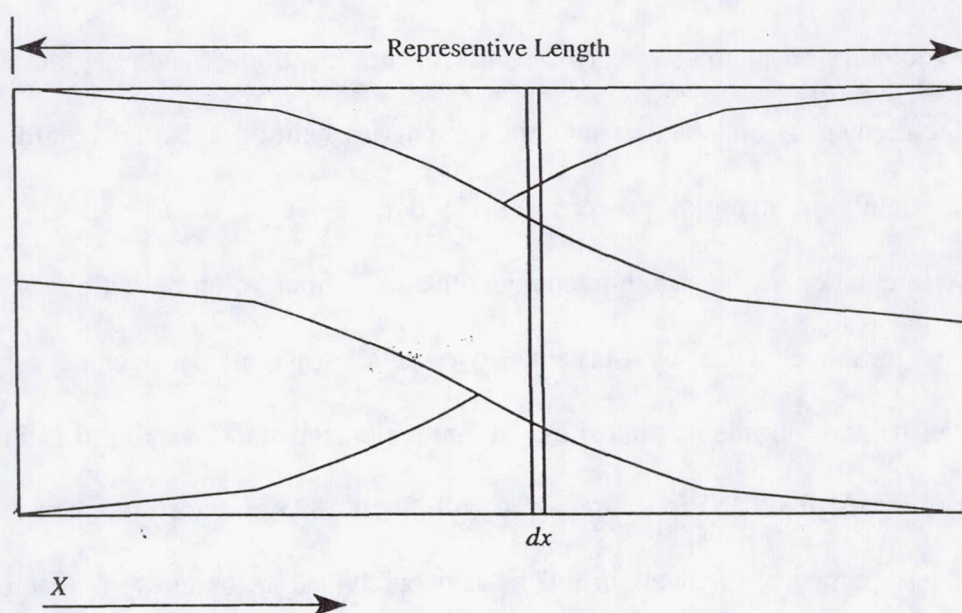


Figure 2.2: Typical two dimensional fiber RVE showing parameters for fiber undulation model developed by Ishikawa and Chou [17].



regions in different laminae.) The geometry changes considered by the authors are related to the stacking of the woven mats used to make the composite and not to the physical shape of the tows and tow paths.

Foye [21] performed a 3D analysis to determine the effective properties of woven composites. In this analysis, a 1/16th unit cell is modeled by one eight-node hexahedra. The geometry of the tows and cross-sections is not mentioned, and integration performed on the element is done across material boundaries with no apparent regard to the jump discontinuity in material properties. He does however report fair agreement with experimental data for a graphite/epoxy with a 64% fiber volume fraction for the weaves.

In a later paper by Masters, Foye, *et al.* [6] the same technique was used to model tri-axial braided composites. A finite element model was used to idealize a tri-axial braided AS-4 fabric impregnated with Shell 1895 epoxy resin. The results of the analysis compared as well or better than analytical techniques in predicting elastic properties of the composite when compared to experimental data. One analytical model used was a laminate model, which models each set of tows in the composite as if it were a symmetric laminate made from unidirectional plies. This model ignores any undulation of the tows. To account for this, another model, a corrected laminate model, applies a correction factor which can account for the braid undulation. The last model used for property prediction was the diagonal brick model as discussed previously [25].

Whitcomb [2] developed several techniques for performing three-dimensional finite element analysis of plain weave composites. This paper deals with aspects of analyzing these composites which are different from the traditional analysis of laminated



composites. Analysis of various plain weaves was performed to show the impact of tow waviness on the overall moduli and Poisson's ratios as well as strain distributions throughout the composite. The unit cell used by in his analysis is a quarter-unit cell as shown in Figure 2.3. This quarter-unit cell is small enough to allow more highly refined meshes than that of the full unit cell. Some results which Whitcomb found were that the in-plane moduli decreases almost linearly as tow waviness is increased. Also, when the plain weave composite is subjected to uniaxial loading, large normal and shear strains developed due to tow waviness.

Woo and Whitcomb [2], Whitcomb and Woo [5], and Whitcomb *et al.* [23] developed new macro elements which account for the spatial variation of material properties within a single element in order to simplify 3D analysis of textile composites. These elements are particularly useful for analyzing a woven composite with finite dimension because it reduces the amount of memory required to analyze the model. The disadvantage to using macro elements is that macro elements can only model small number of degrees of freedom compared to that of the full finite element mesh. Although these degrees of freedom can effectively model the stiffness of the composite, stresses in the element are erroneous near the edges of the elements. However, away from the edges of the macro elements, Woo [8] reports very close agreement with standard finite element results.

Paumelle *et al* [24] presented an analysis of woven composites by homogenization of the fibers and resin to get tow properties and then homogenizing the tows and resin to get composite properties. Stresses induced inside the woven composite microstructure

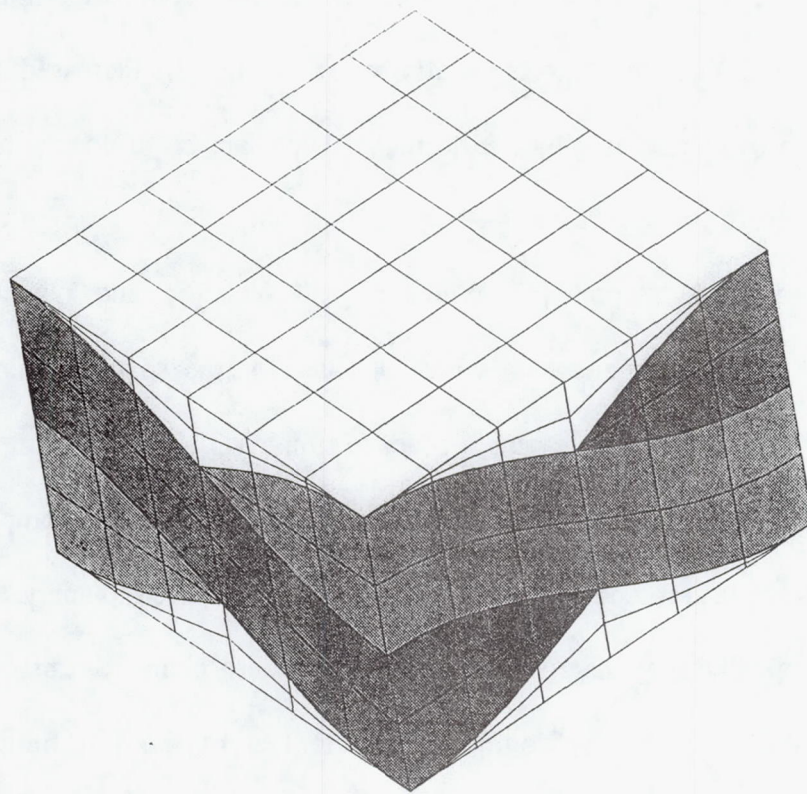


Figure 2.3: Quarter unit cell of plain weave textile composite used by Whitcomb [6].



were calculated using three dimensional finite elements. This analysis was performed on a balanced glass fabric embedded in an epoxy resin. The primary goal of their study was to reveal the over stresses of the materials in the composite as well as point out the problem of delamination at the yarn-matrix interface. They point out in their investigation that the over stresses induced in the composite can be as much as 7.8 times the macroscopic loading. They also contend that the resin undergoes the maximum loading relative to its strength and that failure will initiate there.

In an earlier study [7], Paumelle *et al* presented results which reflect the effect of geometry changes on the effective properties. The geometry effects considered were:

1. Distance between yarns which is analogous to waviness ratio.
2. Shape of yarn section which reflects the flatness or circularity of the cross section.
3. Fiber content of the tows.
4. Resin thickness between layers of fabric.

The authors make several conclusions based on their study. They observe that the Young's modulus of the resin greatly affects the values of  $E_z$ ,  $G_{xz}$ , and  $G_{yz}$ . Also, the remark that a readjustment of the yarn shape could increase the shear modulus of the composite.

Woo [8] studied woven composite using two dimensional and three dimensional finite elements. The author's research dealt with the study of two types of macro elements: single-field and multi-field. A comparison of results obtained with these special elements was compared to conventional finite elements. Also, work was



performed to determine initial points of failure in the composite as well as some work on the prediction of elastic properties and their variation with waviness-ratio. The material system used by Woo was a T300 graphite fiber in an epoxy matrix. Since Woo's work contains work which is initially closely related to this research, these material properties will be used in all analysis in this thesis.

### III. THEORY

This chapter contains relevant theory related to plain weave composites. The purpose of this chapter is to give the reader a better understanding of woven composites and explain how and why certain results were obtained. A description of various terms related to woven composites will be covered in the following section. After this description, mesh generation will be covered to explain the theory involved in the generation of the finite element meshes used for this research. Next, application of loads to the meshes will be covered along with the appropriate boundary conditions for the RVE's used in this research.

#### 3.1 Nomenclature

A woven composite like conventional fiber composites is made of a matrix material surrounding fibers. However, the fibers in a woven composite are twisted into a dense fiber bundle called a *tow* which can be combined with other tows to make a textile. After the addition of resin, the tow contains resin and fibers. The fiber properties can be homogenized with the resin to give effective properties of the tow. These homogenized properties can be found using micromechanics. For a plain weave, there are two different names for the tows - *warp* and *fill*. The warp tows run in the primary load carrying direction, and the fill tows run perpendicular to them.

The tow is characterized by a *tow path* which is a description of how the midplane of the tow changes with position. The tow path of a typical tow is shown



in Figure 3.1. The tow path is the most important feature in describing a woven composite. It will be shown later that by specifying a tow path, many parameters which further describe the tows can be found. For this study, only sinusoidal paths will be considered.

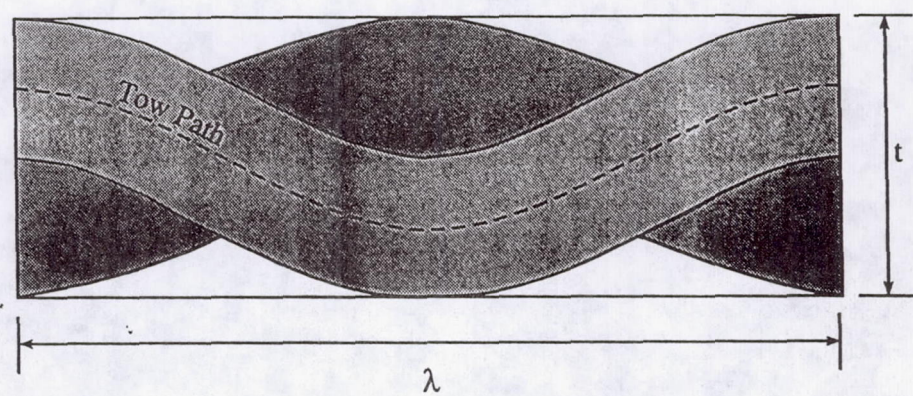
The tows of a composite are characterized not only by the tow path but by a parameter referred to as *waviness ratio* (*WR*). Waviness ratio is - as the name suggests - a measure of the waviness of a tow. It is more specifically, the ratio of the thickness of the mat to the wavelength of the tow path. Or in equation form

$$WR = \frac{t}{\lambda} \quad 3.1.1$$

where  $t$  is the thickness of the woven mat and  $\lambda$  is the wavelength of the towpath (see Figure 3.1).

Tows can be woven together in many ways. The one that this research is concerned with is the plain weave. This type of weave has only  $0^\circ$  and  $90^\circ$  tows which follow an undulating tow path. A typical plain weave is shown in Figure 3.2. In this study, the warp and fill tows are assumed to be identical. This is type of configuration is known as a balanced weave.

Several other terms describing the assumed geometry are also utilized, but these are better addressed in the following section on mesh generation.



$$WR = t/\lambda$$

Figure 3.1: Cross-section of plain weave showing towpath and parameters used in waviness ratio.



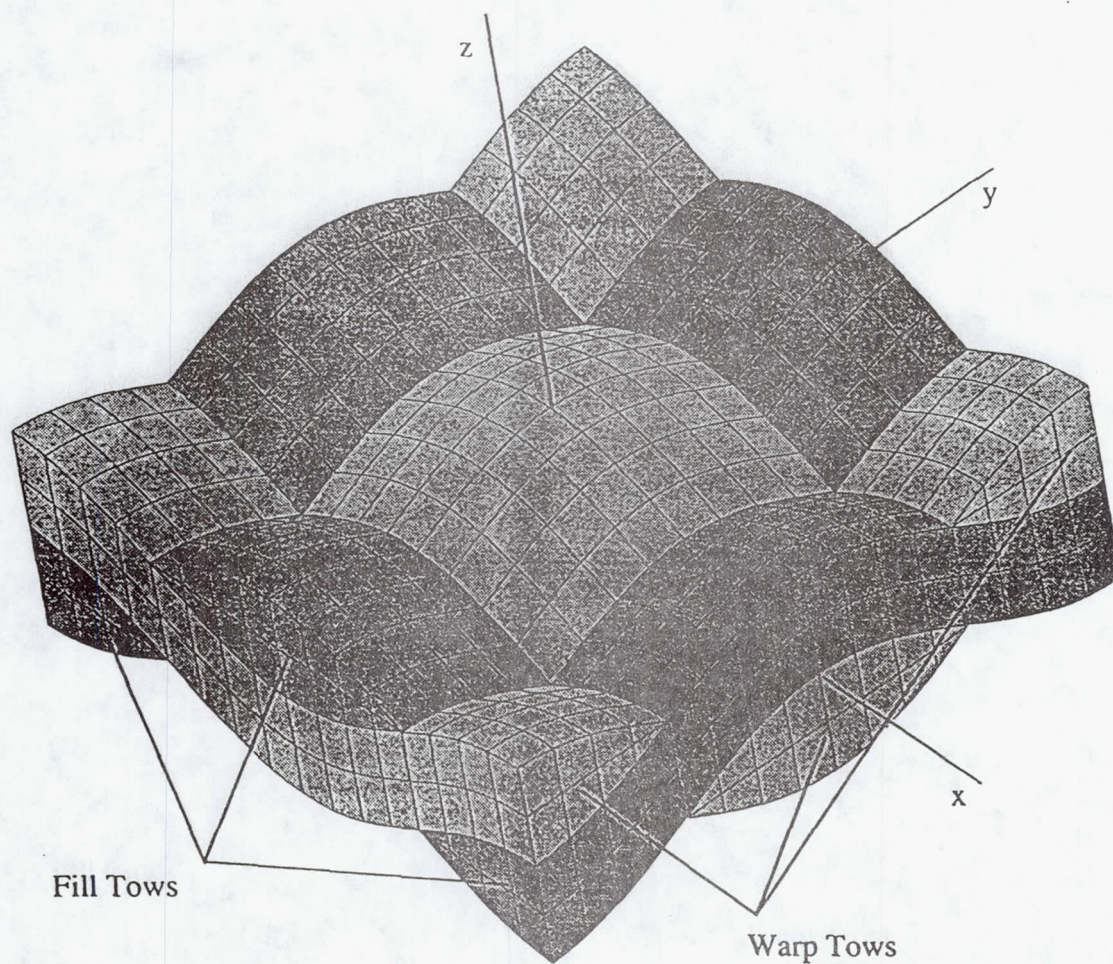


Figure 3.2: Typical plain weave composite unit cell modelled with finite elements with warp and fill tows indicated as well as coordinate system used in this study.



## 3.2 Mesh Generation

In order to determine the effect of geometry on the effective properties and stress distributions, a mesh generation strategy must be developed in order to automate the tedious task of mesh generation. Since the geometry of woven composites are rather unique, the generation strategy must be consistent with the geometry of the tows. The following section details the development of meshes used in this thesis. To generate three dimensional meshes, an understanding of the generation of simpler two dimensional meshes is beneficial. Therefore, mesh generation for 2D models will be discussed first, then generation of 3D models will be addressed.

### 3.2.1 *Generation of 2D tow by translation of cross-section*

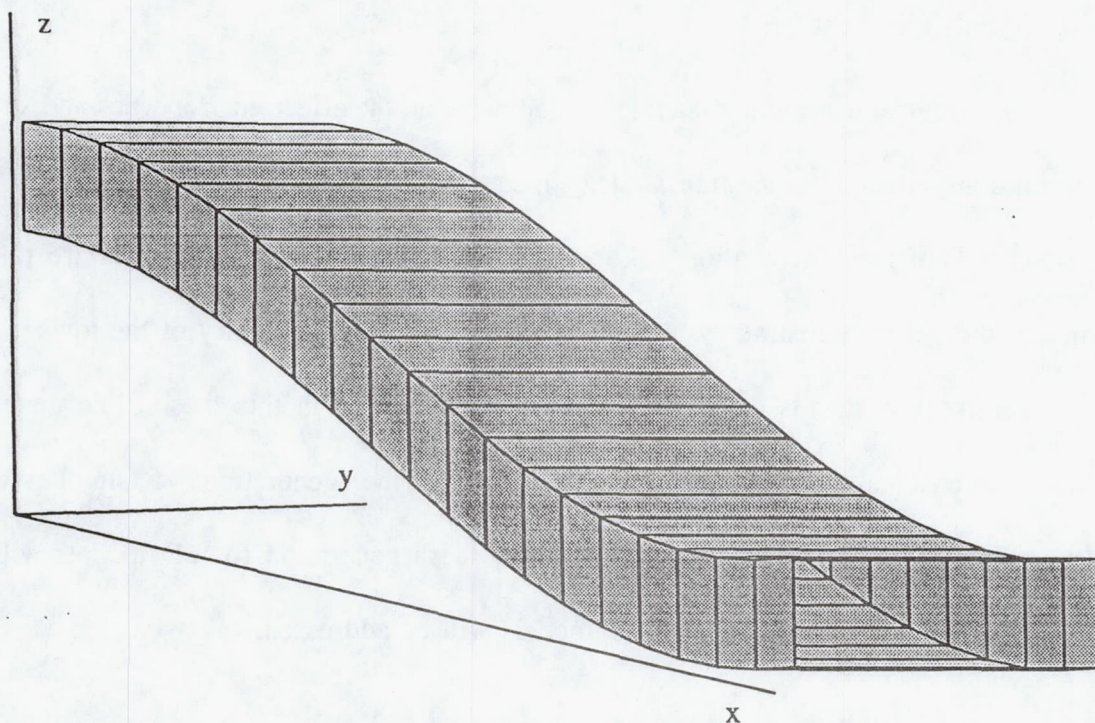
Translated tows are the simplest to generate and understand. The term translated actually refers to the way a representative cross-section is used to generate a solid object (see Figure 3.3(a)). For 2D models, it physically means the distance above and below the tow path is kept a constant. For a tow path described by the function  $f(x)$ , the top and bottom of the tow are given by  $f(x) \pm h/2$  where  $h$  is the height of the fiber tow. Knowing this, generation of elements for the tow can be done by simply using this functions to pick off values for the top and bottom. For example, if the tow path is described by

$$f(x) = \sin(x)$$

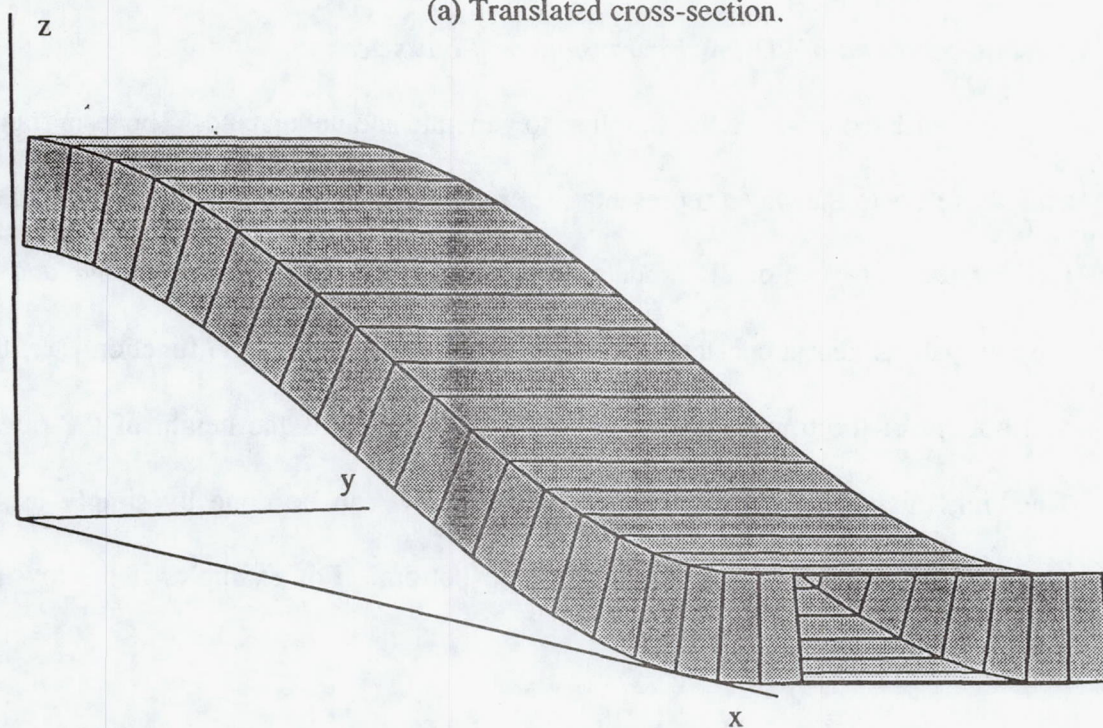
3.2.1

and has a height of  $h=2$ , then the top and bottom are described by the functions





(a) Translated cross-section.



(b) Extruded cross-section.

Figure 3.3: Solid objects created by translating and extruding a cross-section.



$$g_T(x) = f(x) + 1 = \sin(x) + 1$$

$$g_B(x) = f(x) - 1 = \sin(x) - 1$$
3.2.2

respectively, where the subscripts 'T' refers to the top and 'B' to the bottom of the tow. The coordinates for the top and bottom of a translated tow is represented by a function which is no more complicated than that which describes the tow path.

The translated tow does have one major drawback, distortion of the tow at high waviness ratios. For example, a tow path described by the function

$$f(x) = \sin\left(\frac{\pi}{x}\right)$$
3.2.3

with a height of 2, has a  $WR=1$ . This tow is shown in Figure 3.4. The thickness of the tow is dramatically smaller near 'A' than at 'B' as indicated by the arrows. This is physically inaccurate because the tow still contains the same amount of fibers so should be the same width at 'A' and 'B'. A better way would be to keep the thickness perpendicular to the tow path constant. This method of generation will be termed extruded.

### 3.2.2 Generation of 2D tow by extrusion of cross-section

As stated above, the extruded tow is generated by keeping a constant distance perpendicular to the tow path. Figure 3.3(b) illustrates how a representative cross-section is used to generate a solid model. Functions for the top and bottom of the tow



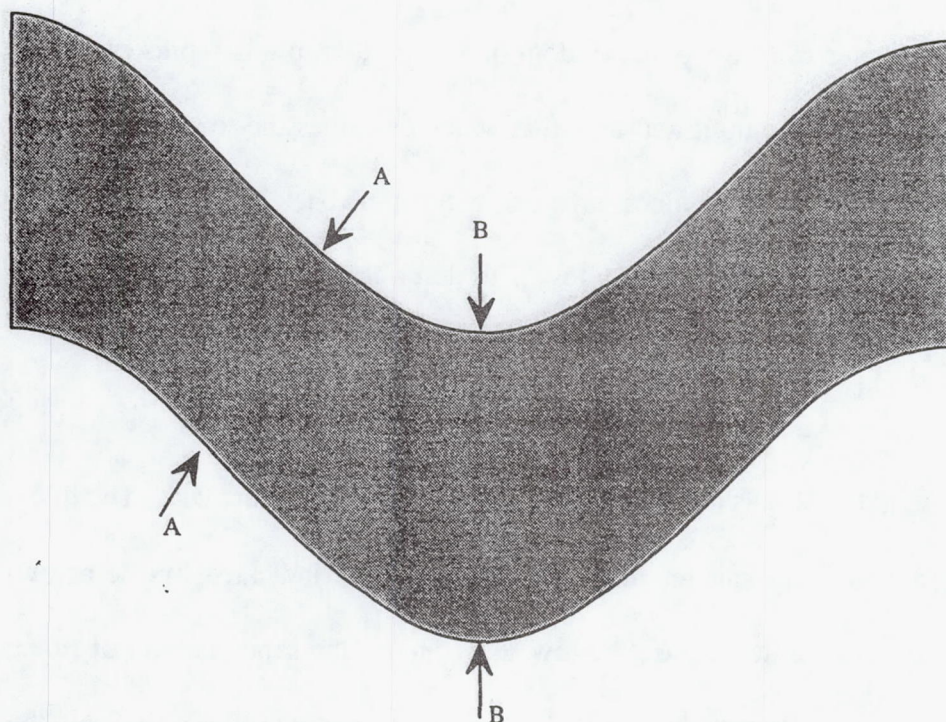


Figure 3.4: High waviness ratio translated tow showing unrealistic tow thicknesses through the tow.



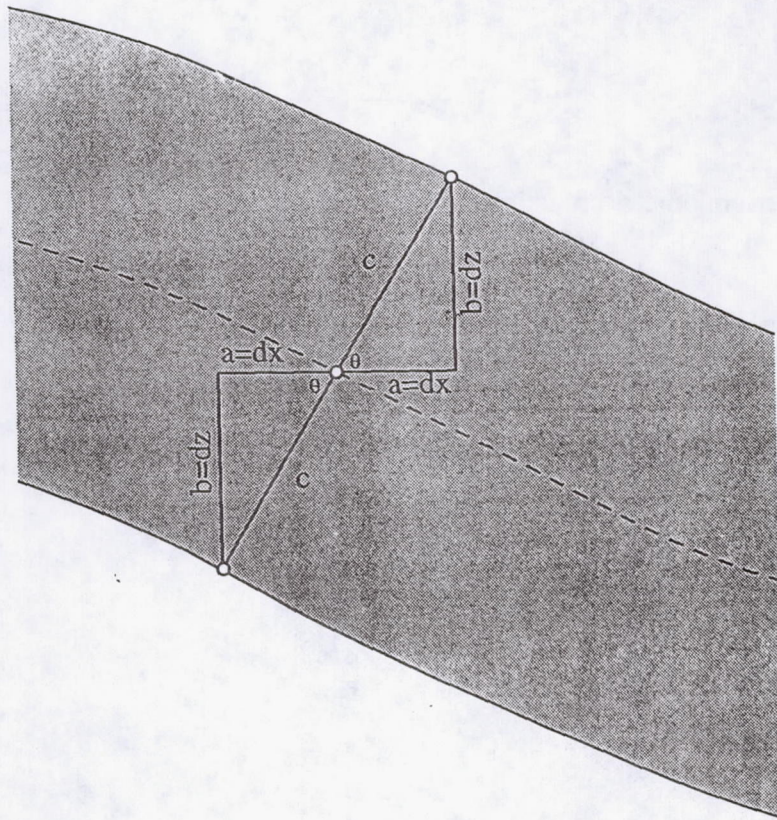


Figure 3.5: Right triangles used to derive equations for extruded tows.



can be derived using the Pythagorean Theorem with the triangle shown in Figure 3.5,

$$a^2 + b^2 = c^2 \quad 3.2.4$$

Dividing by  $a^2$  gives

$$1 + \frac{b^2}{a^2} = \frac{c^2}{a^2} \quad 3.2.5$$

Rewriting using trigonometric functions for the r.h.s. gives

$$1 + \left(\frac{b}{a}\right)^2 = \frac{1}{\cos^2 \theta} \quad 3.2.6$$

here  $\theta$  is the angle opposite side  $b$ . Setting  $a=dx$  and  $b=dz$  as shown in Figure 3.5 gives

$$1 + \left(\frac{dz}{dx}\right)^2 = \frac{1}{\cos^2 \theta} \quad 3.2.7$$

or, using  $z=f(x)^{\dagger}$  gives

$$1 + f'(x)^2 = \frac{1}{\cos^2 \theta} \quad 3.2.8$$

Solving for  $\cos \theta$  gives

$$\cos \theta = \frac{1}{\sqrt{f'(x)^2 + 1}} \quad 3.2.9$$

---

<sup>†</sup> $z$  is used so that transition to the discussion of 3D mesh generation will be made simpler.

Similarly, an equation for  $\sin\theta$  can be derived and is given by

$$\sin\theta = \frac{f'(x)}{\sqrt{f'(x)^2 + 1}} \quad 3.2.10$$

Using the above relations for  $\sin\theta$  and  $\cos\theta$ , it is possible to obtain values for  $\Delta x_T$ ,  $\Delta z_T$ ,  $\Delta x_B$ , and  $\Delta z_B$  as shown in Figure 3.6. These relations in terms of  $f(x)$  and  $h$  as shown in Figure 3.6 are

$$\Delta x_T = -\frac{h}{2} \frac{f'(x)}{\sqrt{f'(x)^2 + 1}} \quad 3.2.11$$

$$\Delta z_T = \frac{h}{2} \frac{1}{\sqrt{f'(x)^2 + 1}} \quad 3.2.12$$

$$\Delta x_B = \frac{h}{2} \frac{f'(x)}{\sqrt{f'(x)^2 + 1}} \quad 3.2.13$$

$$\Delta z_B = -\frac{h}{2} \frac{1}{\sqrt{f'(x)^2 + 1}} \quad 3.2.14$$

Adding these relations to  $x$  and  $z=f(x)$  gives

$$x_T(x) = x - \frac{h}{2} \frac{f'(x)}{\sqrt{f'(x)^2 + 1}} \quad 3.2.15$$

$$z_T(x) = f(x) + \frac{h}{2} \frac{1}{\sqrt{f'(x)^2 + 1}} \quad 3.2.16$$



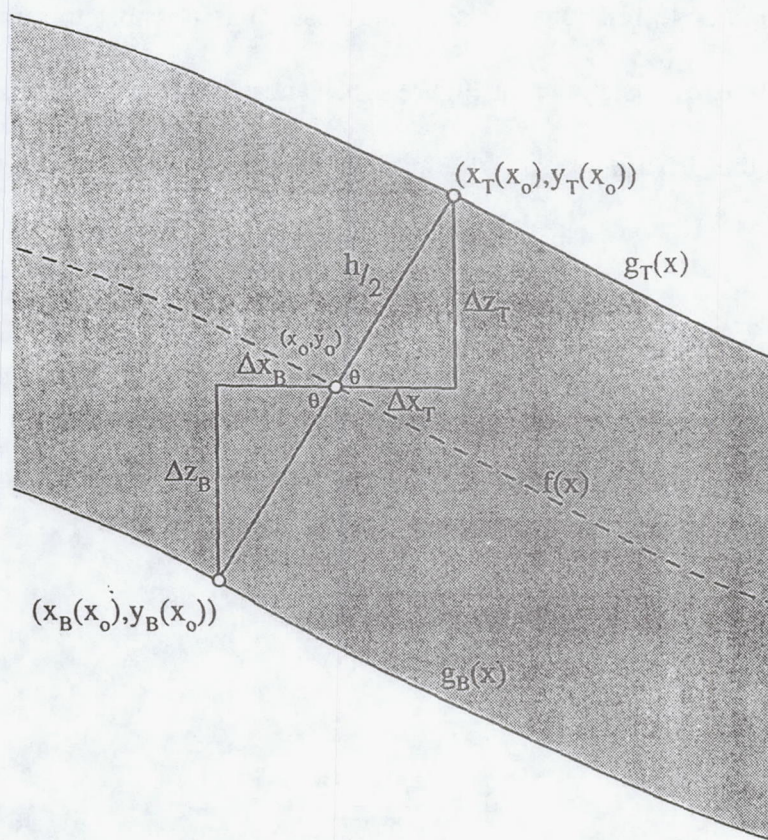


Figure 3.6: Parameters involved in the derivation of extruded tows.

$$x_g(x) = x + \frac{h}{2} \frac{f'(x)}{\sqrt{f'(x)^2 + 1}} \quad 3.2.17$$

$$z_g(x) = f(x) - \frac{h}{2} \frac{1}{\sqrt{f'(x)^2 + 1}} \quad 3.2.18$$

To obtain an equation,  $g_T(x)$ , which describes the top surface of the tow, one must first recognize that

$$f'(x) = g_T'(x_T) \quad 3.2.19$$

as shown in Figure 3.6. Starting with

$$g_T(x_T) = z_T(x) = f(x) + \frac{h}{2} \frac{1}{\sqrt{f'(x)^2 + 1}} \quad 3.2.20$$

Substituting (3.2.19) into (3.2.20) gives

$$g_T(x_T) = f(x) - \frac{h}{2} \frac{1}{\sqrt{g_T'(x_T)^2 + 1}} \quad 3.2.21$$

Solving for  $x$  in (3.2.15) and substituting in (3.2.19) gives

$$x = x_T + \frac{h}{2} \frac{g_T'(x_T)}{\sqrt{g_T'(x_T)^2 + 1}} \quad 3.2.22$$

Finally, substituting (3.2.22) into (3.2.21) gives

$$g_T(x_T) = f\left(x_T + \frac{h}{2} \frac{g_T'(x_T)}{\sqrt{g_T'(x_T)^2 + 1}}\right) - \frac{h}{2} \frac{1}{\sqrt{g_T'(x_T)^2 + 1}} \quad 3.2.23$$

It is cumbersome to solve this highly complicated equation for  $g_T(x)$  to determine points on the tow path. An approximate solution can be obtained by fitting a spline through points generated using equations (3.2.15)-(3.2.18) and then evaluating the spline along the path. This spline technique was used herein.

As with translated tows, extruded tows have disadvantages. Half the height of a translated tow cannot exceed the radius of curvature of the tow path or the formulation for  $g_T(x)$  will become multivalued. The radius of curvature,  $\rho$ , for a function  $f(x)$  is given by

$$\rho = \frac{(1 + f'(x)^2)^{\frac{3}{2}}}{|f''(x)|} \quad 3.2.24$$

which gives the condition

$$\frac{h}{2} < \rho \quad 3.2.25$$

If a tow path is described by the function

$$f(x) = \cos\left(\frac{2\pi}{\lambda}x\right) \quad 3.2.26$$

with a height of 2, the waviness-ratio is

$$WR = \frac{4}{\lambda} \quad 3.2.27$$

Substituting (3.2.26) and (3.2.24) into (3.2.25) gives

$$1 < \frac{\left(1 + \left(-\frac{2\pi}{\lambda} \sin\left(\frac{2\pi}{\lambda} x\right)\right)\right)}{\left|\left(\frac{2\pi}{\lambda}\right)^2 \cos\left(\frac{2\pi}{\lambda} x\right)\right|} \quad 3.2.28$$

The r.h.s. is minimum when  $x = \lambda$  which gives

$$1 < \left(\frac{\lambda}{2\pi}\right) \quad 3.2.29$$

This condition is false for  $\lambda < 2\pi$ . This implies that  $WR$  cannot exceed  $4/2\pi$  for an extruded tow with this particular combination of tow path and height. This is important to know because it implies that the height of a tow has a maximum value for a specific tow path.

### 3.2.3 The 90° tows

So far all that has been discussed is generation of one tow which will be termed the 0° tow. The tows running perpendicular to the 0° tows will be designated as the 90° tows. If one assumes that the 0° and 90° tows have the same tow path, then a maximum height of the tow can be found. The height,  $h$ , of the tows is given mathematically as

$$h = \max(f(x)) - \min(f(x)) \quad 3.2.30$$

This equation assumes that the minimum of the 90° tows occurs at the maximum of the 0° tows and vice versa - which is the case for plain weaves. The thickness of the mat may also be found and is given by



$$t=2h$$

3.2.31

With this it is possible to proceed to the development of the cross-section of the 90° tows.

### 3.2.4 Cross-Sections

The cross section of the 90° tows is determined by the tow path of the 0° tows. There are an infinite number of different cross-section shapes which can conform to this statement. However, it is important to consider what constrains the cross-section shape in order to get a maximum area cross-section shape. Since both the 0° and 90° tows always want to straighten after being woven together, they are forced to contact. As a simplifying assumption, if the cross-section is assumed to be constant along the tow path, then the shape is constrained and only one maximum area cross-section exists. The cross-section generated by way of this assumption is symmetric about the mid-plane of the tow. This means that the distance from the mid-plane to the top is the same as the distance from the mid-plane to the bottom of the tow. The cross-section can then be represented by a function  $h(x)$  which gives the distance from the lower surface to the upper surface of the cross-section. Consequently, the distance from the mid-plane to either the top or bottom of the cross-section is just  $h(x)/2$  (see Figure 3.7).

### 3.2.5 Generation of 3D translated tows

After the cross-section has been determined, generation of 3D tows is possible. The top and bottom of a single 0° translated tow are created using a formula similar to

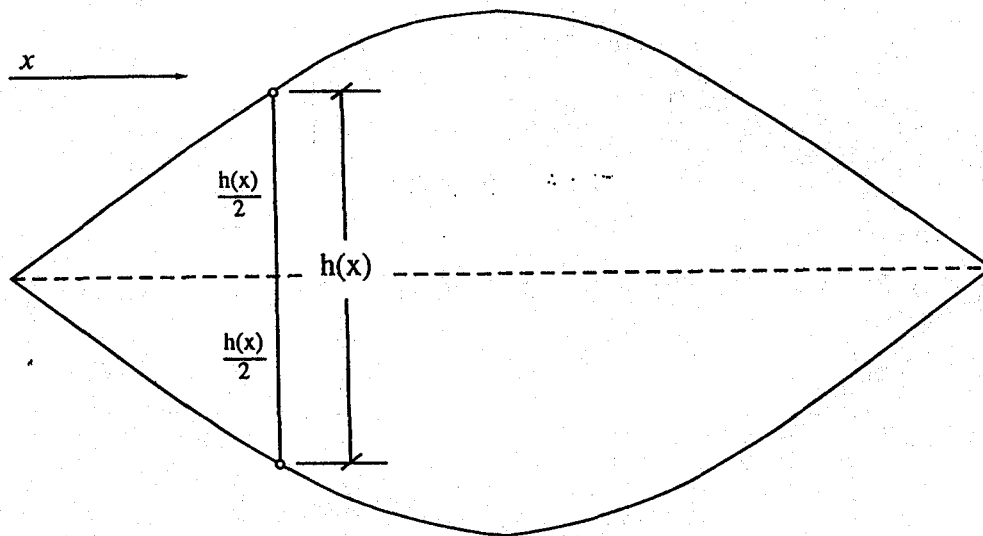


Figure 3.7: Cross section of tow showing function for height,  $h(x)$ .

that used in 2D (eq. (3.2.2)),

$$\begin{aligned} g_{T0}(x,y) &= f(x) + \frac{h(y)}{2} \\ g_{B0}(x,y) &= f(x) - \frac{h(y)}{2} \end{aligned} \quad 3.2.32$$

Notice that the only difference is that  $h$  is now a function  $y$ . (The '0' in the subscript on  $g$  refers to the  $0^\circ$  tow.) Coordinates defining the surface of a translated tow may be picked easily using the above formulas. The tow path of adjacent  $0^\circ$  tows for a plain weave are offset in the  $x$  direction by  $\lambda/2$ . This gives the following equations for adjacent  $0^\circ$  tows:

$$\begin{aligned} g_{T0}(x,y) &= f\left(x + \frac{\lambda}{2}\right) + \frac{h(y)}{2} \\ g_{B0}(x,y) &= f\left(x + \frac{\lambda}{2}\right) - \frac{h(y)}{2} \end{aligned} \quad 3.2.33$$

The  $90^\circ$  tows may also be added by using the above formula and making a change of variable (ie. switching  $x$  and  $y$ ).

$$\begin{aligned} g_{T90}(x,y) &= f(y+c) + \frac{h(x+r)}{2} \\ g_{B90}(x,y) &= f(y+c) - \frac{h(x+r)}{2} \end{aligned} \quad 3.2.34$$

To insure compatibility between the  $0^\circ$  and  $90^\circ$  tows,  $c$  and  $r$  have been added to the previous equation. An example may clarify the meaning of  $c$  and  $r$ .



*Example:* If a tow path is given by

$$f(x) = A \cos\left(\frac{2\pi x}{\lambda}\right) \quad 3.2.35$$

Then the top and bottom surface of the 0° and 90° tows are described by

$$g_0(x,y) = A \cos\left(\frac{2\pi x}{\lambda}\right) \pm \frac{h(y)}{2} \quad 3.2.36$$

and

$$g_{90}(x,y) = A \cos\left(\frac{2\pi(y+c)}{\lambda}\right) \pm \frac{h(x+r)}{2} \quad 3.2.37$$

At  $(x,y) = (0,0)$ ,  $g_{00}(0,0)$  should equal  $g_{T90}(0,0)$ . So to insure this,  $c$  and  $r$  should be given the values

$$c = \frac{\lambda}{2}, r = 0. \quad 3.2.38$$

Next, generation of 3D extruded tows will be covered. Compatibility will be enforced in the same way as it is for the translated tows above.

### 3.2.6 Generation of 3D extruded tows

The extension from 2D to 3D is also not difficult for extruded tows. The main difficulty is an increase in the amount of data which must be kept. Using equations (3.2.15)-(3.2.18) and substituting a function in for  $h$  which describes the cross-section, the following equations are produced

$$x_T(x,y) = x - \frac{h(y)}{2} \frac{f'(x)}{\sqrt{f'(x)^2 + 1}} \quad 3.2.39$$

$$z_T(x,y) = f(x) + \frac{h(y)}{2} \frac{1}{\sqrt{f'(x)^2 + 1}} \quad 3.2.40$$

$$x_B(x,y) = x + \frac{h(y)}{2} \frac{f'(x)}{\sqrt{f'(x)^2 + 1}} \quad 3.2.41$$

$$z_B(x,y) = f(x) - \frac{h(y)}{2} \frac{1}{\sqrt{f'(x)^2 + 1}} \quad 3.2.42$$

Again, it may be possible to obtain equations describing the top and bottom surface of the tow, but these equations will be highly non-linear and difficult to solve. Using a two-dimensional spline fit or collections of 1D splines, it is possible to obtain an approximate function for the upper and lower surface of the tows.

In the above equations, (3.2.39)-(3.2.42),  $h(y)$  has been included. This function for the cross-section of the tow must also be approximated using splines. Using all of these splines means that a substantial amounts of "book-keeping" must be performed in a mesh generation program.

To obtain equations describing the  $0^\circ$  tows adjacent to the single  $0^\circ$  tow, an offset of  $\lambda/2$  must be added to  $x$  as shown in the translated section previously. The equations describing the  $90^\circ$  tows can also be generated similar to the translated section using the constants  $c$  and  $r$ .



Several extruded tows are shown in Figure 3.8. As indicated by the arrow in the figure, there exists a gap between the  $0^\circ$  and  $90^\circ$  tows. This gap is not present with the translated tows. The gap exists between the extruded tows because the edges of the perpendicular tows, which are the same as the tow path of the perpendicular tow, do not have the same shape as the cross-section of the tow where the two tows should meet. This is shown in Figure 3.9. This is not true for the translated tows whose cross-section shape is the same as the part of the tow path in contact.

### 3.2.7 *Generation of Matrix*

After generating the tows using any method, all that remains is to generate the matrix elements. Generation of the matrix elements for the translated model is fairly simple to accomplish. This is done by breaking the matrix into two regions - one above the tows and one below the tows - and generating each region separately. For the upper region, the containing surfaces are the top of the tows and a plane where  $z = \text{constant}$ . The elements are created by just picking off points from the upper plane and top of the tows and then dividing the region into the number of desired elements. A 1/8th subcell translated mesh which has been sectioned is shown in Figure 3.10.

For the extruded model, this strategy is all right if the matrix elements being created are above or below two tows. But the extruded model has a few surprises. There exists a matrix pocket between the warp and fill tows as shown in Figure 3.8 and Figure 3.9. Elements must be created for this region also, and additionally, must be



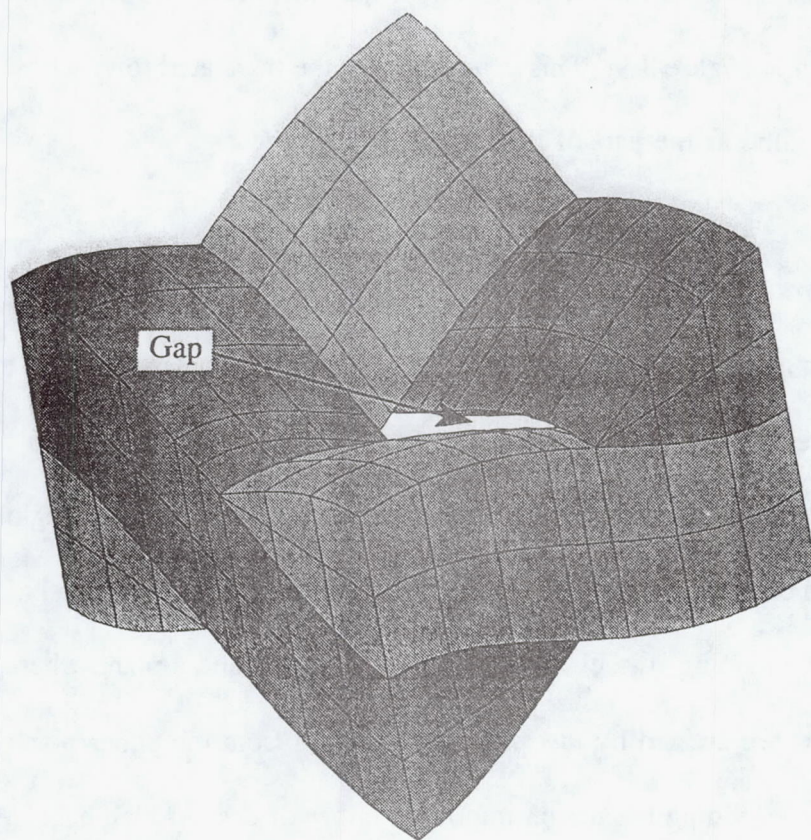


Figure 3.8: Extruded tows with arrow indicating gap between warp and fill tows.



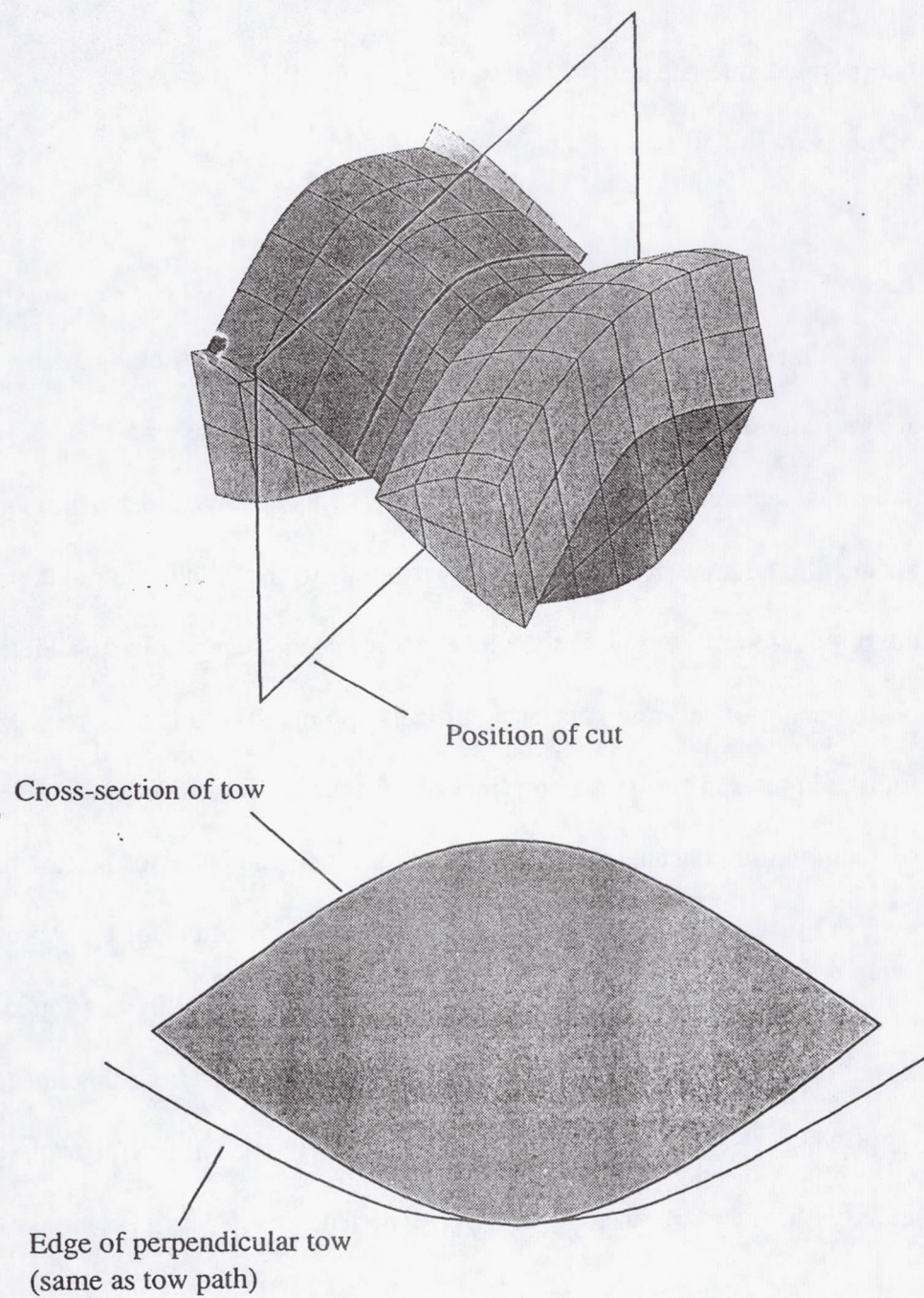


Figure 3.9: Cross-section of extruded tow showing that edge of perpendicular tow does not have same shape as cross-section.



incorporated into the rest of the matrix. Figure 3.11 shows a seperated 1/8th subcell extruded mesh and one possible way to do this.

### 3.2.8 Variation of material properties

The material properties of the tows can be found by homogenizing the properties of the individual fibers with the resin. These properties can then be applied to the individual elements representing the tows of the composite. Although, the tow is assumed to be homogeneous and transversely isotropic in the material coordinate system, the orientation of the tow in the global coordinate system varies considerably depending on the angle of the tow path at a particular point. The angle of rotation for the warp translated tows is constant along lines of constant  $x$ . For the warp extruded tows, angles of rotation are constant along lines which are perpendicular to the tow path.

For this research, the variation of angles of rotation for the warp extruded tows will be assumed to vary linearly along lines of constant  $x$ . It was found that the actual variation of the angle across the tow varied less than  $0.5^\circ$  from this linear fit at a  $WR = 1/3$ . This is assumed to be a small effect and will add little error to the analysis. Unit cells with lower waviness ratios will experience even less deviation from the correct angle.

For each element two methods of specifying the angles for the elements will be studied for initial analysis. One method assume a constant rotation angle for an entire element. This will be referred to as the *single angle* method. The next method allows



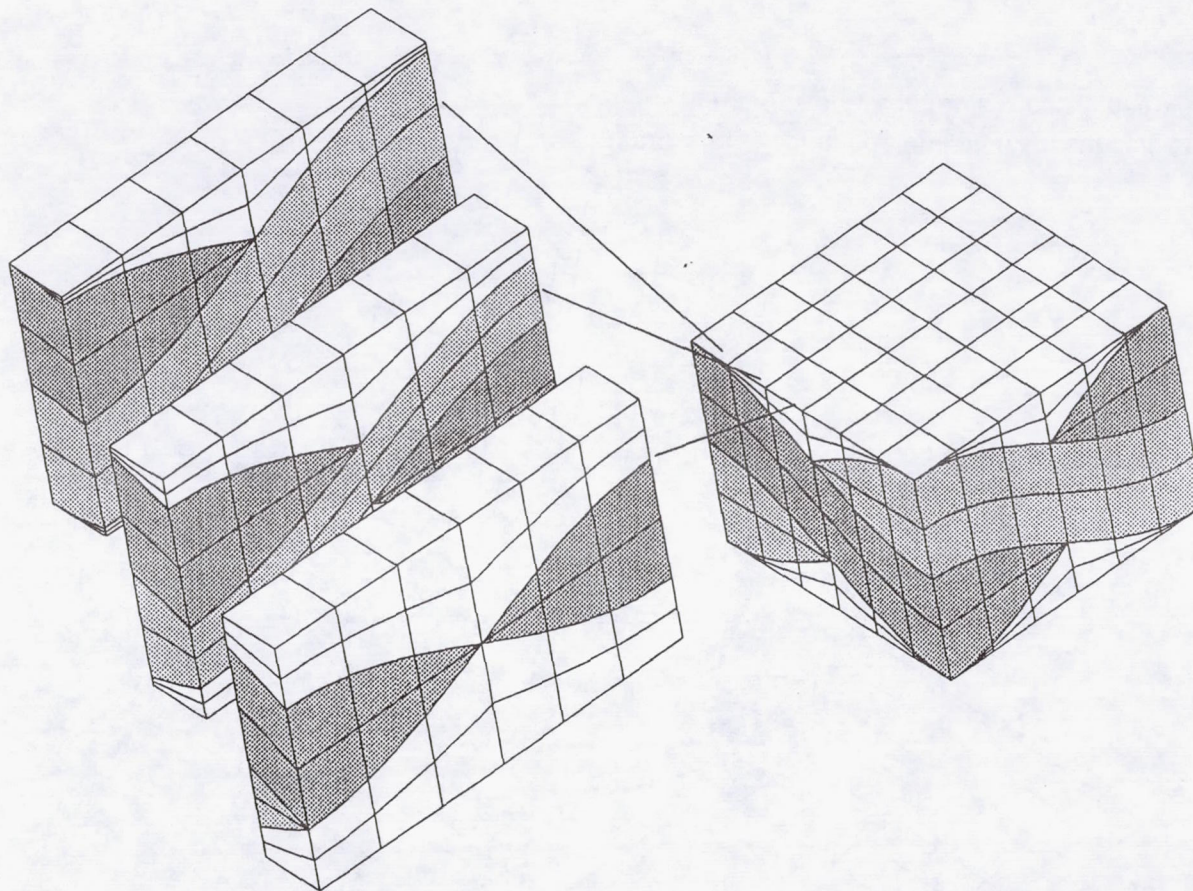


Figure 3.10: Sectioned view of 1/8th subcell translated mesh showing how matrix is added to tows.



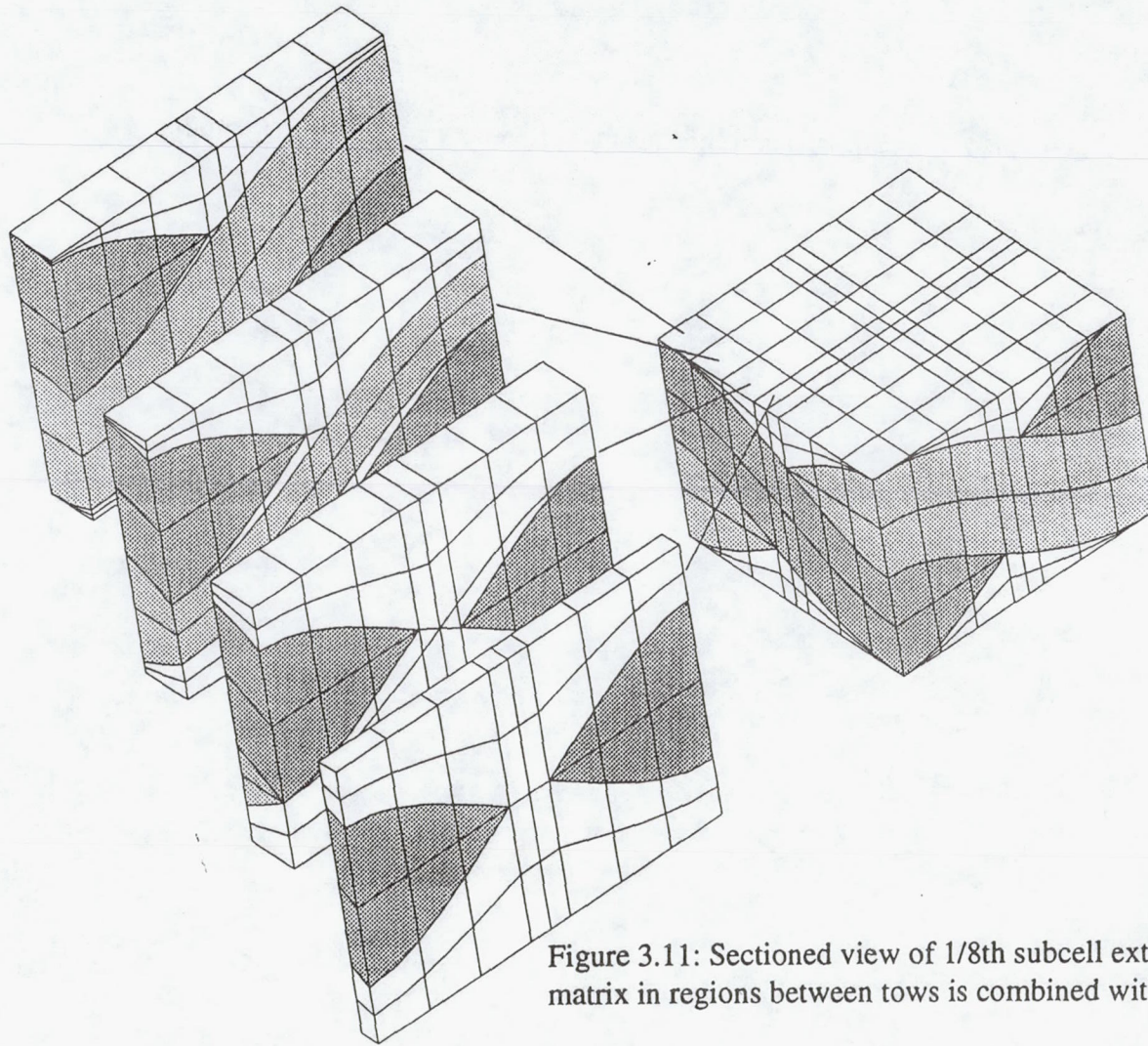


Figure 3.11: Sectioned view of 1/8th subcell extruded mesh showing how matrix in regions between tows is combined with rest of matrix.



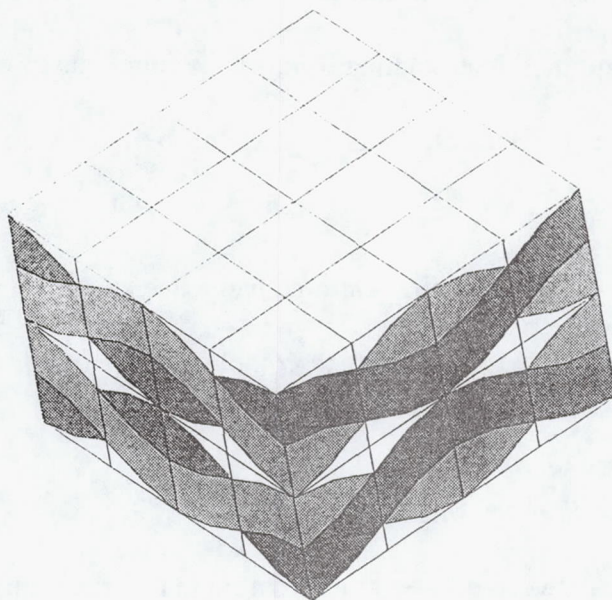
a variation of material properties at each integration point by specifying the angles at the nodes of the element and then interpolating using shape functions to obtain the values at integration points inside the element. This method will be referred to the *multiple angle* method.

These methods will be examined in a convergence study later in this chapter to determine which method is better and if such complication is truly necessary.

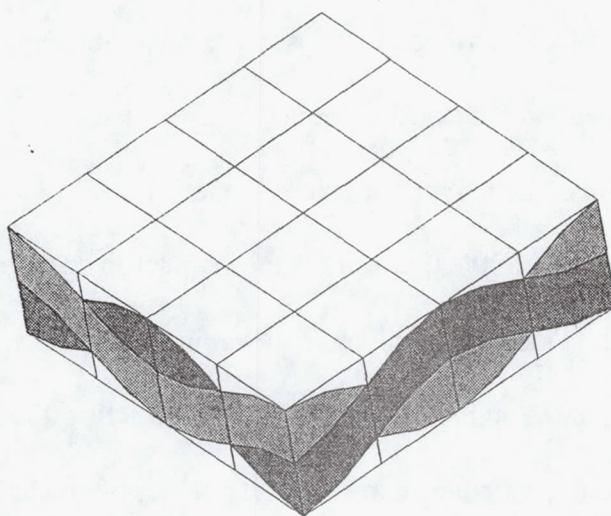
### 3.2.9 *Parameters describing meshes*

To differentiate between different meshes used in this research, a brief description will be presented for several different meshes and parameters used in their generation.

Two full unit cells of a woven composite are shown in Figure 3.12. The size of the unit cell is dependent on the stacking sequence of the mats. For symmetric stacking, the unit cell is larger than the unit cell for simply stacked mats. The basic building block of both unit cells is 1/32nd of the unit cell for the symmetric stacking and 1/16th the size of the simply stacked. This smaller block is shown in Figure 3.13. To generate a mesh for this smaller cell, three numbers will be used to describe the division of elements inside the mesh. The first number represents the number of elements through each fiber tow in the z direction. The second number represents the number of elements through each fiber tow in the y direction for the 0° tow and x direction for the 90° tow. The third number is the number of elements above the tows and below the tows. For



(a) Unit cell for symmetrically stacked mats



(b) Unit cell for simply stacked mats

Figure 3.12: Unit cells.



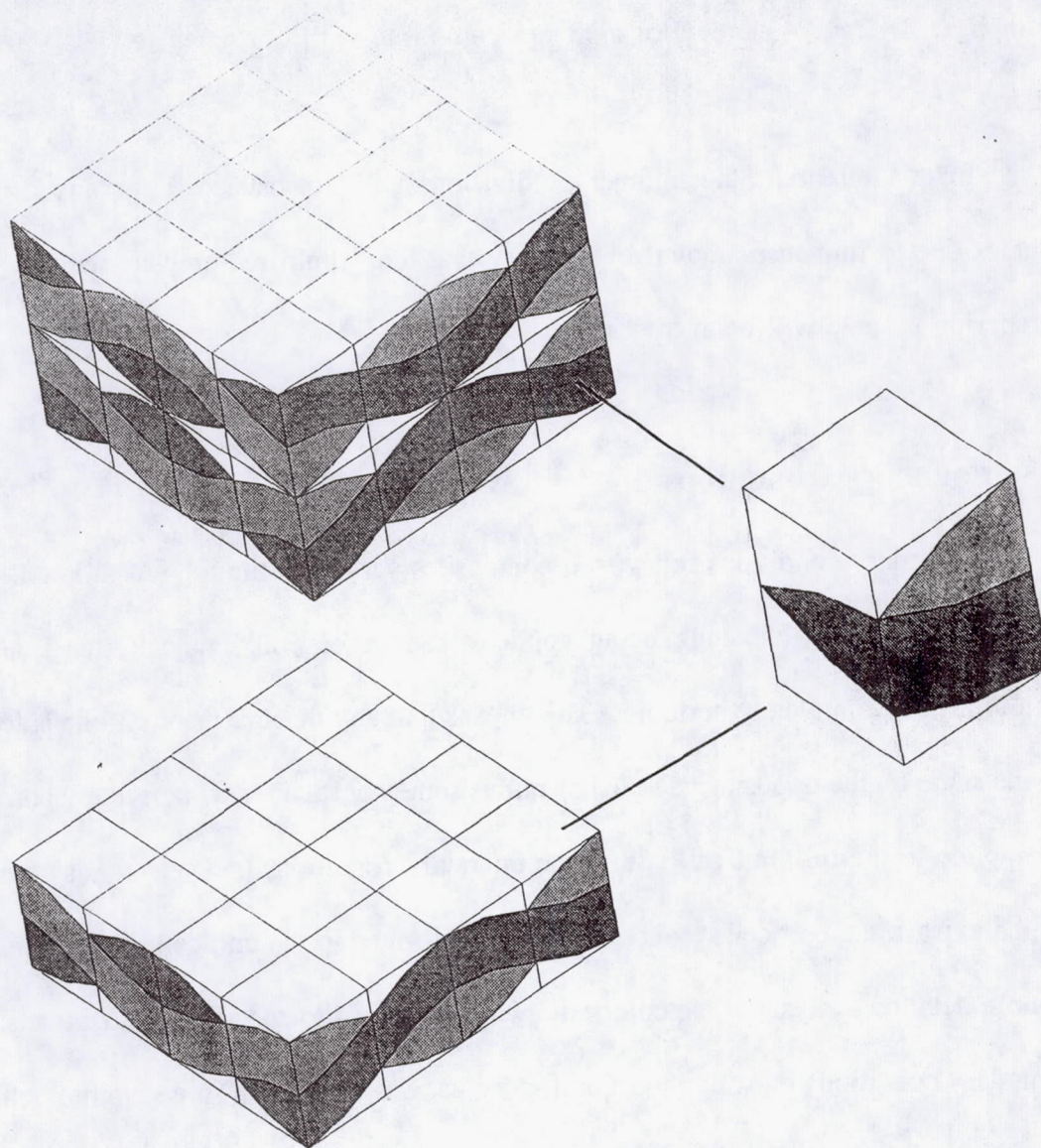


Figure 3.13: Basic building block of unit cells in Figure 3.12.



example, a 1/32nd 243 model of a woven composite with translated tows is shown in Figure 3.14.

In this research, the number of divisions will not exceed 9 for any of these indices due to immense amount of memory that this would require, consequently this numbering scheme will be adequate.

### 3.3 Boundary Conditions

Boundary conditions for woven composites vary with the type of unit cell being used and the type of loading being applied. For a general unit cell, the boundary conditions are completely periodic. This means that any displacement on one side must be the same on the opposite side plus or minus some constant. Any periodic loading can be applied to the full unit cell with these boundary conditions. Due to symmetries which exist in the unit cell, reduction can be performed to the unit cell in order to allow a more detailed analysis of the composite when subjected to specific types of loads. The boundary conditions must be modified for the various subcells. To derive the boundary conditions for the various RVE's used in this analysis, a general approach will be used. The following will apply to the symmetrically stacked mats as shown in Figure 3.12. The derivation for simply stacked mats is very similar and will not be covered in this research. The periodic boundary conditions will be given for a general full unit cell, and these will then be modified for different types of loading.



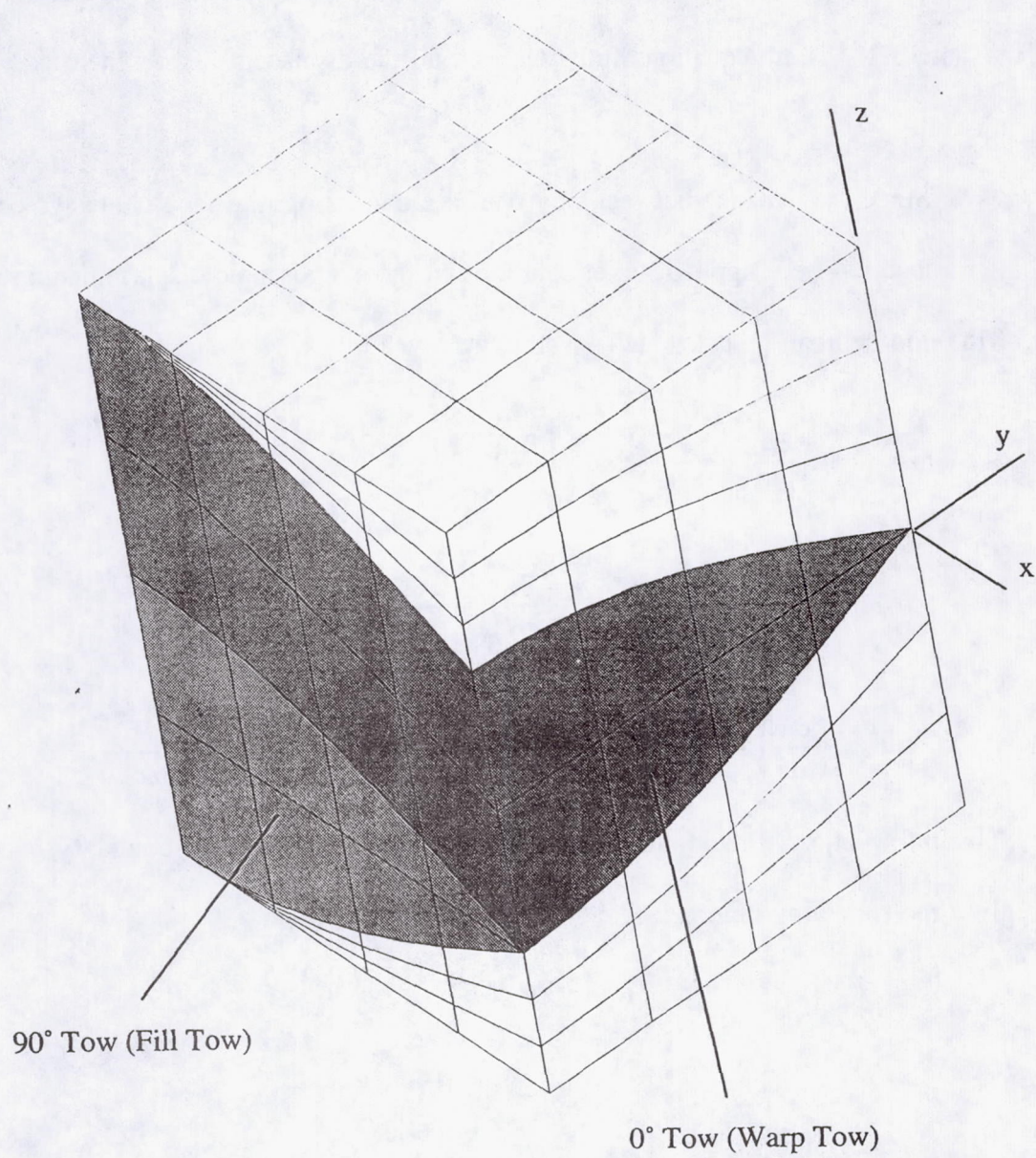


Figure 3.14: 1/32nd 243 translated model.



### 3.3.1 Periodic boundary conditions of general unit cell

For the unit cell in Figure 3.15, the periodic boundary conditions are summarized in Table 3.1. These equations fully describe all the displacements on each face of the unit cell.

Since the distance between any one face and its oppsite face is always constant after a load has been applied, ie. at equilibrium, the macroscopic displacement gradients of the unit cell can be calculated. These are given by

$$\left(\frac{\partial u}{\partial x}\right)_0 = \frac{u_A - u_B}{a}; \quad \left(\frac{\partial u}{\partial y}\right)_0 = \frac{u_A - u_C}{a}; \quad \left(\frac{\partial u}{\partial z}\right)_0 = \frac{u_A - u_D}{2c} \quad 3.3.1$$

$$\left(\frac{\partial v}{\partial x}\right)_0 = \frac{v_A - v_B}{a}; \quad \left(\frac{\partial v}{\partial y}\right)_0 = \frac{v_A - v_C}{a}; \quad \left(\frac{\partial v}{\partial z}\right)_0 = \frac{v_A - v_D}{2c} \quad 3.3.2$$

$$\left(\frac{\partial w}{\partial x}\right)_0 = \frac{w_A - w_B}{a}; \quad \left(\frac{\partial w}{\partial y}\right)_0 = \frac{w_A - w_C}{a}; \quad \left(\frac{\partial w}{\partial z}\right)_0 = \frac{w_A - w_D}{2c} \quad 3.3.3$$

Substituting eqns. (3.3.1), (3.3.2), and (3.3.3) into the periodic boundary conditions gives the following nine periodic boundary conditions

$$u\left(\frac{a}{2}, y, z\right) = u\left(-\frac{a}{2}, y, z\right) + a\left(\frac{\partial u}{\partial x}\right)_0 \quad 3.3.4$$

$$v\left(\frac{a}{2}, y, z\right) = v\left(-\frac{a}{2}, y, z\right) + a\left(\frac{\partial v}{\partial x}\right)_0 \quad 3.3.5$$

$$w\left(\frac{a}{2}, y, z\right) = w\left(-\frac{a}{2}, y, z\right) + a\left(\frac{\partial w}{\partial x}\right)_0 \quad 3.3.6$$



Table 3.1: Summary of periodic boundary conditions for the unit cell in Figure 3.15.

$x = \pm \frac{a}{2}$	$y = \pm \frac{a}{2}$	$z = \pm c$
$u(\frac{a}{2}, y, z) = u(-\frac{a}{2}, y, z) + u_A - u_B$	$u(x, \frac{a}{2}, z) = u(x, -\frac{a}{2}, z) + u_A - u_C$	$u(x, y, c) = u(x, y, -c) + u_A - u_D$
$v(\frac{a}{2}, y, z) = v(-\frac{a}{2}, y, z) + v_A - v_B$	$v(x, \frac{a}{2}, z) = v(x, -\frac{a}{2}, z) + v_A - v_C$	$v(x, y, c) = v(x, y, -c) + v_A - v_D$
$w(\frac{a}{2}, y, z) = w(-\frac{a}{2}, y, z) + w_A - w_B$	$w(x, \frac{a}{2}, z) = w(x, -\frac{a}{2}, z) + w_A - w_C$	$w(x, y, c) = w(x, y, -c) + w_A - w_D$



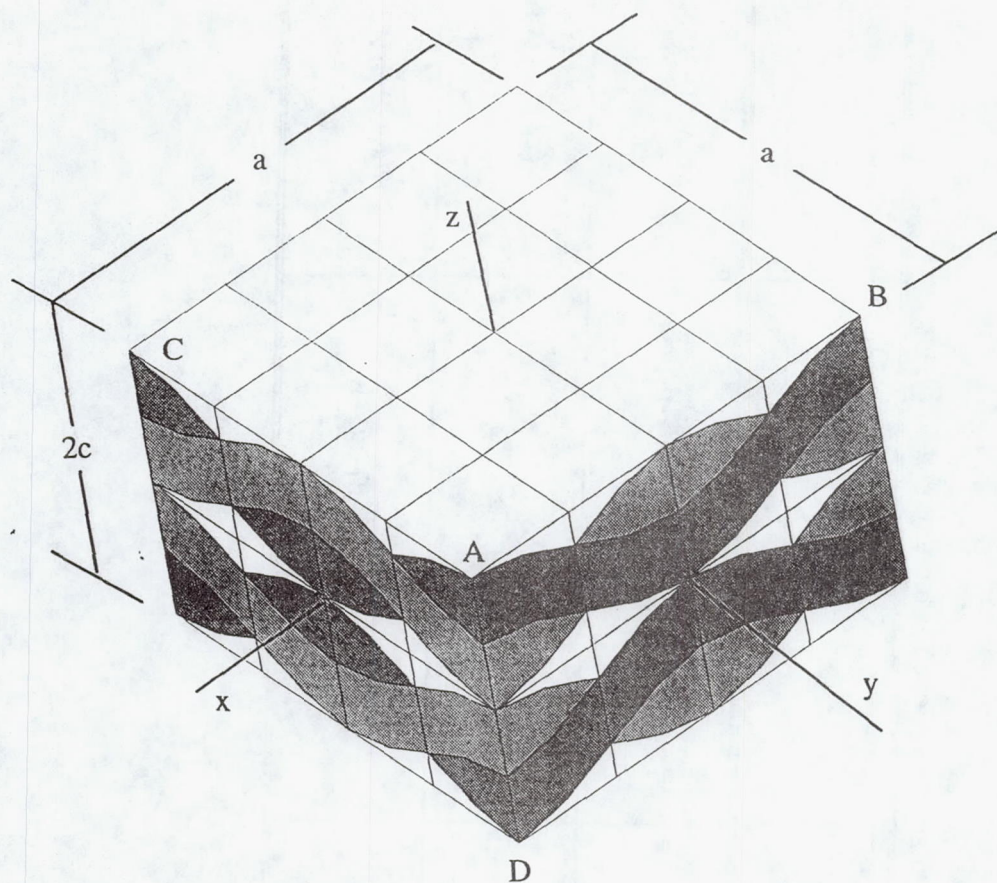


Figure 3.15: Unit cell used for derivation of boundary conditions.



$$u(x, \frac{a}{2}, z) = u(x, -\frac{a}{2}, z) + a \left( \frac{\partial u}{\partial y} \right)_0 \quad 3.3.7$$

$$v(x, \frac{a}{2}, z) = v(x, -\frac{a}{2}, z) + a \left( \frac{\partial v}{\partial y} \right)_0 \quad 3.3.8$$

$$w(x, \frac{a}{2}, z) = w(x, -\frac{a}{2}, z) + a \left( \frac{\partial w}{\partial y} \right)_0 \quad 3.3.9$$

$$u(x, y, c) = u(x, y, -c) + 2c \left( \frac{\partial u}{\partial z} \right)_0 \quad 3.3.10$$

$$v(x, y, c) = v(x, y, -c) + 2c \left( \frac{\partial v}{\partial z} \right)_0 \quad 3.3.11$$

$$w(x, y, c) = w(x, y, -c) + 2c \left( \frac{\partial w}{\partial z} \right)_0 \quad 3.3.12$$

These boundary conditions are the basis for any reduction which is to be made to the unit cell.

Macroscopic engineering strains can also be calculated using the following equations

$$\bar{\epsilon}_x = \left( \frac{\partial u}{\partial x} \right)_0 \quad 3.3.13$$

$$\bar{\epsilon}_y = \left( \frac{\partial v}{\partial y} \right)_0 \quad 3.3.14$$

$$\bar{\epsilon}_z = \left( \frac{\partial w}{\partial z} \right)_0 \quad 3.3.15$$

$$\bar{\epsilon}_{xy} = \left( \frac{\partial u}{\partial y} \right)_0 + \left( \frac{\partial v}{\partial x} \right)_0 \quad 3.3.16$$

$$\bar{\epsilon}_{yz} = \left( \frac{\partial v}{\partial z} \right)_0 + \left( \frac{\partial w}{\partial y} \right)_0 \quad 3.3.17$$

$$\bar{\epsilon}_{xz} = \left( \frac{\partial u}{\partial z} \right)_0 + \left( \frac{\partial w}{\partial x} \right)_0 \quad 3.3.18$$

### 3.3.2 Extension

Starting with the full unit cell as shown in Figure 3.15, boundary conditions for the 1/8th and 1/32nd subcells can be derived for extension. If an extension is applied along the x-axis, the only non-zero macroscopic strains are  $\bar{\epsilon}_x$ ,  $\bar{\epsilon}_y$  and  $\bar{\epsilon}_z$ . If we define

$$u_o = \frac{a}{2} \left( \frac{\partial u}{\partial x} \right)_0, \quad v_o = \frac{a}{2} \left( \frac{\partial v}{\partial y} \right)_0, \quad w_o = c \left( \frac{\partial w}{\partial z} \right)_0 \quad 3.3.19$$

and impose that

$$u_A = -u_B = u_o, \quad v_A = -v_C = v_o, \quad w_A = -w_D = w_o \quad 3.3.20$$

then by inserting these into the periodic boundary conditions given in Table 3.1 gives the nine following periodic boundary conditions for extension.



At  $x = \pm \frac{a}{2}$

$$u\left(\frac{a}{2}, y, z\right) = u\left(-\frac{a}{2}, y, z\right) + 2u_o \quad 3.3.21$$

$$v\left(\frac{a}{2}, y, z\right) = v\left(-\frac{a}{2}, y, z\right) \quad 3.3.22$$

$$w\left(\frac{a}{2}, y, z\right) = w\left(-\frac{a}{2}, y, z\right) \quad 3.3.23$$

At  $y = \pm \frac{a}{2}$

$$u\left(x, \frac{a}{2}, z\right) = u\left(x, -\frac{a}{2}, z\right) \quad 3.3.24$$

$$v\left(x, \frac{a}{2}, z\right) = v\left(x, -\frac{a}{2}, z\right) + 2v_o \quad 3.3.25$$

$$w\left(x, \frac{a}{2}, z\right) = w\left(x, -\frac{a}{2}, z\right) \quad 3.3.26$$

and at  $z = \pm c$



$$u(x,y,c)=u(x,y,-c) \quad 3.3.27$$

$$v(x,y,c)=v(x,y,-c) \quad 3.3.28$$

$$w(x,y,c)=w(x,y,-c)+2w_o \quad 3.3.29$$

Symmetry about the  $xy$ ,  $xz$ , and  $yz$  planes produce the following useful relations.

$$xy: \quad \begin{cases} u(x,y,z) = u(x,y,-z) \\ v(x,y,z) = v(x,y,-z) \\ w(x,y,z) = -w(x,y,-z) \end{cases} \quad 3.3.30$$

$$xz: \quad \begin{cases} u(x,y,z) = u(x,-y,z) \\ v(x,y,z) = -v(x,-y,z) \\ w(x,y,z) = w(x,-y,z) \end{cases} \quad 3.3.31$$

$$yz: \quad \begin{cases} u(x,y,z) = -u(-x,y,z) \\ v(x,y,z) = v(-x,y,z) \\ w(x,y,z) = w(-x,y,z) \end{cases} \quad 3.3.32$$

If these symmetries are applied to eqns. (3.3.21)-(3.3.29), the following non-trivial equations are produced.

$$u\left(\frac{a}{2}, y, z\right) = -u\left(-\frac{a}{2}, y, z\right) = u_o \quad 3.3.33$$

$$v\left(x, \frac{a}{2}, z\right) = -v\left(x, -\frac{a}{2}, z\right) = v_o \quad 3.3.34$$

$$w(x, y, c) = -w(x, y, -c) = w_o \quad 3.3.35$$

Eqns. (3.3.33)-(3.3.35) are the non-trivial periodic boundary conditions for extension of



the woven composite unit cell in Figure 3.15. Eqns. (3.3.30)-(3.3.32) also imply that at  $x, y, z = 0$

$$u(0, y, z) = v(x, 0, z) = w(x, y, 0) = 0 \quad 3.3.36$$

This equation along with eqns. (3.3.33)-(3.3.35) fully describe the boundary conditions for the each 1/8th subcell in the unit cell. If the origin is now translated to center of the 1/8th unit cell in the region  $x, y, z > 0$  as shown in Figure 3.16, the boundary conditions on the 1/8th unit cell become

$$\begin{aligned} u\left(\frac{a}{4}, y, z\right) &= -u\left(-\frac{a}{4}, y, z\right) = \frac{u_o}{2}; \\ v\left(x, \frac{a}{4}, z\right) &= -v\left(x, -\frac{a}{4}, z\right) = \frac{v_o}{2}; \\ w\left(x, y, \frac{c}{2}\right) &= -w\left(x, y, -\frac{c}{2}\right) = \frac{w_o}{2}. \end{aligned} \quad 3.3.37$$

To get boundary conditions for the 1/32nd subcell, symmetries in the 1/8th subcell must be exploited. Anti-symmetry about the  $x$ ,  $y$ , and  $z$  axes in the 1/8th subcell shown in Figure 3.16, gives the following relations.

$$x\text{-axis:} \quad \begin{cases} u(x, y, z) = u(x, -y, -z) \\ v(x, y, z) = -v(x, -y, -z) \\ w(x, y, z) = -w(x, -y, -z) \end{cases} \quad 3.3.38$$

$$y\text{-axis:} \quad \begin{cases} u(x, y, z) = -u(-x, y, -z) \\ v(x, y, z) = v(-x, y, -z) \\ w(x, y, z) = -w(-x, y, -z) \end{cases} \quad 3.3.39$$

$$z\text{-axis:} \quad \begin{cases} u(x, y, z) = -u(-x, -y, z) \\ v(x, y, z) = -v(-x, -y, z) \\ w(x, y, z) = w(-x, -y, z) \end{cases} \quad 3.3.40$$



These equations imply that on the  $yz$ ,  $xz$ , and  $xy$  planes in Figure 3.16, the boundary conditions become

$$yz: \begin{cases} u(0,y,z) = -u(0,y,-z) = -u(0,-y,z) \\ v(0,y,z) = v(0,y,-z) = -v(0,-y,z) \\ w(0,y,z) = -w(0,y,-z) = w(0,-y,z) \end{cases} \quad 3.3.41$$

$$xz: \begin{cases} u(x,0,z) = -u(-x,0,z) = u(x,0,-z) \\ v(x,0,z) = -v(-x,0,z) = -v(x,0,-z) \\ w(x,0,z) = w(-x,0,z) = -w(x,0,-z) \end{cases} \quad 3.3.42$$

$$xy: \begin{cases} u(x,y,0) = -u(-x,y,0) = u(x,-y,0) \\ v(x,y,0) = v(-x,y,0) = -v(x,-y,0) \\ w(x,y,0) = -w(-x,y,0) = -w(x,-y,0) \end{cases} \quad 3.3.43$$

These boundary conditions are valid for two different 1/32nd subcells. However, only the one shown in Figure 3.17 will be used for this study due to the mesh generation strategy used. The boundary conditions used for extension are

$$u\left(\frac{a}{4}, x, y\right) = \frac{u_o}{2} \quad 3.3.44$$

$$w(x, y, c) = w(x, y, -c) = \frac{w_o}{2} \quad 3.3.45$$

$$v\left(x, \frac{a}{4}, z\right) = \frac{v_o}{2} \quad 3.3.46$$

$$yz: \begin{cases} u(0,y,z) = -u(0,y,-z) \\ v(0,y,z) = v(0,y,-z) \\ w(0,y,z) = -w(0,y,-z) \end{cases} \quad 3.3.47$$



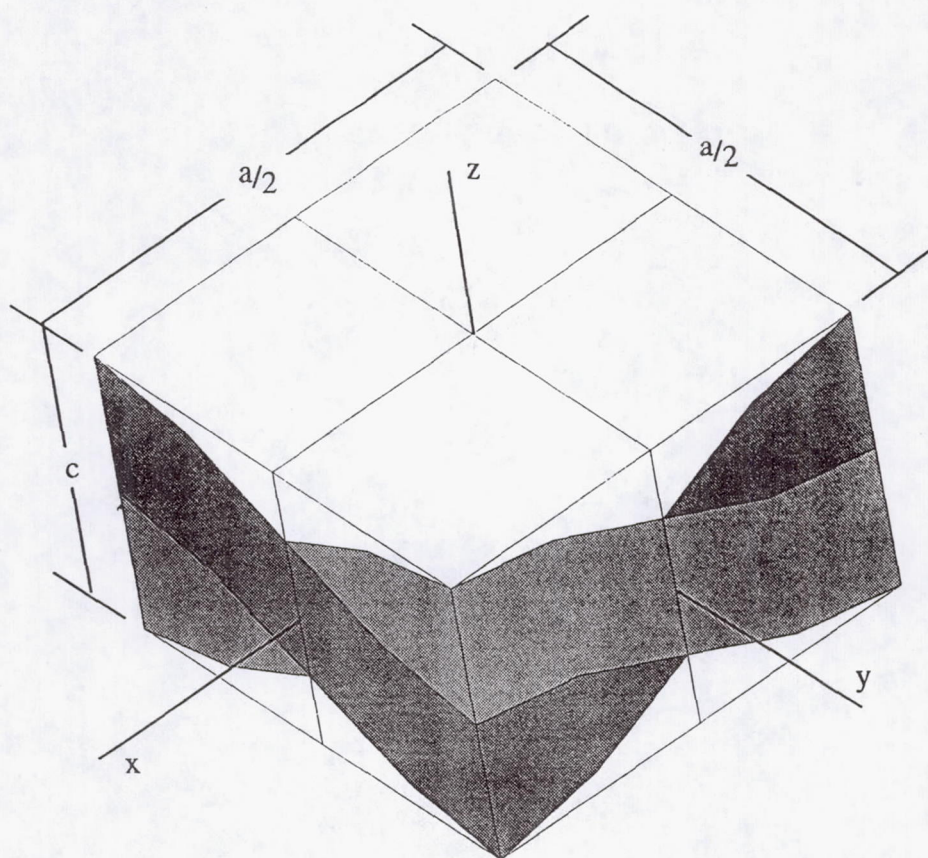


Figure 3.16: 1/8th subcell used in derivation of boundary conditions.

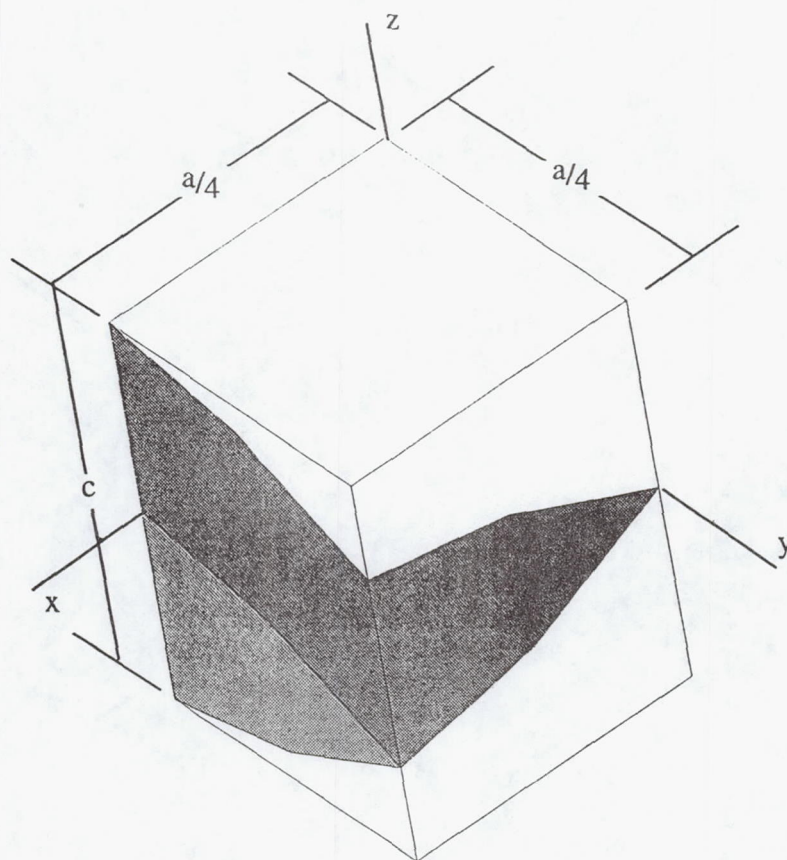


Figure 3.17: 1/32nd subcell used in derivation of boundary conditions.



$$xz: \quad \begin{cases} u(x,0,z) = u(x,0,-z) \\ v(x,0,z) = -v(x,0,-z) \\ w(x,0,z) = -w(x,0,-z) \end{cases} \quad 3.3.48$$

With the boundary conditions fully described for the full, 1/8th and 1/32nd subcells for extension, we will proceed to the boundary conditions for an applied  $\epsilon_{xz}$  shear strain.

### 3.3.3 $\epsilon_{xz}$ shear

Starting again with the full unit cell in Figure 3.15 and applying a shear strain, boundary conditions will be derived for the 1/8th and 1/32nd subcells. If a shear strain is applied such that

$$w_A = -w_B = w_o; \quad u_A = -u_D = u_o \quad 3.3.49$$

the non-zero macroscopic displacement gradients are given by

$$\left( \frac{\partial u}{\partial z} \right)_0 = \frac{u_o}{c}; \quad \left( \frac{\partial w}{\partial x} \right)_0 = \frac{2w_o}{a} \quad 3.3.50$$

Applying these to the periodic boundary conditions given in Table 3.1 gives the nine following periodic boundary conditions for shear.

At  $x = \pm \frac{a}{2}$

$$u\left(\frac{a}{2}, y, z\right) = u\left(-\frac{a}{2}, y, z\right) \quad 3.3.51$$

$$v\left(\frac{a}{2}, y, z\right) = -v\left(-\frac{a}{2}, y, z\right) \quad 3.3.52$$

$$w\left(\frac{a}{2}, y, z\right) = w\left(-\frac{a}{2}, y, z\right) + 2w_o \quad 3.3.53$$

At  $y = \pm \frac{a}{2}$

$$u\left(x, \frac{a}{2}, z\right) = u\left(x, -\frac{a}{2}, z\right) \quad 3.3.54$$

$$v\left(x, \frac{a}{2}, z\right) = v\left(x, -\frac{a}{2}, z\right) = 0 \quad 3.3.55$$

$$w\left(x, \frac{a}{2}, z\right) = w\left(x, -\frac{a}{2}, z\right) \quad 3.3.56$$

and at  $z = \pm c$

$$u(x, y, c) = u(x, y, -c) + 2u_o \quad 3.3.57$$

$$v(x, y, c) = v(x, y, -c) \quad 3.3.58$$

$$w(x, y, c) = w(x, y, -c) \quad 3.3.59$$



Symmetry about the  $yz$ ,  $xy$ , and  $xz$  planes gives

$$yz: \begin{cases} u(x,y,z) = u(-x,y,z) \\ v(x,y,z) = -v(-x,y,z) \\ w(x,y,z) = -w(-x,y,z) \end{cases} \quad 3.3.60$$

$$xy: \begin{cases} u(x,y,z) = -u(x,y,-z) \\ v(x,y,z) = -v(x,y,-z) \\ w(x,y,z) = w(x,y,-z) \end{cases} \quad 3.3.61$$

$$xz: \begin{cases} u(x,y,z) = u(x,-y,z) \\ v(x,y,z) = -v(x,-y,z) \\ w(x,y,z) = w(x,-y,z) \end{cases} \quad 3.3.62$$

If these symmetries are applied to the above periodic boundary conditions, the non-trivial boundary conditions become

$$v\left(\frac{a}{2}, y, z\right) = v\left(-\frac{a}{2}, y, z\right) = 0 \quad 3.3.63$$

$$w\left(\frac{a}{2}, y, z\right) = -w\left(-\frac{a}{2}, y, z\right) = w_o \quad 3.3.64$$

$$v\left(x, \frac{a}{2}, z\right) = v\left(x, -\frac{a}{2}, z\right) = 0 \quad 3.3.65$$

$$u(x, y, c) = -u(x, y, -c) = u_o \quad 3.3.66$$

$$v(x, y, c) = v(x, y, -c) = 0 \quad 3.3.67$$

Using eqns. (3.3.60)-(3.3.62) at  $x, y, z = 0$ , the following boundary conditions are also established for each 1/8th subcell.

$$yz: \quad \begin{cases} v(0,y,z) = -v(0,y,z) = 0 \\ w(0,y,z) = -w(0,y,z) = 0 \end{cases} \quad 3.3.68$$

$$xy: \quad \begin{cases} u(x,y,0) = -u(x,y,0) = 0 \\ v(x,y,0) = -v(x,y,0) = 0 \end{cases} \quad 3.3.69$$

$$xz: \quad \{ \quad v(x,0,z) = -v(x,0,z) = 0 \quad 3.3.70$$

Shifting the origin to the center of the 1/8th unit cell in the region  $x,y,z > 0$ , the boundary conditions for this region become

$$\begin{aligned} v\left(\frac{a}{4}, y, z\right) &= v\left(-\frac{a}{4}, y, z\right) = v\left(x, y, \frac{c}{2}\right) = \\ v\left(x, y, -\frac{c}{2}\right) &= v\left(x, \frac{a}{4}, z\right) = v\left(x, -\frac{a}{4}, z\right) = 0 \end{aligned} \quad 3.3.71$$

$$w\left(\frac{a}{4}, y, z\right) = -w\left(-\frac{a}{4}, y, z\right) = \frac{w_o}{2} \quad 3.3.72$$

$$u(x, y, c) = -u(x, y, -c) = \frac{u_o}{2} \quad 3.3.73$$

To get boundary conditions for the 1/32nd subcell, symmetries in the 1/8th subcell must be exploited. Anti-symmetry about the y axis produces

$$\begin{aligned} u(x, y, z) &= -u(-x, y, -z) \\ v(x, y, z) &= v(-x, y, -z) \\ w(x, y, z) &= -w(-x, y, -z) \end{aligned} \quad 3.3.74$$

which gives at  $x=0$



$$\begin{aligned}
 u(0,y,z) &= -u(0,y,-z) \\
 v(0,y,z) &= v(0,y,-z) \\
 w(0,y,z) &= -w(0,y,-z)
 \end{aligned}
 \tag{3.3.75}$$

Noting that a negative load gives the opposite displacement than that of the same but positive load, the  $v$  displacement gives

$$v(x,y,z)|_{+\bar{\epsilon}_x} = -v(x,y,z)|_{-\bar{\epsilon}_x} \tag{3.3.76}$$

Since the  $-y$  region of the 1/8th subcell is anti-symmetric to the  $+y$  region, the shear being experienced by the  $-y$  region is opposite that being experienced by the  $+y$  region.

This gives

$$v(x,y,z)|_{+\bar{\epsilon}_x} = -v(x,-y,-z)|_{-\bar{\epsilon}_x} \tag{3.3.77}$$

(3.3.76) into (3.3.77) gives

$$v(x,y,z)|_{\bar{\epsilon}_x} = v(x,-y,-z)|_{\bar{\epsilon}_x} \tag{3.3.78}$$

So, along  $y = 0$ ,

$$v(x,0,z) = v(x,0,-z) \tag{3.3.79}$$

Similarly,

$$w(x,0,z) = w(x,0,-z) \tag{3.3.80}$$

The above fully specifies the boundary conditions for each 1/32nd subcell in the 1/8th subcell. The following is a summary of the non-trivial boundary conditions for the 1/32nd subcell shown in Figure 3.17 subjected to  $\epsilon_x$  shear.

$$v\left(\frac{a}{4}, y, z\right) = v\left(x, y, \frac{c}{2}\right) = v\left(x, y, -\frac{c}{2}\right) = v\left(x, \frac{a}{4}, z\right) = 0 \quad 3.3.81$$

$$w\left(\frac{a}{4}, y, z\right) = \frac{w_o}{2} \quad 3.3.82$$

$$u\left(x, y, \frac{c}{2}\right) = -u\left(x, y, -\frac{c}{2}\right) = \frac{u_o}{2} \quad 3.3.83$$

$$\begin{aligned} u(0, y, z) &= -u(0, y, -z) \\ v(0, y, z) &= v(0, y, -z) \\ w(0, y, z) &= -w(0, y, -z) \end{aligned} \quad 3.3.84$$

$$\begin{aligned} u(x, 0, z) &= -u(x, 0, -z) \\ v(x, 0, z) &= v(x, 0, -z) \\ w(x, 0, z) &= w(x, 0, -z) \end{aligned} \quad 3.3.85$$

Boundary conditions have been specified for the full, 1/8th and 1/32nd subcell for  $\epsilon_{xz}$  shear. Next  $\epsilon_{xy}$  shear will be covered.

### 3.3.4 $\epsilon_{xy}$ shear

Again, starting with the periodic boundary conditions for the full unit cell, boundary conditions will be derived for 1/8th and 1/32nd subcells. If a special case of macroscopic  $\epsilon_{xy}$  shear strain is applied such that

$$u_A = -u_C = v_A = -v_B = d \quad 3.3.86$$

the non-zero macroscopic displacement gradients are given by

$$\left(\frac{\partial u}{\partial y}\right)_0 = \left(\frac{\partial v}{\partial x}\right)_0 = \frac{2d}{a} \quad 3.3.87$$



Applying these to the periodic boundary conditions given in Table 3.1 gives the nine following periodic conditions for shear.

At  $x = \pm \frac{a}{2}$

$$u\left(\frac{a}{2}, y, z\right) = u\left(-\frac{a}{2}, y, z\right) \quad 3.3.88$$

$$v\left(\frac{a}{2}, y, z\right) = -v\left(-\frac{a}{2}, y, z\right) + 2d \quad 3.3.89$$

$$w\left(\frac{a}{2}, y, z\right) = w\left(-\frac{a}{2}, y, z\right) \quad 3.3.90$$

At  $y = \pm \frac{a}{2}$

$$u\left(x, \frac{a}{2}, z\right) = u\left(x, -\frac{a}{2}, z\right) + 2d \quad 3.3.91$$

$$v\left(x, \frac{a}{2}, z\right) = v\left(x, -\frac{a}{2}, z\right) \quad 3.3.92$$

$$w\left(x, \frac{a}{2}, z\right) = w\left(x, -\frac{a}{2}, z\right) \quad 3.3.93$$

and at  $z = \pm c$

$$u(x, y, c) = u(x, y, -c) \quad 3.3.94$$

$$v(x,y,c)=v(x,y,-c) \quad 3.3.95$$

$$w(x,y,c)=w(x,y,-c) \quad 3.3.96$$

Anti-symmetry about the  $z$  axis gives

$$\begin{aligned} u(x,y,z) &= -u(-x,-y,z) \\ v(x,y,z) &= -v(-x,-y,z) \\ w(x,y,z) &= w(-x,-y,z) \end{aligned} \quad 3.3.97$$

Symmetry about the  $xy$ ,  $xz$ , and  $yz$  planes gives

$$xy: \quad \begin{cases} u(x,y,z) = u(x,y,-z) \\ v(x,y,z) = v(x,y,-z) \\ w(x,y,z) = -w(x,y,-z) \end{cases} \quad 3.3.98$$

$$yz: \quad \begin{cases} u(x,y,z) = u(-x,y,z) \\ v(x,y,z) = -v(-x,y,z) \\ w(x,y,z) = -w(-x,y,z) \end{cases} \quad 3.3.99$$

$$xz: \quad \begin{cases} u(x,y,z) = -u(x,-y,z) \\ v(x,y,z) = v(x,-y,z) \\ w(x,y,z) = -w(x,-y,z) \end{cases} \quad 3.3.100$$

Eqn. (3.3.98) implies that

$$w(x,y,0) = -w(x,y,0) = 0 \quad 3.3.101$$

Further, periodic boundary conditions for  $w$  at  $z=\pm c$  imply

$$w(x,y,c) = w(x,y,-c) \quad 3.3.102$$

but



$$w(x,y,c) = -w(x,y,-c) \quad 3.3.103$$

which gives

$$w(x,y,c) = w(x,y,-c) = 0 \quad 3.3.104$$

Similarly, at  $y = 0$ , eqn. (3.3.100) implies

$$u(x,0,z) = w(x,0,z) = 0 \quad 3.3.105$$

and at  $x = 0$ , eqn. (3.3.99) implies

$$v(0,y,z) = w(0,y,z) = 0 \quad 3.3.106$$

Also, using eqns. (3.3.98)-(3.3.100) to trivialize the periodic boundary conditions in eqns. (3.3.88)-(3.3.96) gives the following non-trivial conditions

$$v\left(\frac{a}{2}, y, z\right) = -v\left(-\frac{a}{2}, y, z\right) = v_o \quad 3.3.107$$

$$u\left(x, \frac{a}{2}, z\right) = -u\left(x, -\frac{a}{2}, z\right) = u_o \quad 3.3.108$$

$$w\left(\pm \frac{a}{2}, y, z\right) = w\left(x, \pm \frac{a}{2}, z\right) = w(x, y, \pm c) = 0 \quad 3.3.109$$

If the 1/8th unit cell in the region  $x, y, z > 0$  is again considered and the origin is translated to its center as shown in Figure 3.16, the non-trivial boundary conditions become

$$v\left(\frac{a}{4}, y, z\right) = -v\left(-\frac{a}{4}, y, z\right) = \frac{v_o}{2} \quad 3.3.110$$

$$u(x, \frac{a}{4}, z) = -u(x, -\frac{a}{4}, z) = \frac{u_o}{2} \quad 3.3.111$$

$$w(\pm \frac{a}{4}, y, z) = w(x, \pm \frac{a}{4}, z) = w(x, y, \pm \frac{c}{2}) = 0 \quad 3.3.112$$

In order to obtain boundary conditions for the 1/32nd subcell, symmetries inherent to the 1/8th subcell must be exploited. Anti-symmetries of geometry and loading similar to the anti-symmetries around the  $x$  axis for  $\epsilon_{xz}$  gives the following relations about the  $x$  and  $y$  axes in Figure 3.16 of the 1/8th subcell subjected to  $\epsilon_{xy}$ .

$$x: \begin{cases} u(x, y, z) = -u(x, -y, -z) \\ v(x, y, z) = v(x, -y, -z) \\ w(x, y, z) = w(x, -y, -z) \end{cases} \quad 3.3.113$$

$$y: \begin{cases} u(x, y, z) = u(-x, y, -z) \\ v(x, y, z) = -v(-x, y, -z) \\ w(x, y, z) = w(-x, y, -z) \end{cases} \quad 3.3.114$$

Anti-symmetry about the  $z$  axis gives

$$z: \begin{cases} u(x, y, z) = -u(-x, -y, z) \\ v(x, y, z) = -v(-x, -y, z) \\ w(x, y, z) = w(-x, -y, z) \end{cases} \quad 3.3.115$$

At  $x, y = 0$ , the following conditions develop.

$$\begin{aligned} u(0, y, z) &= u(0, y, -z) \\ v(0, y, z) &= -v(0, y, -z) \\ w(0, y, z) &= w(0, y, -z) \end{aligned} \quad 3.3.116$$

$$\begin{aligned} u(x, 0, z) &= -u(x, 0, -z) \\ v(x, 0, z) &= v(x, 0, -z) \\ w(x, 0, z) &= w(x, 0, -z) \end{aligned} \quad 3.3.117$$



Equations (3.3.116) and (3.3.117) along with the following four are the boundary conditions for the 1/32nd subcell.

$$v\left(\frac{a}{4}, y, z\right) = \frac{v_o}{2} \quad 3.3.118$$

$$u\left(x, \frac{a}{4}, z\right) = \frac{u_o}{2} \quad 3.3.119$$

$$w\left(\frac{a}{4}, y, x\right) = 0 \quad 3.3.120$$

$$w\left(x, \frac{a}{4}, z\right) = 0 \quad 3.3.121$$

Again, it must be emphasized that these are for the special case of  $\epsilon_{xy}$  where the displacements on the  $x$  and  $y$  faces of the full unit cell are the same. If different displacements are applied,  $u$  and  $v$  displacements on opposite faces on the 1/32nd subcell become dependent on one another and this is very difficult to enforce using finite elements.

### 3.3.5 Savings due to unit cell reduction

To illustrate the amount of savings which is produced by the various simplifications mentioned previously, the memory and CPU time required to analyze the model in extension are compared for the 1/32nd, 1/8th and full

Table 3.2: CPU times and memory requirement for 111 translated model.

Cell Type	CPU time (s)	Memory Requirement (Words)
1/32nd	2	3.4K
1/8th	7	25K
Full	90	0.625M

unit cell models of a woven composite. A summary of the results is presented in Table

3.2. The amount of memory required for the 1/32nd 111 translated subcell for extension is about 3.4K Words. A 1/8th 111 translated subcell requires almost eight times that at 25K Words, and the full unit cell requires 0.625M Words, about 180 times that of the 1/32nd subcell. CPU time is also cut severely by these simplifications. The 1/32nd subcell takes about 1/50th the amount of time required to analyze the complete unit cell.

### 3.4 Material Properties

The material properties used in this investigation were selected in order to allow direct comparison with some existing results [8]. This made it possible to detect errors which may have been made in the analysis. For the warp and fill tows, the elastic properties are the same and are given below with the resin properties.

Fiber Tow:

$$E_x = 206.9 \text{ GPa}, E_y = E_z = 5.171 \text{ GPa}$$

$$\nu_{xy} = \nu_{xz} = \nu_{yz} = 0.25$$

$$G_{xy} = G_{xz} = G_{yz} = 2.386 \text{ GPa}$$

$$X_t = 1034 \text{ MPa}, X_c = 689.5 \text{ MPa}$$

$$Y_t = Z_t = 41.37 \text{ MPa}, Y_c = Z_c = 117.2 \text{ MPa}$$

$$S_{xy} = S_{yz} = S_{xz} = 68.95 \text{ MPa}$$

Resin:

$$E = 3.45 \text{ GPa}, \nu = 0.35, G = 1.28 \text{ GPa}$$

$$X_t = 103.4 \text{ MPa}, X_c = 241.3 \text{ MPa}, S = 89.6 \text{ MPa}$$



### 3.5 Convergence Study

A convergence study was done in order to determine finite element models which could adequately predict moduli and stress distributions. The effective elastic properties of the composite will be presented first. A study of translated and extruded meshes is studied. The meshes used for the convergence study are shown in Figures 3.18 and 3.19.

#### 3.5.1 Elastic Properties

The convergence of elastic properties for the translated and extruded model with a waviness ratio of 1/3 is presented in Tables 3.3-3.6. There are only 6 independent elastic material parameters for a balanced plain weave composite. These are  $E_x$ ,  $\nu_{xy}$ ,  $\nu_{xz}$ ,  $E_z$ ,  $G_{xy}$  and  $G_{xz}$ .  $E_x$  and  $E_y$  are equivalent as well as  $\nu_{xz}$  and  $\nu_{yz}$ . Also,  $G_{yz}$  is the same as  $G_{xz}$ . Material properties of the woven composite are studied individually to determine the convergence of each with mesh refinement.

#### *Translated Model*

Tables 3.3 and 3.4 show the convergence of the elastic material properties for the translated model. For the 121 multiple angle model, the value of  $E_x$  is only 0.8% greater than that predicted by the nearly converged value of the translated 454 multiple angle model which contains 25 times the number of elements than the 121 model. The single angle 121 model predicts a value that is -6.6% less than that predicted by the multi-angle 454 model. It is interesting to note that convergence of the values is substantially



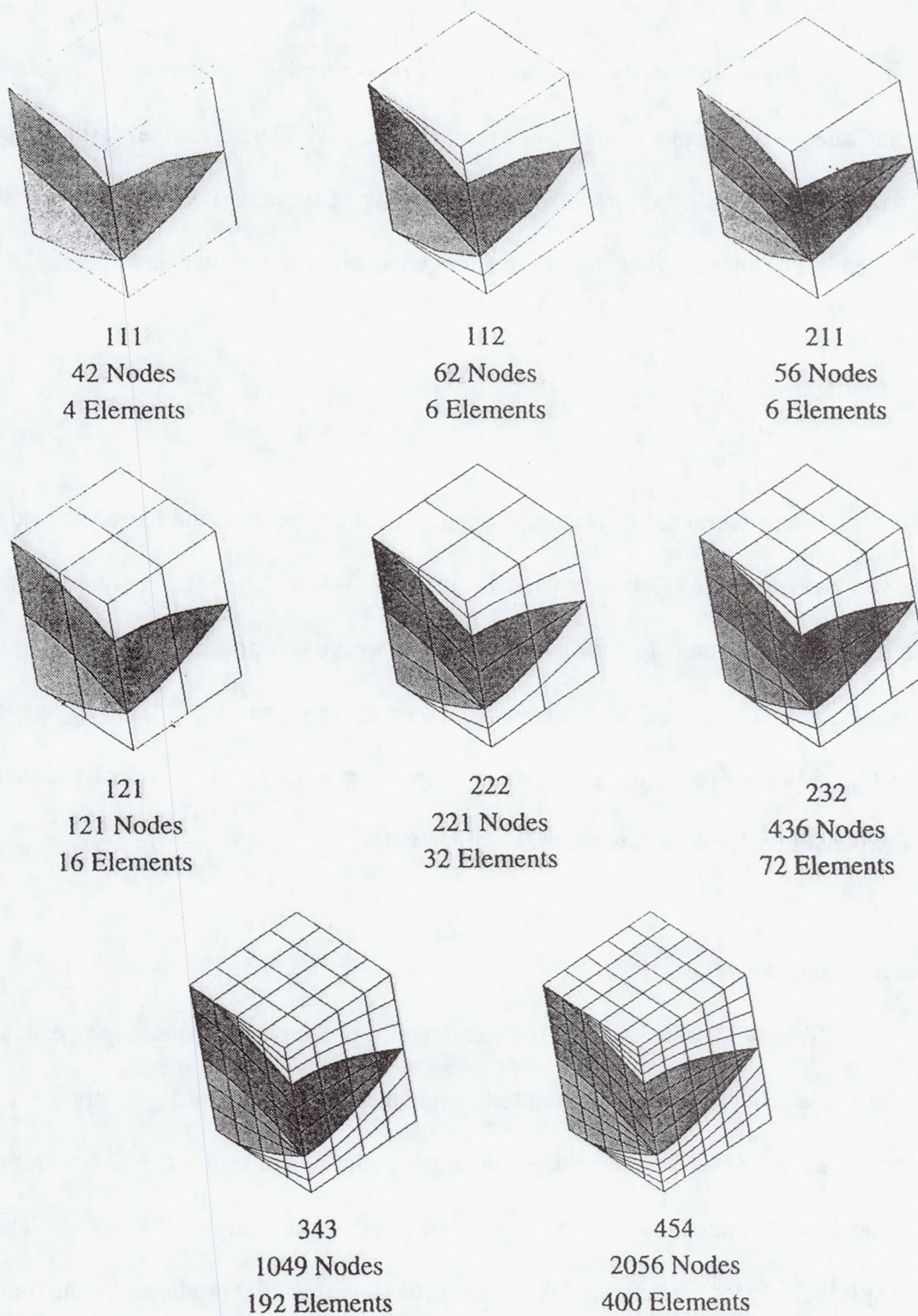
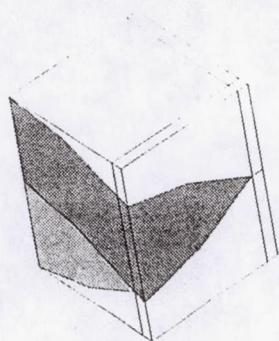
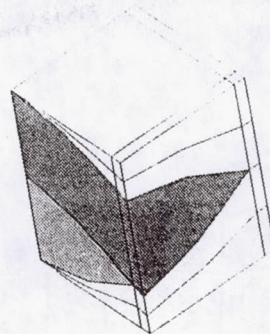


Figure 3.18: Meshes used in convergence study for translated tows. Elements are 3D 20-node hexahedrals.

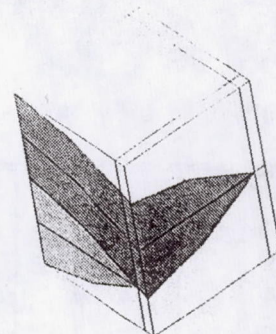




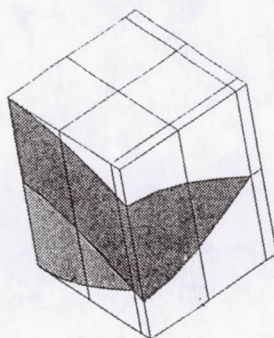
111  
105 Nodes  
16 Elements



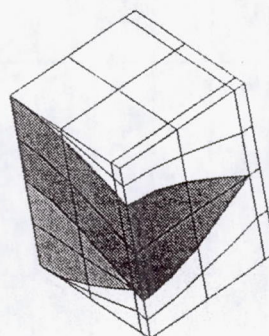
112  
161 Nodes  
24 Elements



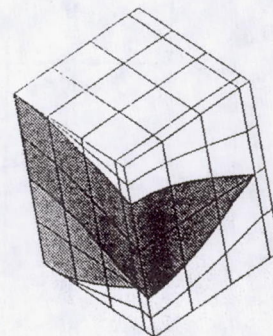
211  
127 Nodes  
20 Elements



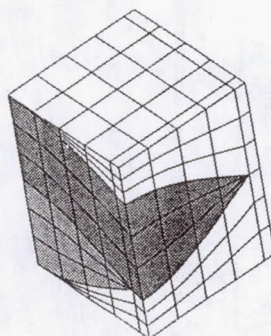
121  
228 Nodes  
39 Elements



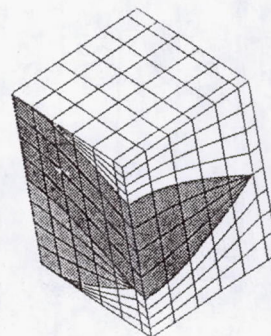
222  
396 Nodes  
69 Elements



232  
687 Nodes  
128 Elements



343  
1500 Nodes  
295 Elements



454  
2763 Nodes  
564 Elements

Figure 3.19: Meshes used in convergence study for extruded tows. Elements are 3D 20-node hexahedrals.



Table 3.3: Convergence of moduli with model type for translated model with single angle approximation and  $WR = 1/3$ .

Translated Model with Single Angles						
Model	$E_x$ (GPa)	$E_z$ (GPa)	$G_{xy}$ (GPa)	$G_{xz}$ (GPa)	$\nu_{xy}$	$\nu_{xz}$
111	25.95	4.77	1.9567	2.7233	0.0002	0.8808
112	25.93	4.77	1.9567	2.7165	0.0002	0.8801
211	25.14	4.76	1.9549	2.6966	0.0020	0.8603
121	25.92	4.78	1.9462	2.5220	0.1049	0.8450
222	25.45	4.78	1.9453	2.4968	0.1064	0.8340
232	26.48	4.78	1.9443	2.4855	0.1201	0.8613
343	26.93	4.78	1.9439	2.4753	0.1256	0.8733
454	N/A	N/A	1.9437	2.4698	N/A	N/A



Table 3.4: Convergence of moduli with model type for translated model with multiple angle approximation and  $WR = 1/3$ .

Translated Model with Multiple Angles						
Model	$E_x$ (GPa)	$E_z$ (GPa)	$G_{xy}$ (GPa)	$G_{xz}$ (GPa)	$\nu_{xy}$	$\nu_{xz}$
111	29.45	4.80	1.9566	2.6428	0.0940	0.9384
112	N/A	4.80	1.9565	2.6335	N/A	N/A
211	29.35	4.80	1.9545	2.6081	0.0937	0.9382
121	28.00	4.79	1.9462	2.5356	0.1049	0.8450
222	27.89	4.79	1.9453	2.5037	0.1326	0.8952
232	27.80	4.78	1.9443	2.4954	0.1325	0.8953
343	27.77	4.78	1.9439	2.4813	0.1327	0.8952
454	27.76	4.78	1.9437	2.4698	0.1328	0.8951



different for the multiple and single angle models. The coarse multiple angle models over predict the values of  $E_x$ , whereas the coarse single angle models under predict values for  $E_x$ . The 343 multi-angle model produces a value for  $E_x$  which is less than .04% greater than that of the 454 multi-angle model and still has only half the elements of the 454 model. Similarly for  $v_{xy}$  and  $v_{xz}$ , the 343 multi-angle model produces results which are within 1/10000th that of the 454 multi-angle model. Although the single angle model has not converged, it seems to be approaching the results predicted by the 454 multi-angle model.

As Table 3.4 shows, values for  $E_z$ ,  $G_{xy}$  can be predicted using very rough models as can be seen by the small variance of the calculated values as the model is refined. Even the 111 multi-angle model was able to predict values within 0.67% of the converged values for these two properties.

For  $G_{xy}$ , predictions converged as slowly as the values for  $E_x$ ,  $v_{xz}$ , and  $v_{xy}$ . This indicates that for these for properties, a fairly refined mesh is needed. Therefore, for moduli comparison in the results section, the 343 multi-angle model will be used since values predicted by it differ by less than 1% from those of the 454 model, which requires substantially higher ammounts of memory and CPU time.

#### *Extruded Model*

Convergence of the extruded model with multiple angles was as fast or faster than the translated model with multiple angles as shown in Table 3.5 and 3.6 due to the higher number of elements in an extruded model compared to like translated models.



Table 3.5: Convergence of moduli with model type for extruded model with single angle approximation and  $WR = 1/3$ .

Extruded Model with Single Angles						
Model	$E_x$ (GPa)	$E_z$ (GPa)	$G_{xy}$ (GPa)	$G_{xz}$ (GPa)	$\nu_{xy}$	$\nu_{xz}$
111	N/A	N/A	1.9065	2.6137	N/A	N/A
112	24.39	4.73	1.9062	2.6113	0.0541	0.8235
211	23.86	4.73	1.9058	2.5866	0.0505	0.8097
121	24.86	4.74	1.8999	2.4781	0.1208	0.8246
222	24.45	4.73	1.8993	2.4530	0.1223	0.8151
232	26.04	4.73	1.8988	2.4481	0.1356	0.8386
343	25.63	4.73	1.8986	2.4387	0.1411	0.8518
454	25.82	N/A	1.8985	2.4353	0.1437	0.8530

Table 3.6: Convergence of moduli with model type for extruded model with multiple angle approximation and  $WR = 1/3$ .

Extruded Model with Multiple Angles						
Model	$E_x$ (GPa)	$E_z$ (GPa)	$G_{xy}$ (GPa)	$G_{xz}$ (GPa)	$\nu_{xy}$	$\nu_{xz}$
111	27.05	4.75	1.9064	2.5140	0.1290	0.8837
112	27.04	4.75	1.9061	2.5112	0.1292	0.8836
211	26.94	4.74	1.9054	2.4812	0.1291	0.8828
121	26.21	4.73	1.8999	2.4456	0.1499	0.8612
222	26.01	4.73	1.8993	2.4199	0.1504	0.8586
232	25.30	4.73	1.8987	2.4184	0.1506	0.8582
343	26.01	4.72	1.8985	2.4032	0.1509	0.8678
454	26.00	N/A	1.8984	N/A	0.1509	0.8678



Consequently, the 343 multi-angle model will also be used for prediction of material properties for the extruded model.

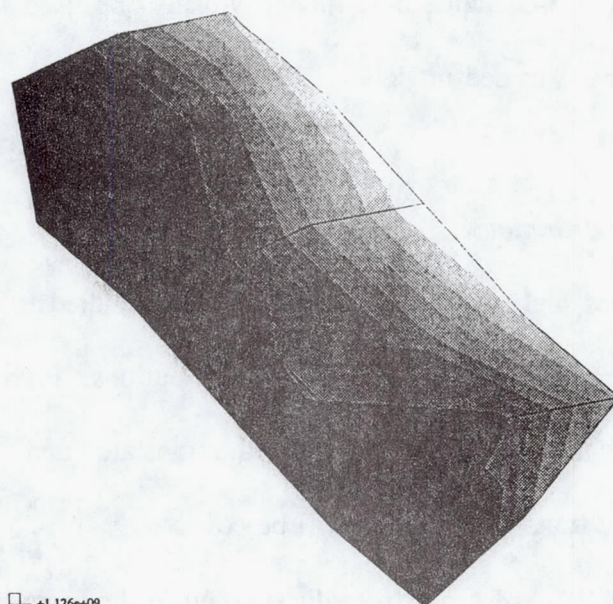
### 3.5.2 Stress Distributions

Translated and extruded meshes were also studied to determine the refinement required for adequate analysis of the stress distributions. Figure 3.18 and 3.19 show the meshes used for the convergence study of the translated and extruded meshes. For this subsection, only translated meshes will be covered.

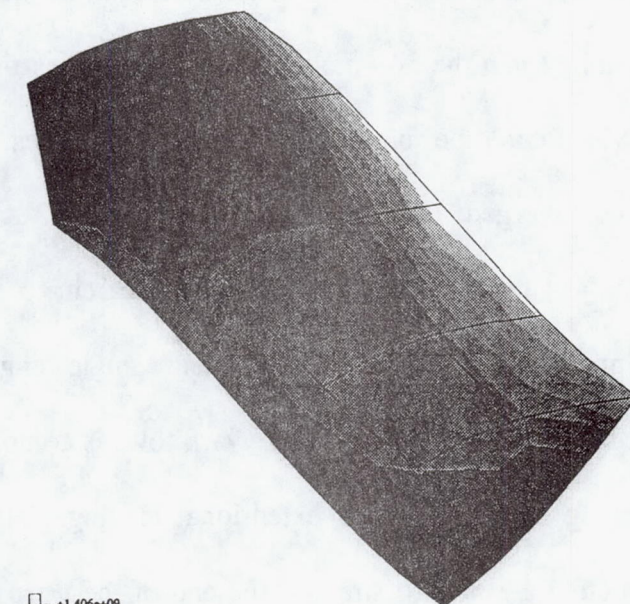
Figure 3.20 shows  $\sigma_{xx}$  stress distribution in the warp tows for various translated meshes subjected to a 1% extensional loading in the warp direction. As can be seen from the figure, the 111 model stress distribution is in no way converged as compared to the 454 model. Even the 343 model is not the same as the 454 model which is the largest mesh which could be run with the available resources. Although the meshes are not completely converged, the difference between the 343 and 454 is small enough to suggest that the 454 model is sufficient for this research.

A comparison of the multi-angle and single angle elements is given in Figure 3.21. In this figure, the  $\sigma_{xx}$  in the warp tows is compared for the 454 translated model after being subject to a 1% extensional loading. Notice that the single angle model is predicting a non-zero stress at the end of the warp tow which should be zero due to symmetry. To get rid of this error using the single angle approximation, substantial mesh refinement would be necessary at the ends of the tow. For this reason, the multi-angle 454 model will be used to evaluate the stress distributions in the RVE.





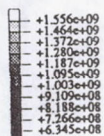
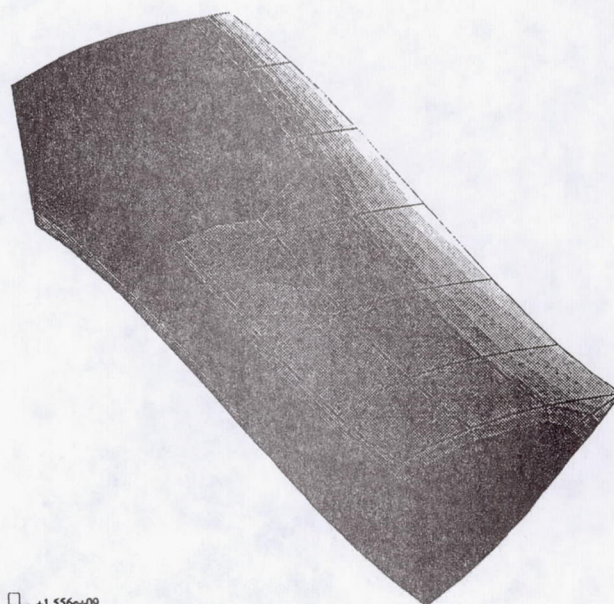
Mesh: 111



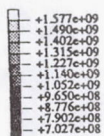
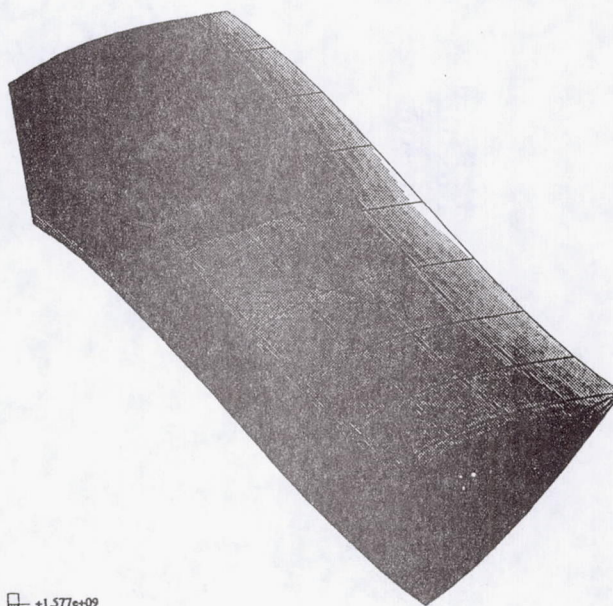
Mesh: 121

Figure 3.20: Convergence of  $\sigma_{xx}$  stress distributions in warp tows of translated meshes. Meshes were subjected to 1%  $\epsilon_{xx}$ .





Mesh: 232



Mesh: 343

Figure 3.20: (continued)

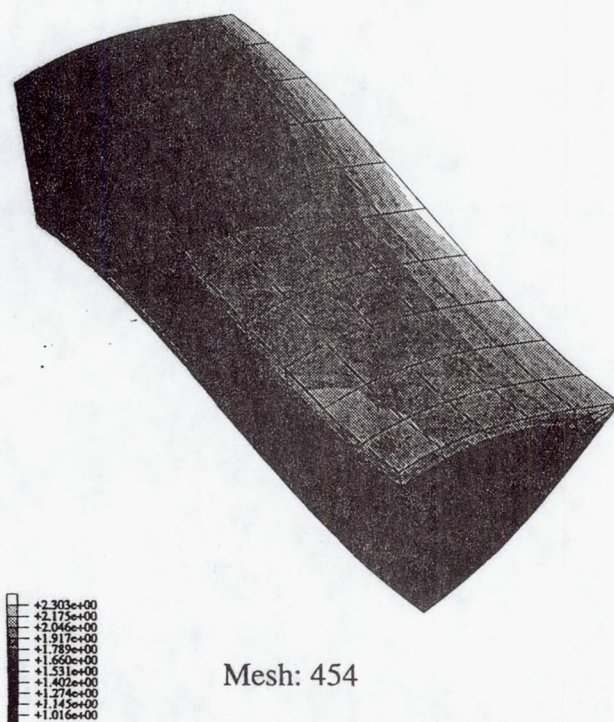


Figure 3.20: (continued)



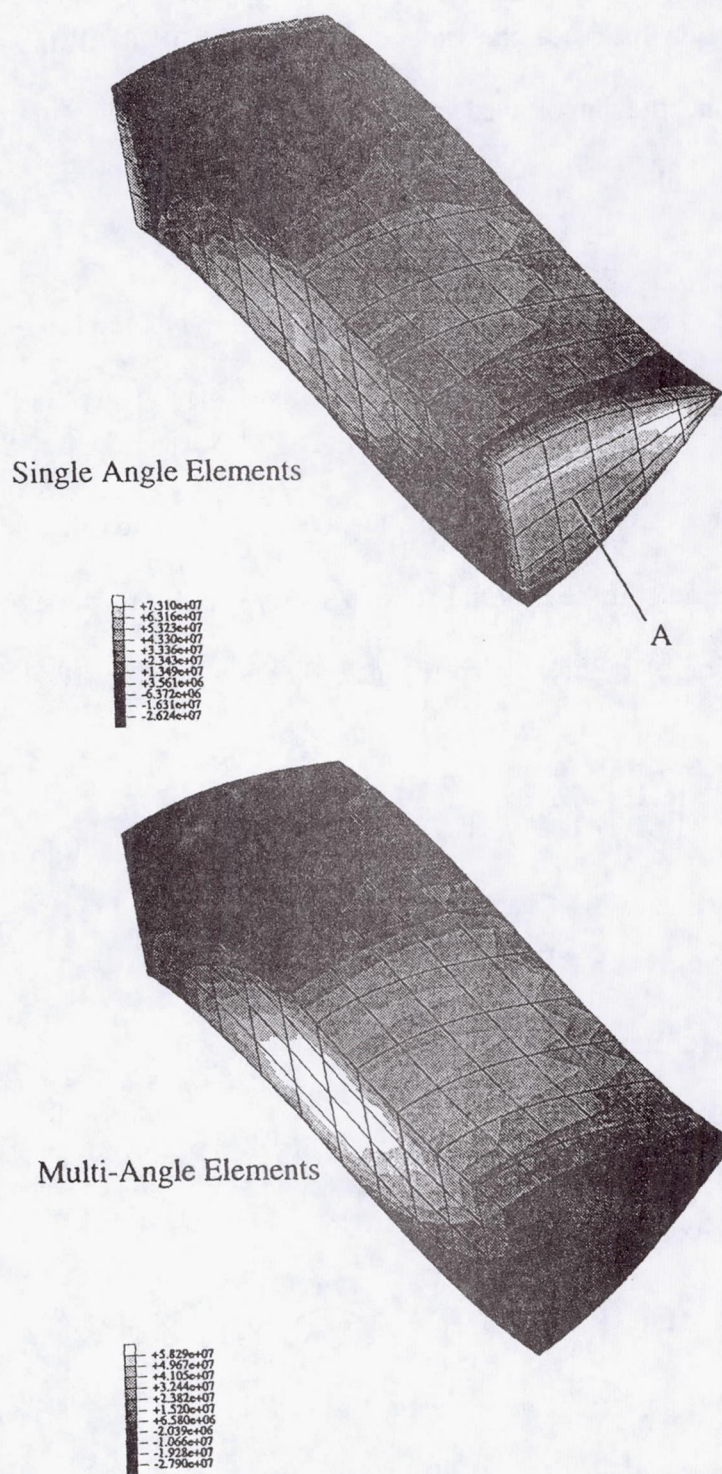


Figure 3.21: Comparison of multi-angle and single angle elements in translated 454 models subjected to 1%  $\epsilon_{xx}$  strain. Notice that single angle model predicts non-zero stress at 'A'.



### 3.6 Failure Criteria

For this research, a modification of the Tsai-Hill failure criteria will be used to determine the importance of the calculated stresses. The Tsai-Hill failure criteria predicts failure if

$$\begin{aligned} & \left( \frac{\sigma_{11}}{X} \right)^2 + \left( \frac{\sigma_{22}}{Y} \right)^2 + \left( \frac{\sigma_{33}}{Z} \right)^2 - \left( \frac{1}{X^2} + \frac{1}{Y^2} - \frac{1}{Z^2} \right) \sigma_{11} \sigma_{22} - \left( \frac{1}{X^2} - \frac{1}{Y^2} + \frac{1}{Z^2} \right) \sigma_{11} \sigma_{33} - \\ & \left( -\frac{1}{X^2} + \frac{1}{Y^2} + \frac{1}{Z^2} \right) \sigma_{22} \sigma_{33} + \left( \frac{\sigma_{12}}{S_{12}} \right)^2 + \left( \frac{\sigma_{13}}{S_{13}} \right)^2 + \left( \frac{\sigma_{23}}{S_{23}} \right)^2 \geq 1 \end{aligned} \quad 3.6.1$$

The values for  $X$ ,  $Y$ , and  $Z$  are the average of the tensile and compressive strengths of the material. If the material strengths vary greatly, this model may not provide adequate prediction of failure. Woo [8] instead uses a modified Tsai-Hill criteria given by

$$\begin{aligned} & \left( \frac{\sigma_{11}}{X} \right)^2 + \left( \frac{\sigma_{22}}{Y} \right)^2 + \left( \frac{\sigma_{33}}{Z} \right)^2 - \left( \frac{1}{X_0^2} + \frac{1}{Y_0^2} - \frac{1}{Z_0^2} \right) \sigma_{11} \sigma_{22} - \left( \frac{1}{X_0^2} - \frac{1}{Y_0^2} + \frac{1}{Z_0^2} \right) \sigma_{11} \sigma_{33} - \\ & \left( -\frac{1}{X_0^2} + \frac{1}{Y_0^2} + \frac{1}{Z_0^2} \right) \sigma_{22} \sigma_{33} + \left( \frac{\sigma_{12}}{S_{12}} \right)^2 + \left( \frac{\sigma_{13}}{S_{13}} \right)^2 + \left( \frac{\sigma_{23}}{S_{23}} \right)^2 \geq 1 \end{aligned} \quad 3.6.2$$

where, for tension

$$X = X_t, Y = Y_t, Z = Z_t \quad 3.6.3$$

and for compression

$$X = X_c, Y = Y_c, Z = Z_c \quad 3.6.4$$

Also, the values for  $X_0$ ,  $Y_0$  and  $Z_0$  are given by



$$X_0 = \frac{X_t + X_c}{2}, Y_0 = \frac{Y_t + Y_c}{2}, Z_0 = \frac{Z_t + Z_c}{2} \quad 3.6.5$$

This theory is based on Von Mises isotropic yield criteria and should provide adequate predictions of failure [9].

If two models are compared at the same macroscopic strain and one predicts a maximum failure criteria of  $T_1$  and the second predicts a maximum failure criteria of  $T_2$ , then the percent difference in the macroscopic strain to failure would be valuable to know. For linear elasticity, the strains in the material vary linearly with changes in the applied macroscopic strain and can be written as

$$\epsilon_{ij} = \lambda_{ij} \bar{\epsilon} \quad 3.6.6$$

The stresses at any point are related to the strains by

$$\sigma_{ij} = C_{ijkl} \epsilon_{kl} \quad 3.6.7$$

Substituting (3.6.6) into (3.6.7) gives

$$\sigma_{ij} = C_{ijkl} \lambda_{kl} \bar{\epsilon} \quad 3.6.8$$

Substituting (3.6.8) into (3.6.5) gives

$$\begin{aligned} & \left( \frac{C_{11kl} \lambda_{kl} \bar{\epsilon}}{X} \right)^2 + \left( \frac{C_{22kl} \lambda_{kl} \bar{\epsilon}}{Y} \right)^2 + \left( \frac{C_{33kl} \lambda_{kl} \bar{\epsilon}}{Z} \right)^2 - \left( \frac{1}{X_0^2} + \frac{1}{Y_0^2} - \frac{1}{Z_0^2} \right) C_{11kl} \lambda_{kl} C_{22mn} \lambda_{mn} \bar{\epsilon}^2 - \\ & \left( \frac{1}{X_0^2} - \frac{1}{Y_0^2} + \frac{1}{Z_0^2} \right) C_{11kl} \lambda_{kl} C_{33mn} \lambda_{mn} \bar{\epsilon}^2 - \left( -\frac{1}{X_0^2} + \frac{1}{Y_0^2} + \frac{1}{Z_0^2} \right) C_{22kl} \lambda_{kl} C_{33mn} \lambda_{mn} \bar{\epsilon}^2 + \quad 3.6.9 \\ & \left( \frac{C_{12kl} \lambda_{kl} \bar{\epsilon}}{S_{12}} \right)^2 + \left( \frac{C_{13kl} \lambda_{kl} \bar{\epsilon}}{S_{13}} \right)^2 + \left( \frac{C_{23kl} \lambda_{kl} \bar{\epsilon}}{S_{23}} \right)^2 \geq 1 \end{aligned}$$

Factoring out  $\bar{\epsilon}^2$  gives

$$\begin{aligned} & \left[ \left( \frac{C_{11kl}\lambda_{kl}}{X} \right)^2 + \left( \frac{C_{22kl}\lambda_{kl}}{Y} \right)^2 + \left( \frac{C_{33kl}\lambda_{kl}}{Z} \right)^2 - \left( \frac{1}{X_0^2} + \frac{1}{Y_0^2} - \frac{1}{Z_0^2} \right) C_{11kl}\lambda_{kl}C_{22mn}\lambda_{mn} - \right. \\ & \left. \left( \frac{1}{X_0^2} - \frac{1}{Y_0^2} + \frac{1}{Z_0^2} \right) C_{11kl}\lambda_{kl}C_{33mn}\lambda_{mn} - \left( -\frac{1}{X_0^2} + \frac{1}{Y_0^2} + \frac{1}{Z_0^2} \right) C_{22kl}\lambda_{kl}C_{33mn}\lambda_{mn} + \right. \\ & \left. \left( \frac{C_{12kl}\lambda_{kl}}{S_{12}} \right)^2 + \left( \frac{C_{13kl}\lambda_{kl}}{S_{13}} \right)^2 + \left( \frac{C_{23kl}\lambda_{kl}}{S_{23}} \right)^2 \right] \bar{\epsilon}^2 \geq 1 \end{aligned} \quad 3.6.10$$

The portion of the equation in brackets is constant as long as  $\bar{\epsilon}$  doesn't change sign and can be replaced by a constant  $S_0$ . Which gives

$$S_0 \bar{\epsilon}^2 \geq 1 \quad 3.6.11$$

At  $\bar{\epsilon}_1$  and  $\bar{\epsilon}_2$  eqn. (3.6.11) gives

$$S_{0_1} \bar{\epsilon}_1^2 = T_1, \quad S_{0_2} \bar{\epsilon}_2^2 = T_2 \quad 3.6.12$$

Solving for  $S_0$  gives

$$S_{0_1} = \frac{T_1}{\bar{\epsilon}_1^2}, \quad S_{0_2} = \frac{T_2}{\bar{\epsilon}_2^2} \quad 3.6.13$$

If  $\bar{\epsilon}_f$  is the macroscopic strain to failure then at failure,

$$S_{0_1} \bar{\epsilon}_{f_1}^2 = 1, \quad S_{0_2} \bar{\epsilon}_{f_2}^2 = 1 \quad 3.6.14$$

The percent difference of  $\bar{\epsilon}_{f_1}$  to  $\bar{\epsilon}_{f_2}$  is given by



$$\%difference = 100 \times \frac{\bar{\epsilon}_{f_1} - \bar{\epsilon}_{f_2}}{\bar{\epsilon}_{f_2}} \quad 3.6.15$$

Substituting (3.6.14) into (3.6.15) gives

$$\%difference = 100 \times \frac{\sqrt{\frac{1}{S_{0_1}}} - \sqrt{\frac{1}{S_{0_2}}}}{\sqrt{\frac{1}{S_{0_2}}}} \quad 3.6.16$$

Rewriting gives

$$\%difference = 100 \times \left( S_{0_2} \sqrt{\frac{1}{S_{0_1} S_{0_2}}} - 1 \right) \quad 3.6.17$$

Substituting in (3.6.13) gives

$$\%difference = 100 \times \left( \sqrt{\frac{T_2}{T_1}} - 1 \right) \quad 3.6.18$$

which is the percent difference of  $\bar{\epsilon}_{f_1}$  to  $\bar{\epsilon}_{f_2}$  in terms of the maximum predicted failure criteria using the Tsai-Hill theory. This equation will be used to help in the comparison of the extruded and translated models in the following chapter.

## IV. RESULTS AND DISCUSSION

The previous chapters detail how an analysis may be performed on woven composites using finite elements. By using the discussed mesh generation techniques and applying boundary conditions for desired loadings, almost any plain weave composite can be analyzed. The following is a comparison of translated and extruded tows at various waviness-ratios. The tows have a lenticular cross-section, and the cross-section is constant along the tow path. The tow path is sinusoidal for both the extruded and translated models.

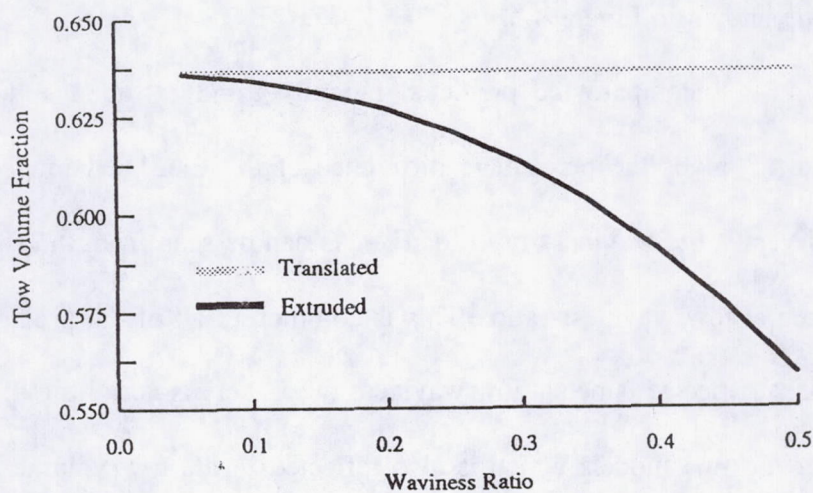
Analysis of extruded and translated tows is performed in order to determine the differences in predicted elastic properties as well as stress distributions in the composite. Comparison will be made between  $1/3$ ,  $1/6$  and  $1/20$  waviness-ratios of extruded and translated tow types.

### 4.1 Elastic Properties

The volume fraction of extruded and translated tows is compared at different waviness-ratio in Figure 4.1. This figure shows that the translated tow always contains the same amount of tow regardless of change in waviness-ratio. This is obviously incorrect, and is due to the fact that the cross-section shape is not being modelled correctly. As waviness-ratio is increased, the volume fraction of the extruded tow drops off. This alone should cause a notable difference in the predicted elastic properties at higher waviness-ratios.

Calculation of the elastic properties was performed using a 1/32nd 343 multiple





$v_t$  = Volume fraction of tow in translated model

$v_e$  = Volume fraction of tow in extruded model

$\Delta v = v_t - v_e$  = Tow Volume Fraction Difference

WR	$\Delta v$
1/3	2.972e-2
1/6	6.616e-3
1/20	5.5e-4

Figure 4.1: Variation of tow volume fraction with waviness ratio for extruded and translated models.



angle model for both the extruded and translated tows for all moduli and Poisson's ratios. These meshes are shown in Figure 4.2.

Figures 4.3-4.8 compare the predicted moduli of the extruded and translated models. Figure 4.3 gives the percentage difference of the translated model over the extruded model versus the waviness-ratio for  $E_x$ . As can be seen from the figure, there is little difference at low waviness-ratio. This is common to all of the predicted elastic properties. This is expected, since at low waviness ratio, there is very little difference in the geometry of the two models which is also reflected in the tow volume fraction in Figure 4.1. As waviness increases, the difference grows to around 6.8% at a waviness of  $1/3$ .

Using the rule of mixtures, the predicted difference in  $E_x$  at  $WR = 1/3$  would be 4.5%. This would seem to indicate that something in addition to tow volume fraction is causing the difference between the predicted moduli. For  $E_x$ , this difference may be caused by cushioning of the warp tows by the resin elements between the warp and fill tows of the extruded model.

For  $E_z$  there is only a 0.63% difference at  $WR = 1/3$  as shown in Figure 4.4. This is due to the fact that the tows and the resin have about the same  $E_z$ . Since there is little difference in the predicted moduli, either model would be adequate for prediction of this moduli with this material model.

Predictions of  $G_{xy}$  using the translated model are 2.4% greater than that predicted using the extruded model as shown in Figure 4.5 for  $WR = 1/3$ . Little difference in this shear modulus should be expected due to the shear moduli of the constituents being so close. Additionally, there should be little difference in the predicted values of  $G_{xz}$ .



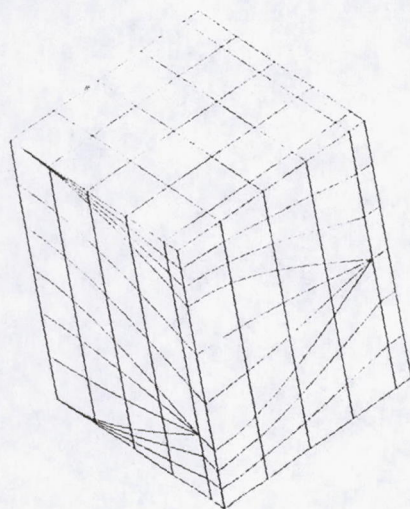
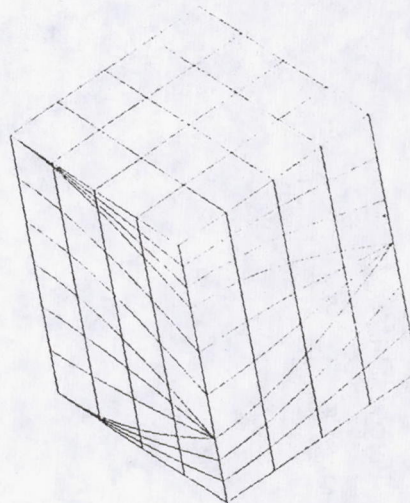
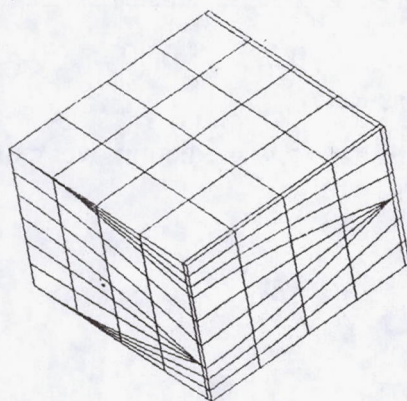
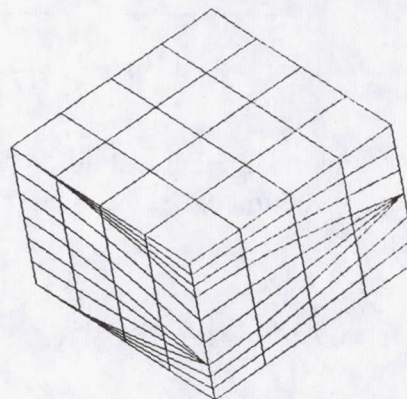
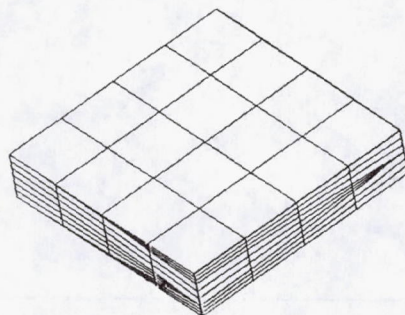
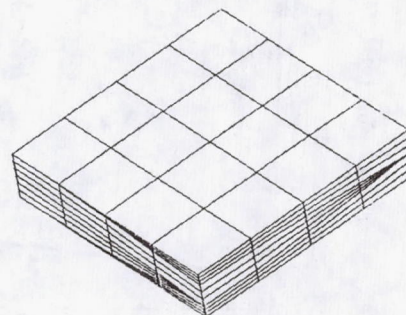
Extruded:  $WR=1/3$ Translated:  $WR=1/3$ Extruded:  $WR=1/6$ Translated:  $WR=1/6$ Extruded:  $WR=1/20$ Translated:  $WR=1/20$ 

Figure 4.2: Meshes used for calculation of elastic properties.

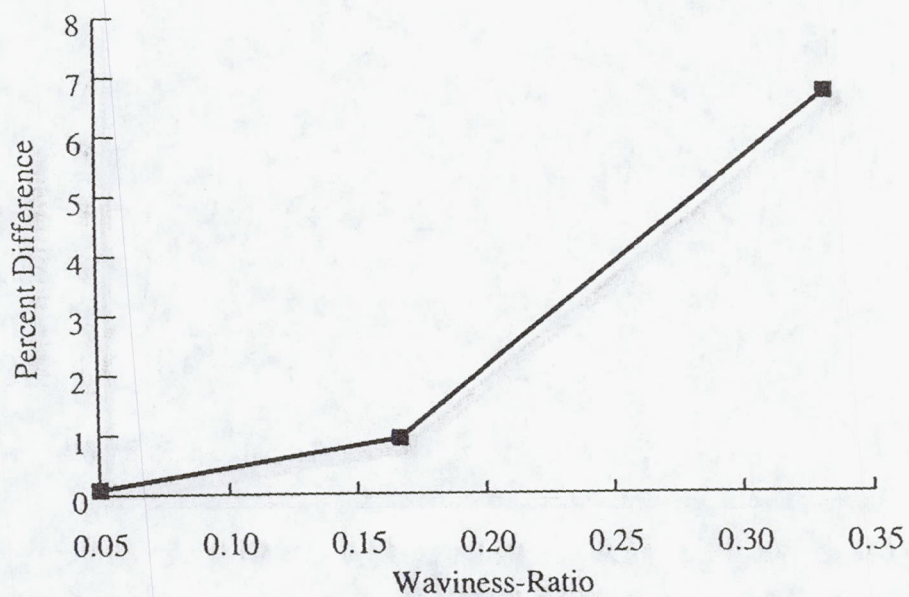


Figure 4.3: Percent difference of translated tow prediction over extruded prediction of  $E_x$ .

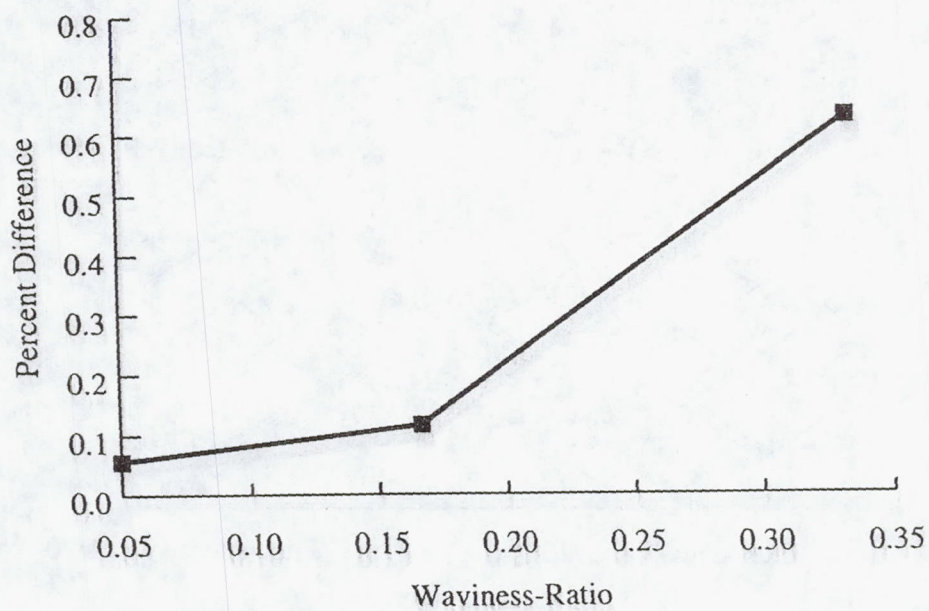


Figure 4.4: Percent difference of translated tow prediction over extruded prediction of  $E_z$ .



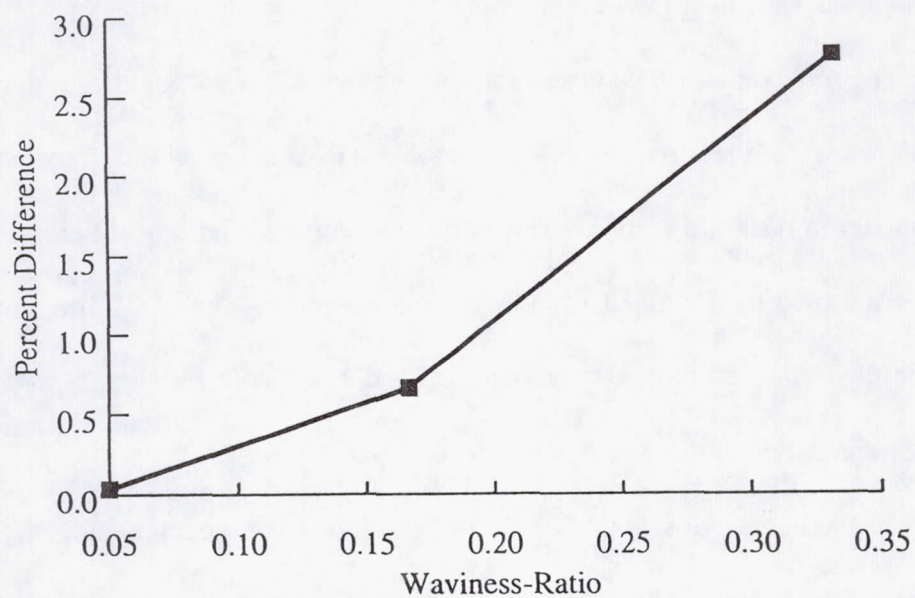


Figure 4.5: Percent difference of translated tow prediction over extruded prediction of  $G_{xz}$ .

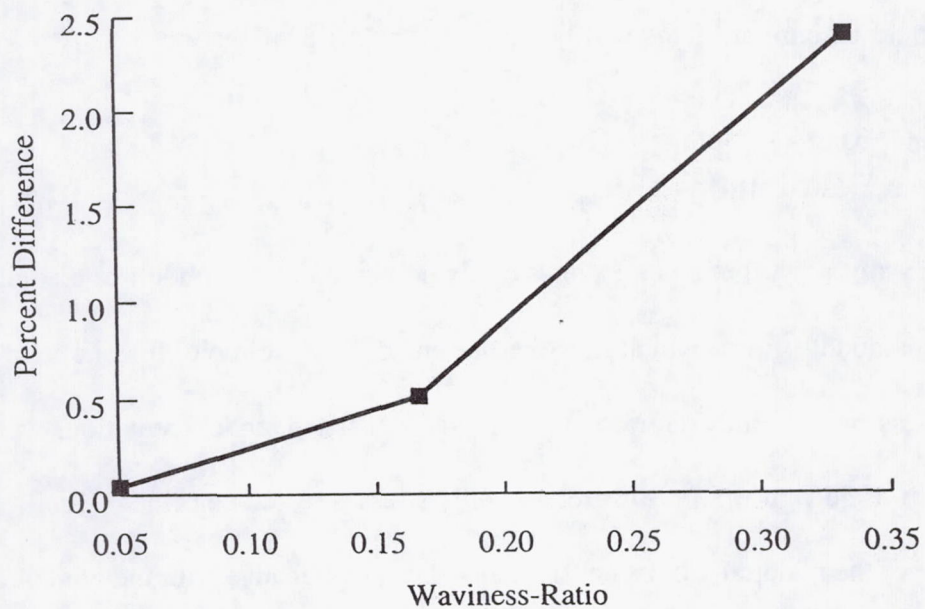


Figure 4.6: Percent difference of translated tow prediction over extruded prediction of  $G_{xy}$ .

Values for  $G_{xz}$  indicate a 3.25% higher prediction by the translated model over the extruded model as shown in Figure 4.6.

The Poisson's ratios vs. waviness-ratio in Figures 4.7 and 4.8 indicate that for an extension in the warp direction, the extruded model will contract slightly more than the translated model in the fill direction. This is due to the translated model being stiffer in the fill direction than the extruded model. As a consequence of the fill direction being more stiff in the translated model, the translated model will contract slightly more in the direction perpendicular to the weave where it is softer.

At low waviness-ratios, both the extruded and translated model predict very similar results. For waviness ratios of 1/6, there is less than 1% difference for all of the moduli and Poisson's ratios. One would expect that since such little difference is being noted in the elastic properties between the two models, the stress distributions inside the two models would be similar. This will be discussed in the next section.

## 4.2 Stress Distributions

The stress distributions are not as easily compared as the moduli of the composite due to the amount of data which must be presented. For example, for one load case at one waviness-ratio, to fully compare extruded and translated model predictions would take a minimum of 36 figures. For this reason, only stresses which contribute significantly to the failure of the material will be considered. These will change with the type of loading. A presentation of the differences at a waviness-ratio of 1/3 will be presented, followed by waviness-ratios of 1/6 and 1/20, respectively.



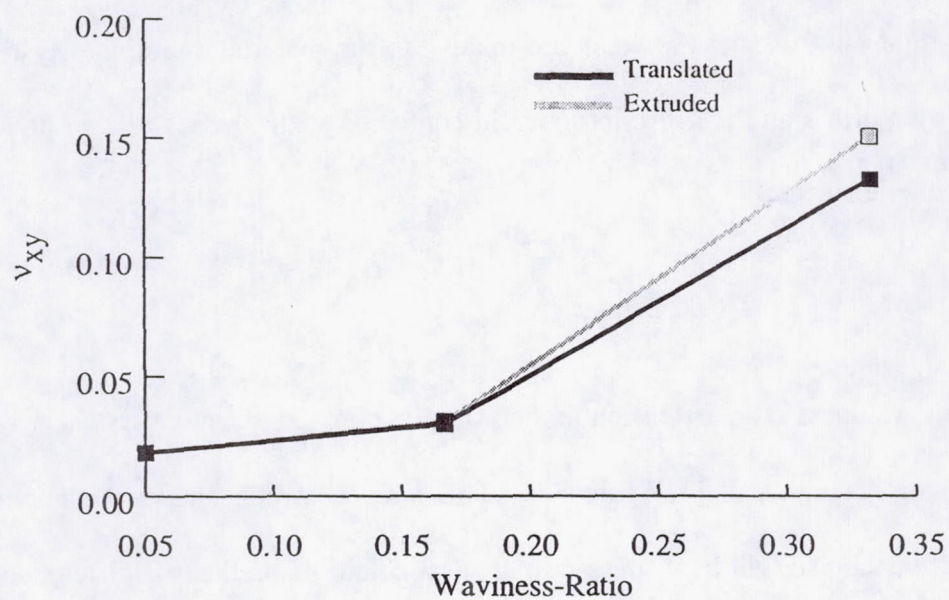


Figure 4.7: Comparison of prediction of  $v_{xy}$  by translated and extruded models.

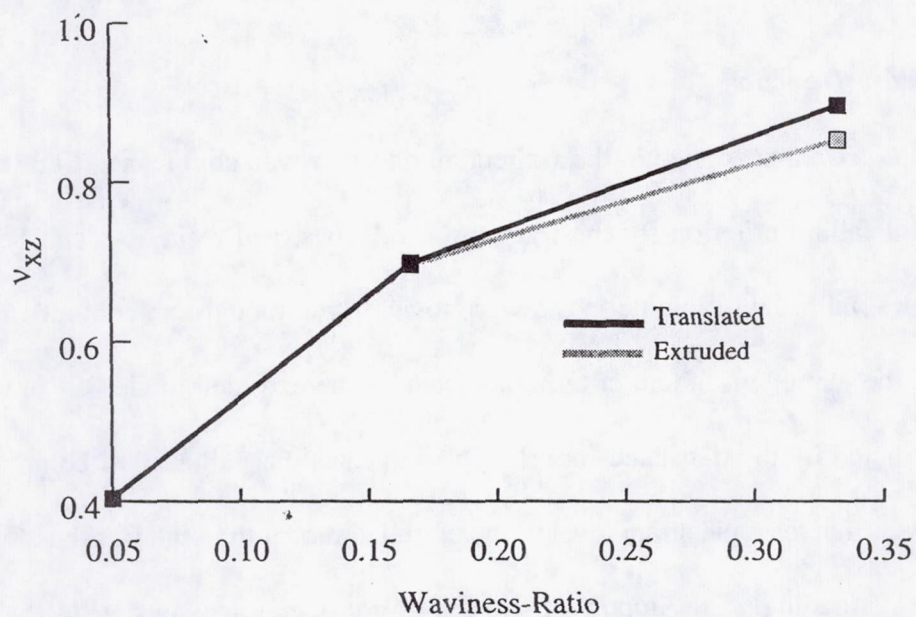


Figure 4.8: Comparison of prediction of  $v_{xz}$  by translated and extruded models.

The stress contours are plotted relative to the material coordinate system for the different constituents. All stresses which are relative to the material coordinate system are signified by a prime on the subscript to avoid confusion with stresses relative to the physical coordinate system.

#### 4.2.1 $WR = 1/3$

For this waviness ratio, extension in the warp direction,  $xz$  shear and  $xy$  shear will be presented for the unit cell in Figure 4.9. This waviness ratio shows the greatest amount of difference and will be discussed in greatest detail. Note that the difference in tow volume fraction is shown in Figure 4.1. Again, this difference should cause some difference between the two models.

#### *Loading in Warp Direction*

A 1%  $\epsilon_{xx}$  strain is applied in the  $x$  direction on the woven composite. Figure 4.10 gives Tsai-Hill failure criterion for the warp tows, fill tows, and resin. As can be seen from the figure, failure will initiate in the warp tows. Even though the contours appear very similar, the maximum failure criteria predicted by the extruded model is 7% higher than that predicted by the translated model. This indicates that failure will be predicted at a 3.3% lower macroscopic strain level in the extruded model than the translated model for this type of loading. The important stresses to consider for extension in the warp direction are determined by normalizing each stress with its appropriate strength as given in the previous chapter.

If the maximum normalized stresses are examined for the warp tows, it can be



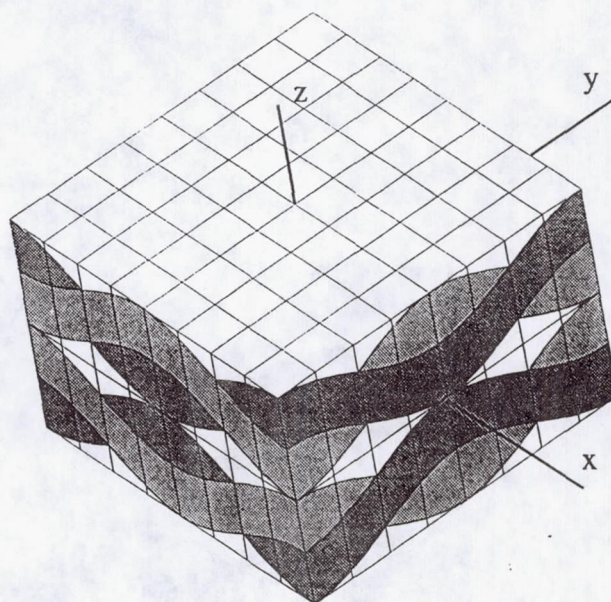
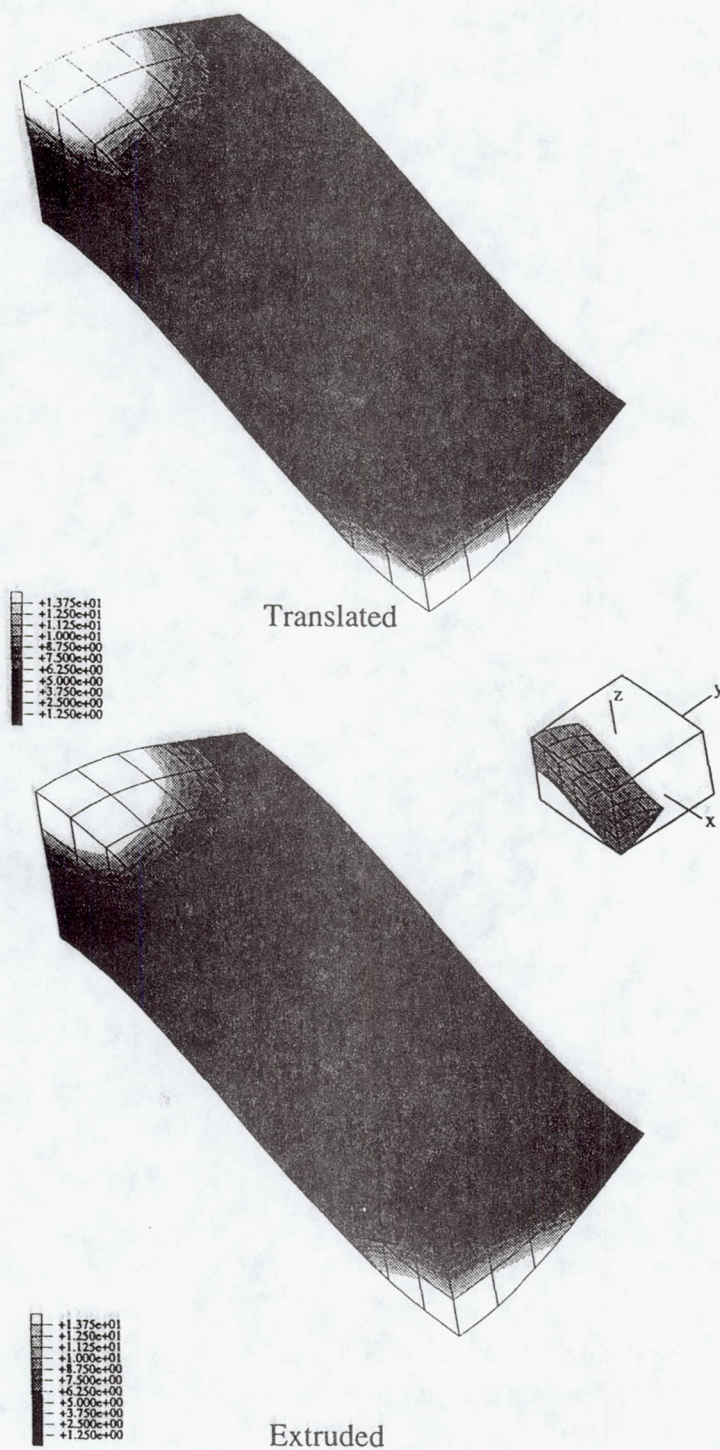


Figure: 4.9: Unit cell used for analysis of plain weave symmetrically stacked woven composite.

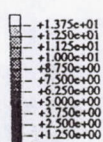
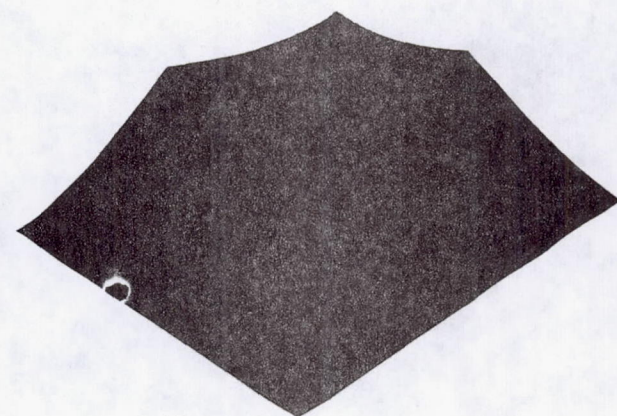




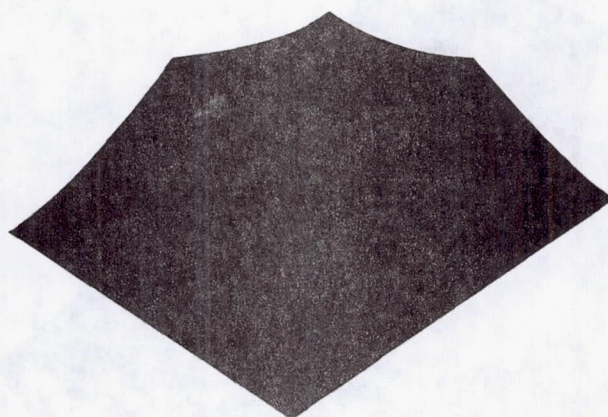
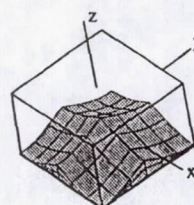
(a) Warp tows.

Figure 4.10: Comparison of Tsai-Hill failure criteria predicted with translated and extruded models after subjecting RVE to 1%  $\epsilon_{xx}$ .





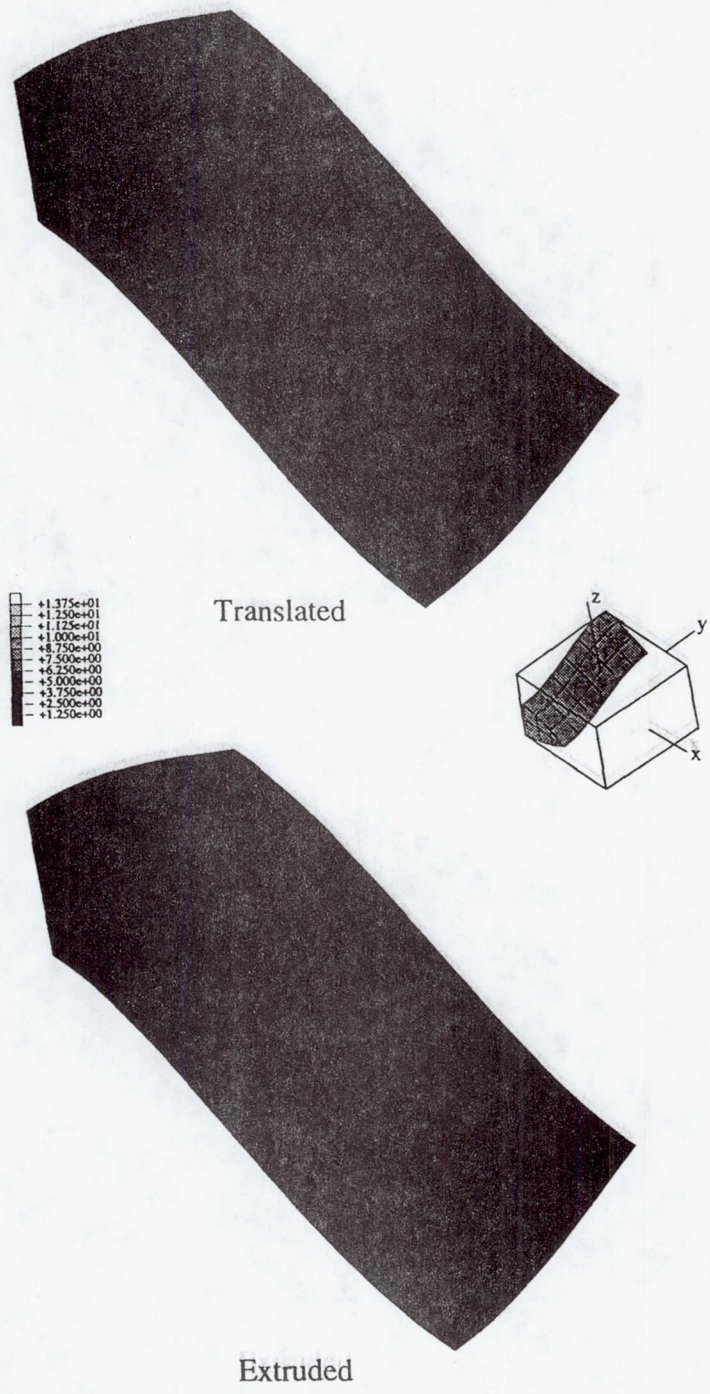
Translated



Extruded

(b) Resin

Figure 4.10: (continued)



(c) Fill Tow

Figure 4.10: (continued)



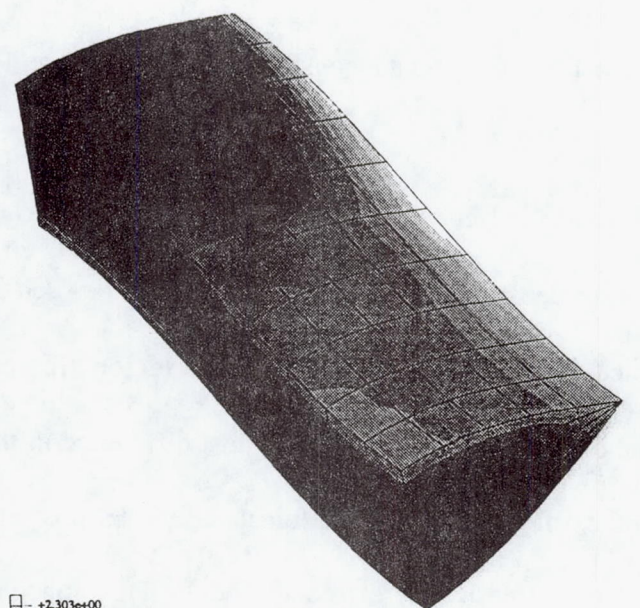
seen that the main contributors to the failure are the  $\sigma_{zz}$  and  $\sigma_{xx}$  stresses. These stresses appear to be the most important and consequently, only these two stresses will be presented.

Figures 4.11 and 4.12 compare the normalized  $\sigma_{xx}$  and  $\sigma_{zz}$  stress distributions generated with the extruded and translated models. As can be seen from Figure 4.11, the  $\sigma_{xx}$  stresses predicted for the warp tows in the failure region are very similar. It is only near the edge of the tow where one can see the most difference in the stress distributions of the translated and extruded models. The translated model predicts a high stress in this region which is not predicted by the extruded model. This concentration appears to be caused by the fill tows shearing this region which, when rotated to the material coordinate system, appears as a  $\sigma_{xx}$  concentration. The extruded model has a resin region in between the fill tows, so does not experience this concentration.

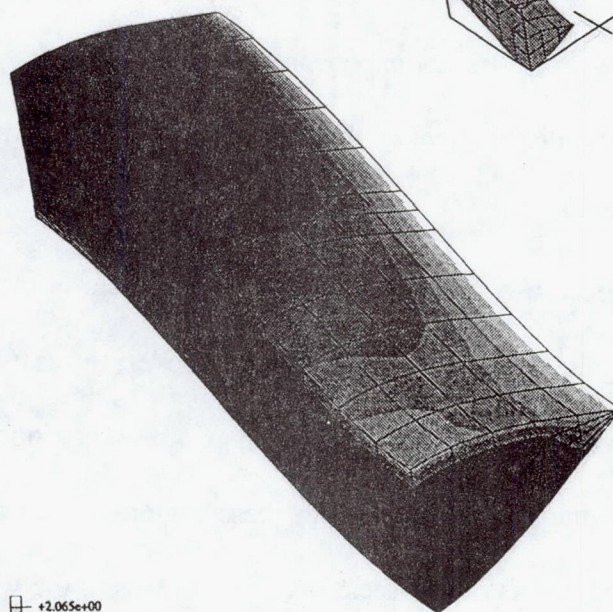
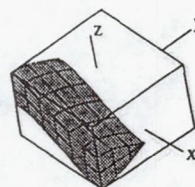
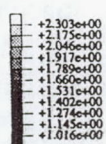
The  $\sigma_{xx}$  stress distributions in the fill tows will be ignored since the distributions are very similar.

The normalized  $\sigma_{xx}$  stress distributions for the resin in the two model are shown in Figure 4.11. Again, these are very similar. However, the extruded model shows four regions of stress which are experiencing a strange stress distribution as indicated by the letter 'A'. This is due to bad elements in these regions which are causing a localized disturbance. The elements do not seem to affect stresses in the warp and fill tows or the rest of the resin which are about two elements away from this region. Therefore, the stresses in these regions will be ignored. The rest of the resin is about the same in both models and uninteresting and will not be discussed.

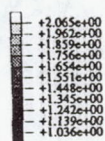




Translated



Extruded



(a) Warp Tows

Figure 4.11: Comparison of  $\sigma_{xx}$  in translated and extruded models after subjecting RVE to 1%  $\epsilon_{xx}$  strain.



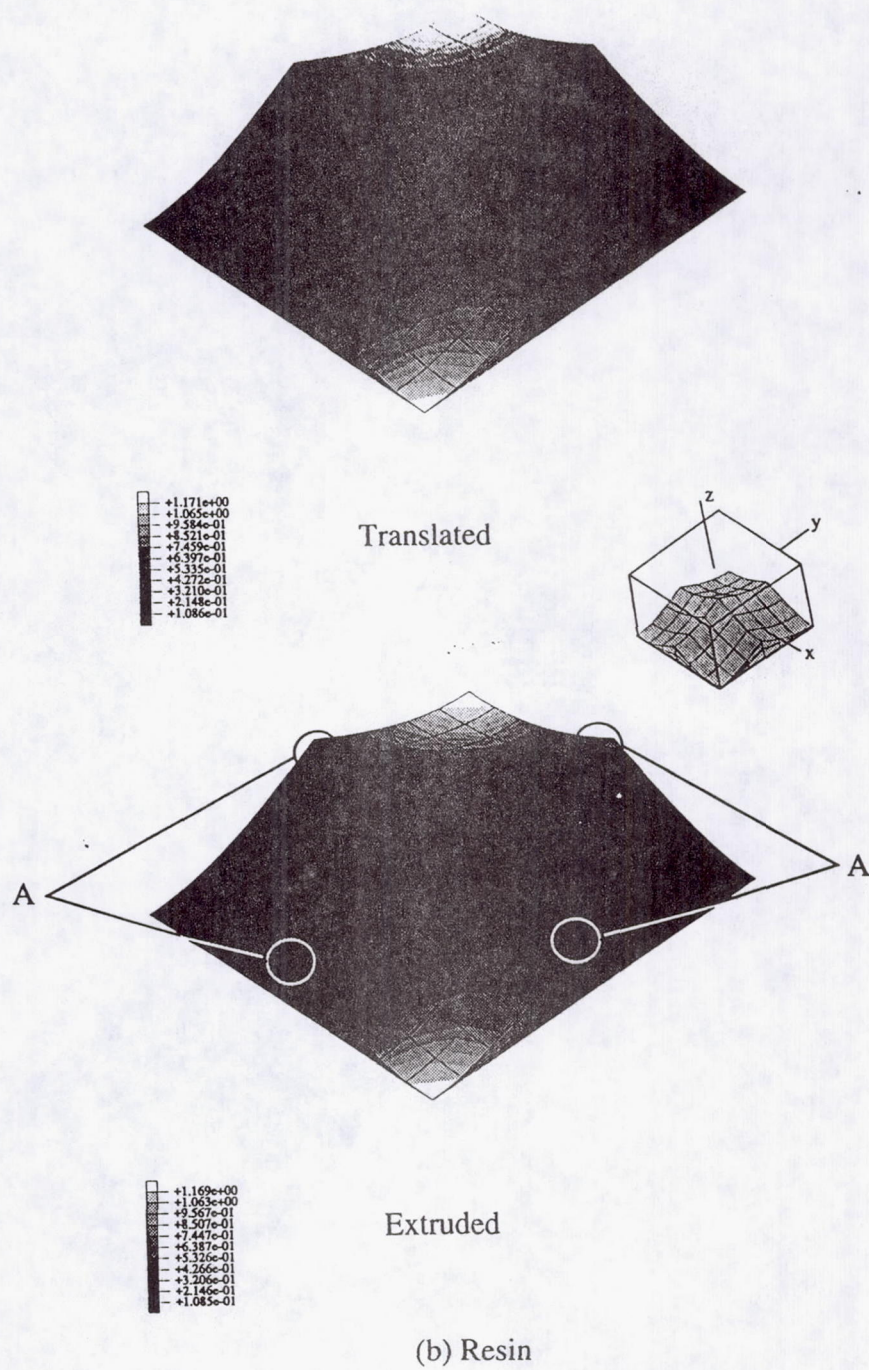


Figure 4.11: (continued)

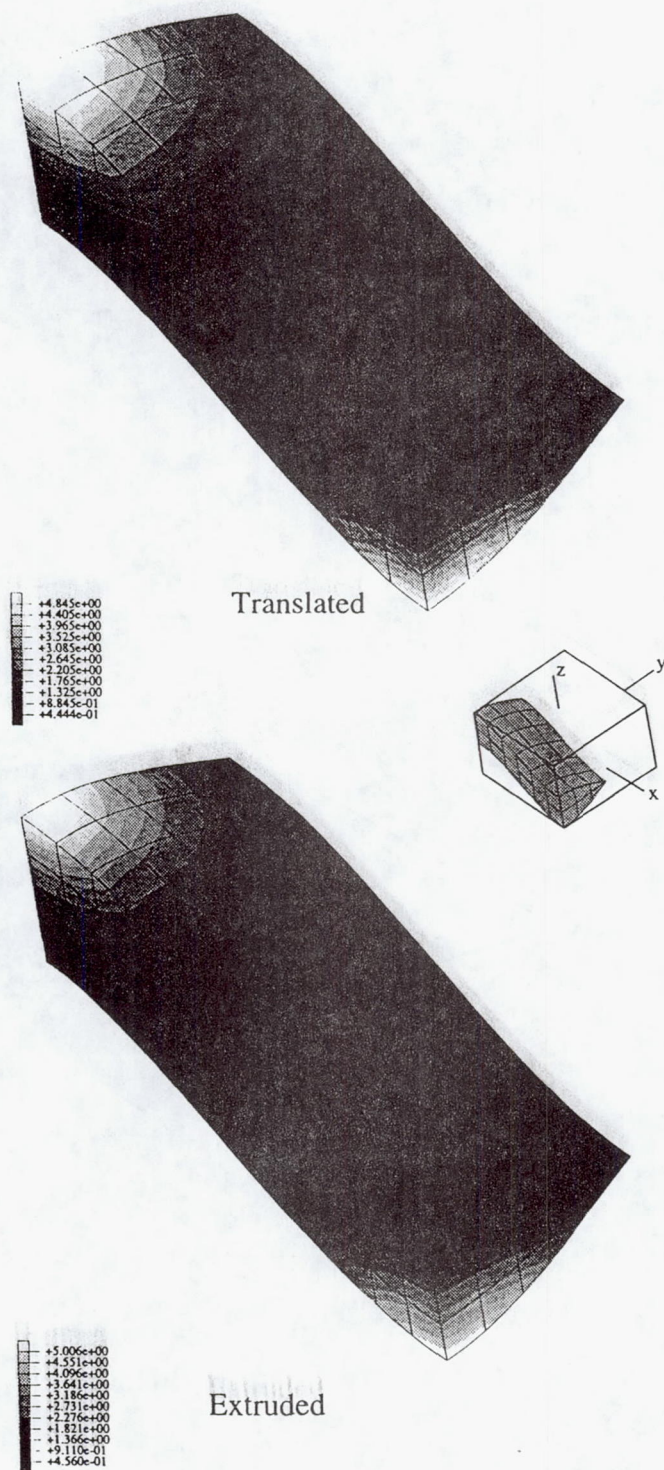


Figure 4.12: Comparison of  $\sigma_{zz}$  distributions in warp tows after subjecting RVE to 1%  $\epsilon_{xx}$  strain.



Figure 4.12 compares the normalized  $\sigma_{zz}$  distributions for the warp tows in the extruded and translated models. This stress is by far the most important for extension in the warp direction. This stress will cause a mode I crack to start between the warp tow and the resin in the region of highest concentration. This concentration is caused by the warp tows wanting to straighten. The tendency to fail in this region should change drastically if the tows are simply stacked rather than symmetrically stacked. This should be investigated in a later study. The differences in the extruded and translated model in the warp tows for  $\sigma_{zz}$  are shown in Figure 4.12. The extruded mesh shows a region which is more highly stressed than the translated. The maximum stress experienced by the extruded mesh is 3.3% higher than that predicted by the translated mesh. There is no substantial difference in the warp tow  $\sigma_{zz}$  stress distributions other than this. The  $\sigma_{zz}$  stress distributions of the fill tows and resin are uninteresting as and will not be presented.

#### *XY Loading*

The Tsai-Hill failure criteria are plotted in Figure 4.13 for a 1%  $\epsilon_{xy}$  macroscopic shear strain applied to the unit cell shown in Figure 4.9. Figure 4.13 shows that failure will initiate in the tows in the region indicated with letter 'A'. The maximum failure criteria for the translated model is 27.97% larger than the maximum predicted by the extruded model. This is a substantial difference. Using equation (3.6.18), the extruded model will fail at a macroscopic strain level 14.2% less than the translated model. This indicates a large difference between the translated and extruded modelling. If the maximum normalized stresses are examined, it is seen that the primary contributing



stresses to failure are the shearing stresses,  $\sigma_{xy}$ ,  $\sigma_{xz}$  and  $\sigma_{yz}$ . These stresses will be examined for differences between the extruded and translated models.

Since all the tows of the woven composite undergo the deformation, the fill tow will not need to be presented for any stress distribution. The normalized  $\sigma_{xy}$  distributions are shown in Figure 4.14 for the extruded and translated models. The maximum stress predicted by the translated model is 10.7% greater than that predicted by the extruded model. This indicates that the neighboring tows in the composite are highly influencing the stresses in this region. Since the extruded tows are separated by regions of resin, the extruded model will predict a higher strain to failure than that predicted by the translated model in this region.

The resin in this region is shown in Figure 4.15 for the extruded and translated models. As can be seen from the figure, both models predict similar stress patterns, except for the region in which the bad element exists in the extruded model. The translated model predicts a region which is under a higher stress than the extruded model as indicated by the white region in the plot of the translated model. This region is also where the four tows of the 1/8th unit cell cross. Since the extruded tows are separated, the extruded model is spared this high stress.

The comparison of normalized stress contours of the warp tow for  $\sigma_{yz}$  are shown in Figure 4.16. The figure shows a large difference in the stress being experienced by the tow. The extruded shows its highest concentration near the center of the tow (region 'A'), whereas the translated shows a 28.3% greater stress at the intersection of the four tows in the 1/8th unit cell at 'B'. This high stress is again caused by the tows being so close



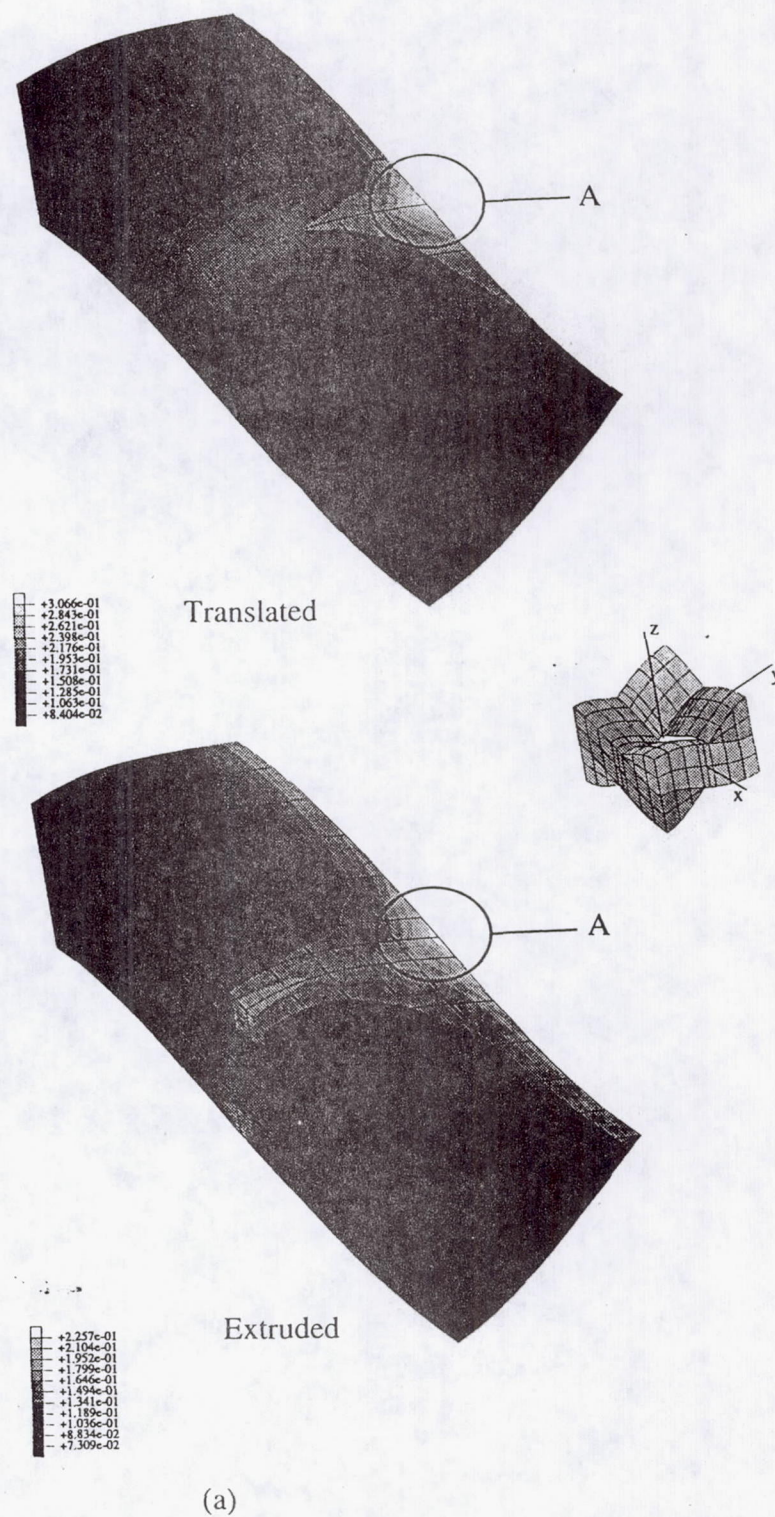
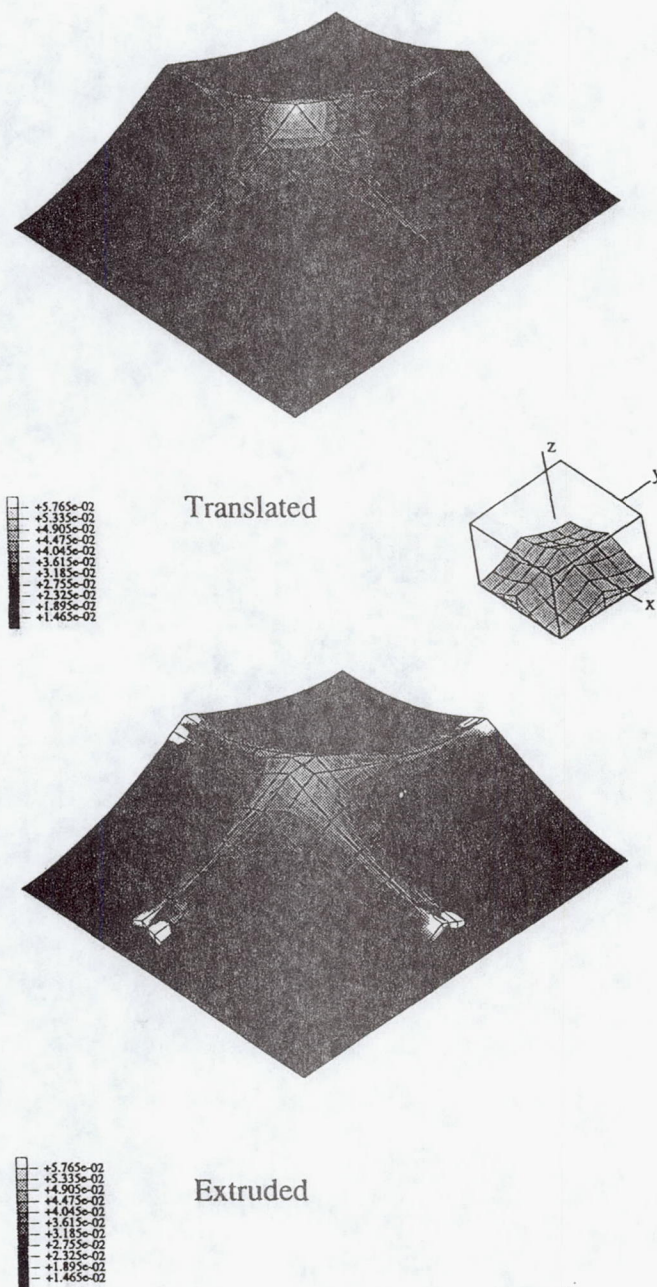


Figure 4.13: Comparison of Tsai-Hill failure criteria predicted with translated and extruded models for (a) tows and (b) resin after being subjected to a 1%  $\epsilon_{xy}$  strain.





(b)

Figure 4.13: (continued)



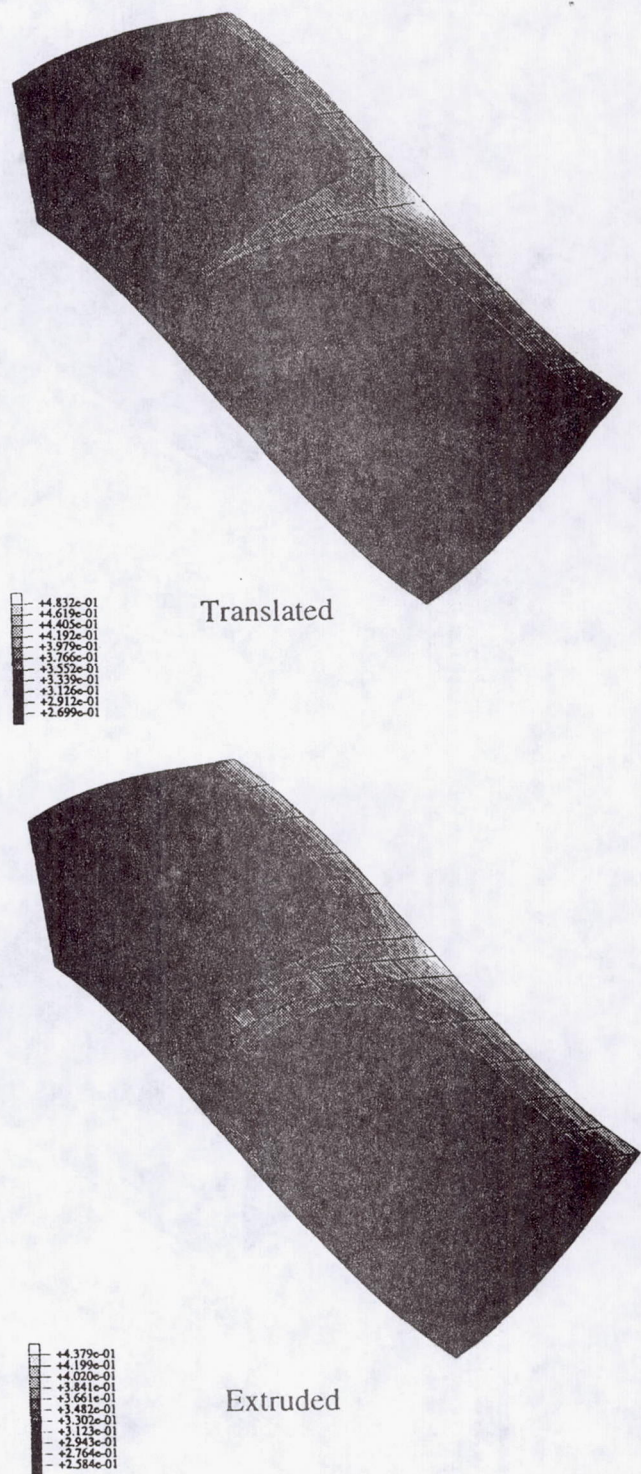
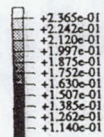
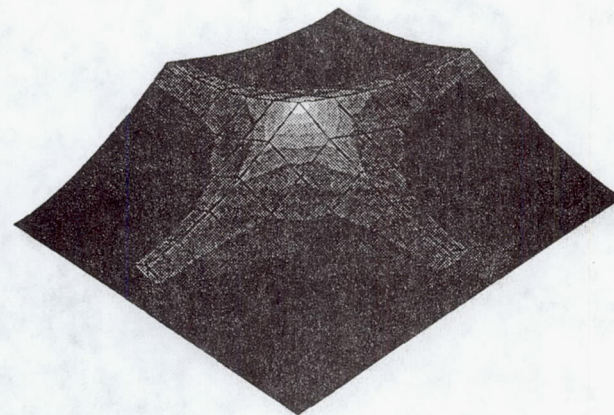
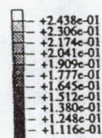
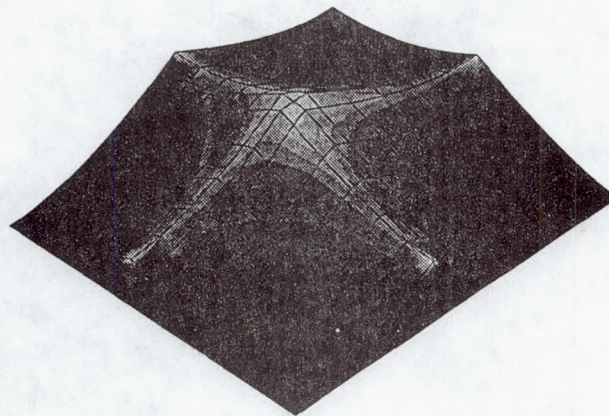


Figure 4.14: Comparison of normalized  $\sigma_{xy}$  distributions in tows of translated and extruded models with  $WR=1/3$  after being subjected to a 1% macroscopic  $\epsilon_{xy}$  strain.





Translated



Extruded

Figure 4.15: Comparison of normalized  $\sigma_{xy}$  distributions in resin of translated and extruded models with  $WR=1/3$  after being subjected to a 1% macroscopic  $\epsilon_{xy}$  strain.



in the translated model which is not present in the extruded model. This stress difference is what is causing the largest difference between the predicted failure of the two models.

The  $\sigma_{yz}$  for the resin is inconsequential compared to the stress levels in the tows. The majority of the tow volume is experiencing stress larger than the highest stress experienced by the resin relative to their strengths so stress distributions in the resin will not be presented. The  $\sigma_{xz}$  for the resin is the same as that for  $\sigma_{yz}$  - just rotated  $90^\circ$  about the  $z$  axis - and will not be presented.

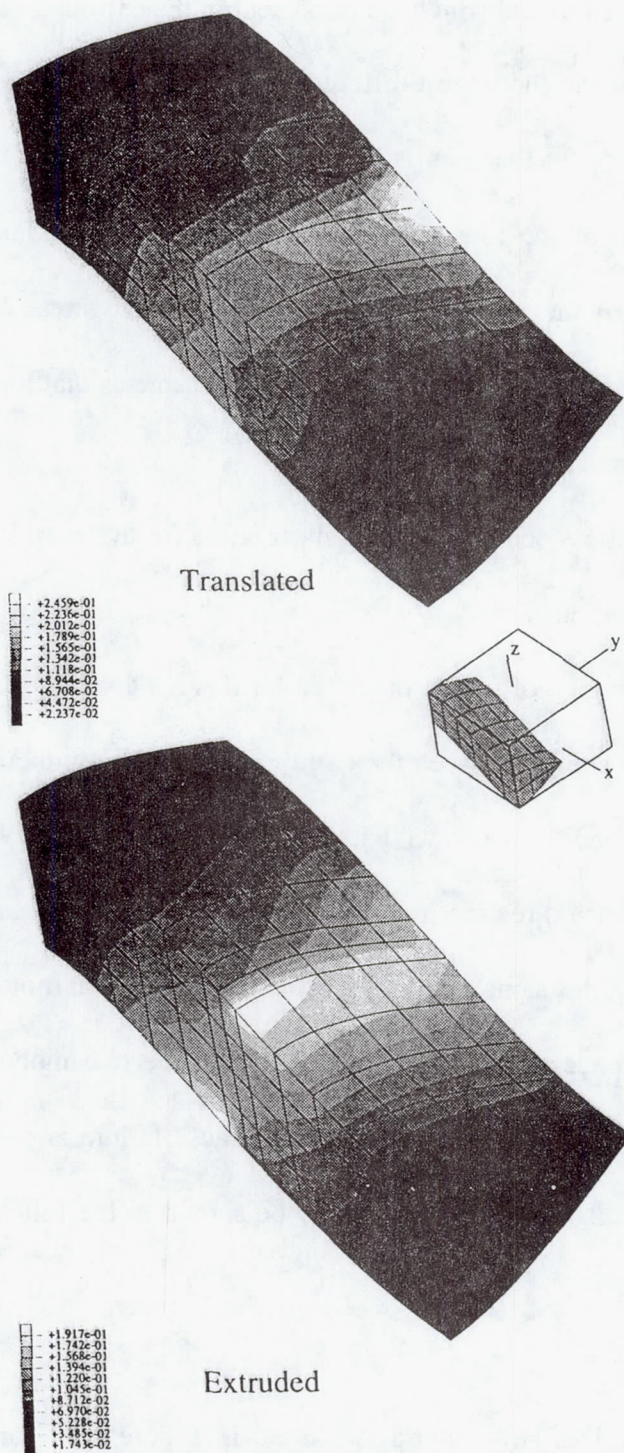
The stress contours for  $\sigma_{xz}$  shear stress for the warp tow is relatively uninteresting and will be skipped.

The region of failure predicted for this XY loading is in the region where the most difference is shown between the two type of modelling, therefore, the greatest amount of difference should be shown with this type of loading. When extensional loading is applied in warp direction, failure is predicted to occur in an area where the models are substantially the same, therefore little difference was noted between the two models. Little difference will also be noted between the two models when a  $\epsilon_{xz}$  shear strain is applied macroscopically to the model because failure is predicted in a region where the models are also very similar, as will be shown in the following section.

### *XZ Loading*

The Tsai-Hill criteria is plotted in Figure 4.17 for the extruded and translated model subjected to a 1%  $\epsilon_{xz}$  macroscopic shear. The figure show that failure is predicted in the resin of both models as indicated by the letter 'A'. The translated model predicts

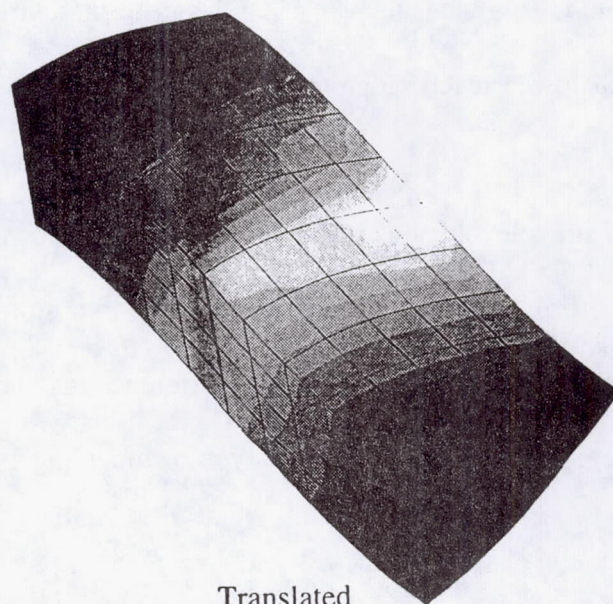




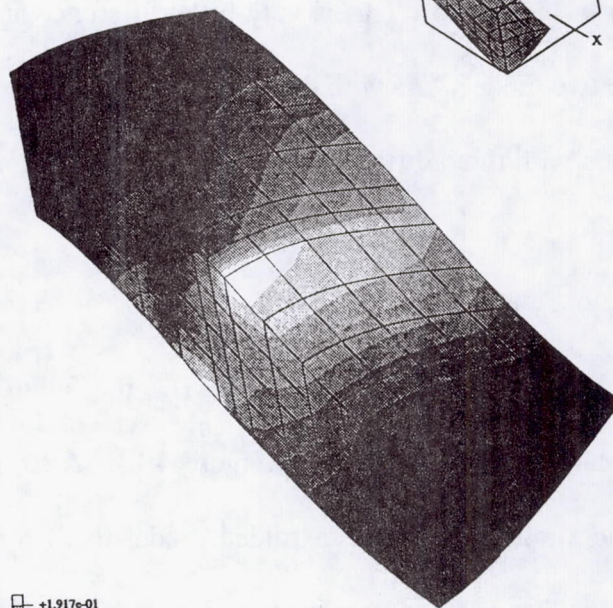
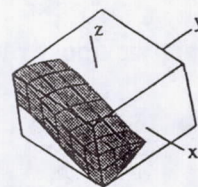
(a) Comparison at different scales

Figure 4.16: Comparison of normalized  $\sigma_{yz}$  distributions in warp tows of translated and extruded models with  $WR=1/3$  after being subjected to a 1% macroscopic  $\epsilon_{xy}$  strain.

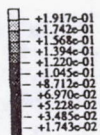




Translated



Extruded



(b) Comparison at same scales

Figure 4.16: (continued)



a failure criterion 4.5% greater than that predicted by the extruded model. Failure will occur at a 2.3% lower macroscopic strain level in the translated model than in the extruded model.

The high stress level is - as stated earlier - in a region where the two models differ very little. Therefore, little difference is noted in the two models. If the stacking of the woven composite were changed, a substantial difference may be noted in the potential for failure of this region and possibly the two type of modeling.

#### 4.2.2 $WR = 1/6$

For this waviness ratio, the difference in the tow volume fraction is less than 1% as indicated in Figure 4.1. This is very little difference and little difference is expected between the two models. As with the above waviness-ratio, the models will be compared for difference with three different loadings: warp extension,  $xy$  shear, and  $xz$  shear.

##### *Loading in Warp Direction*

As with warp extension for  $WR = 1/3$ , the failure for this type of loading will begin in the warp tows as shown in Figure 4.18. Also, failure will initiate at a lower macroscopic strain level in the extruded model than in the translated model by 1.4% below that predicted by the translated model. Recall that for a  $WR$  of  $1/3$ , the difference was 7%. The stresses which contribute most to the failure are again  $\sigma_{x'x'}$  and  $\sigma_{z'z'}$ . There is very little difference in between the maximum and minimum predicted with either loading, and the stress distributions are also very similar, therefore, no distributions will



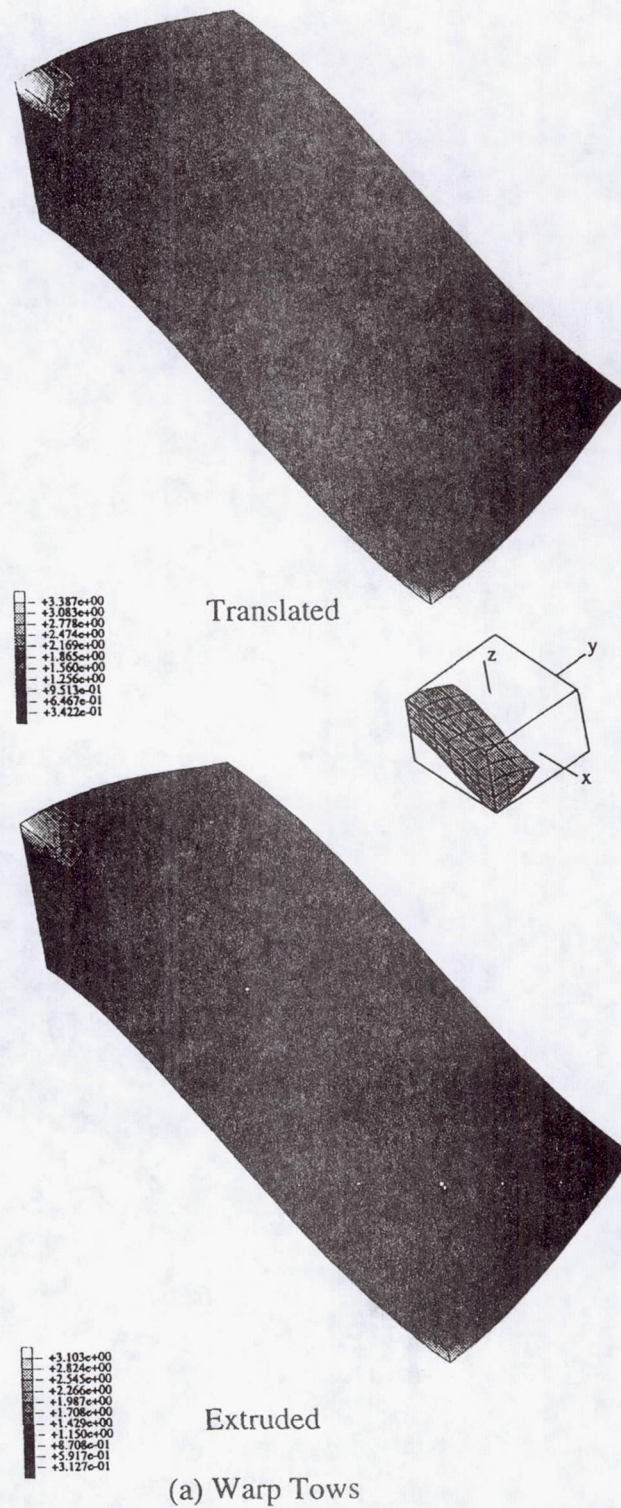
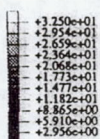
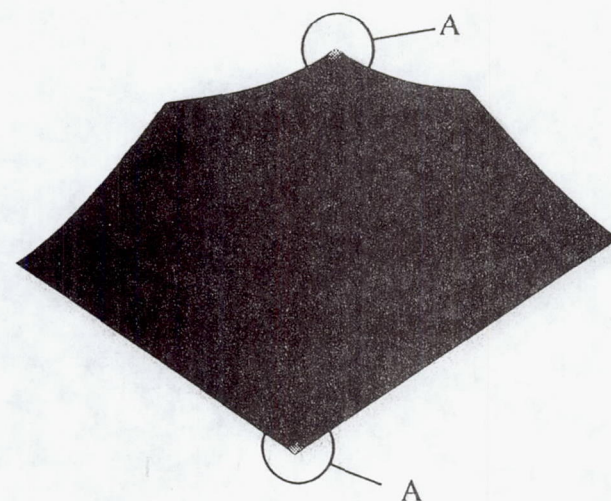
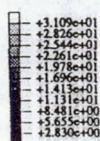
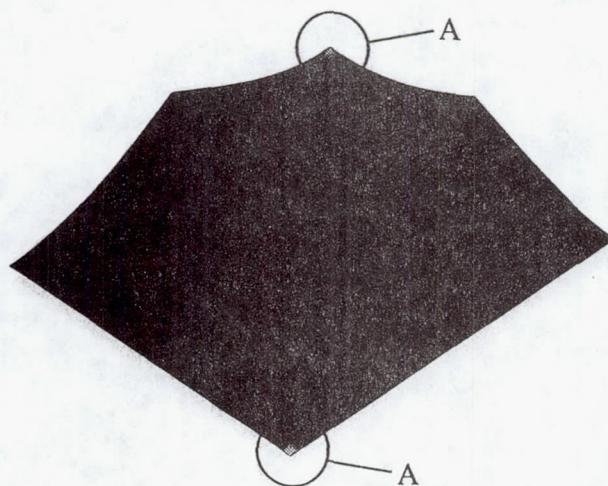
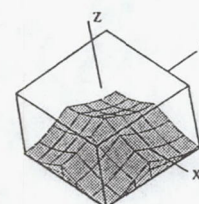


Figure 4.17: Comparison of predicted Tsai-Hill failure criteria for translated and extruded models with  $WR=1/3$  after subjecting RVE to a 1% macroscopic  $\epsilon_{xz}$  strain.





Translated



Extruded

(b) Resin

Figure 4.17: (continued)



be presented for this type of loading.

If this waviness-ratio is compared to the results of  $WR = 1/3$  in the previous section, it can be noted that the  $1/6$ th waviness-ratio can withstand about a 21% larger macroscopic strain than the  $1/3$ rd waviness before failure initiates. This is because the warp tows are not trying to separate as much in the region of failure.

### *XY Loading*

Figure 4.19 shows the Tsai-Hill failure criteria for the two models after subjecting each to a 1%  $\epsilon_{xy}$  shear strain. Failure is again predicted in the center of the tows as it is for  $WR = 1/3$ . For this loading, the extruded model will fail at a macroscopic strain 0.6% less than the translated model. This difference is insignificant.

If the stresses which contribute to failure are examined, the only stress with any significant difference is the  $\sigma_{yz}$  of the warp tow as shown in Figure 4.20. The translated model is still seeing a significant region of stress in the region where the tows cross at 'A'. This is not apparent in the extruded model which predicts a region of high stress near the edge of the fill tow as indicated by the letter 'B'. The separation of the warp tows by resin is still saving the extruded model from significant levels of  $\sigma_{yz}$  stress. Other than this there is no significant difference.

Comparing this waviness-ratio to the  $1/3$ rd waviness above, it is seen that the extruded model will fail sooner at a  $1/6$ th waviness, but the translated will fail first at a  $1/3$ rd waviness for  $xy$  shearing.



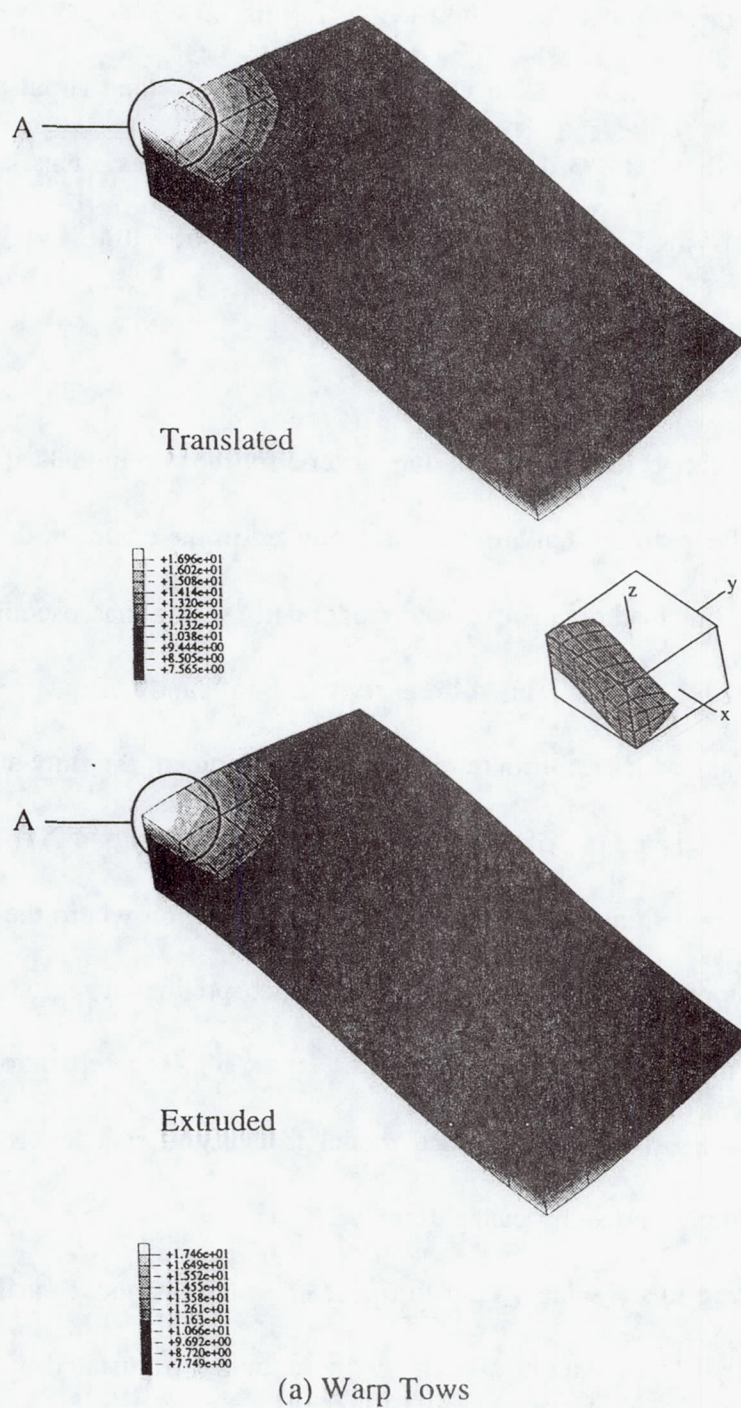
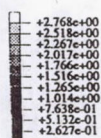
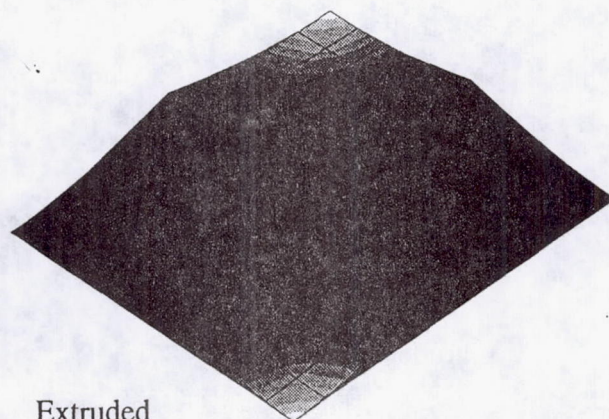
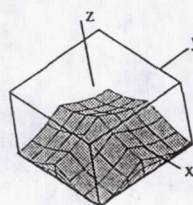
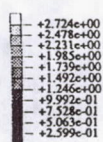
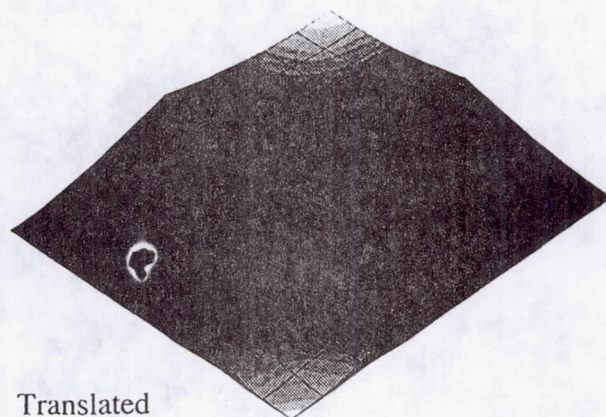


Figure 4.18: Comparison of predicted Tsai-Hill failure criteria for translated and extruded models with  $WR=1/6$  after subjecting RVE to a 1% macroscopic  $\epsilon_{xx}$  strain.

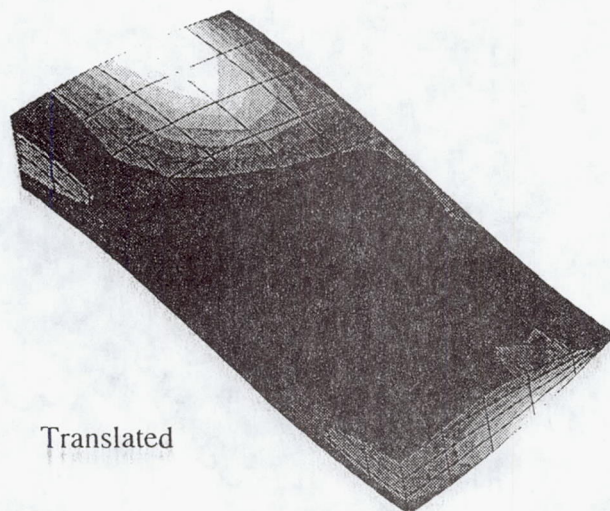




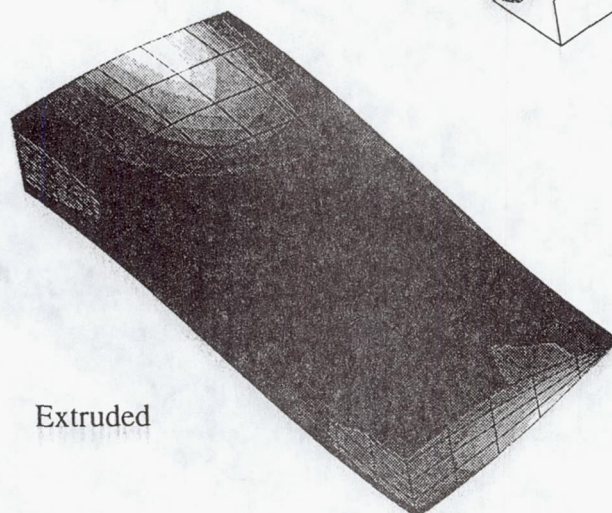
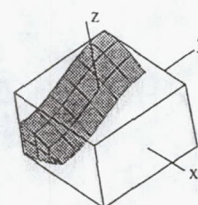
(b) Resin

Figure 4.18: (continued)





+2.500e+00  
+2.398e+00  
+2.295e+00  
+2.192e+00  
+2.090e+00  
+1.987e+00  
+1.884e+00  
+1.782e+00  
+1.679e+00  
+1.576e+00  
+1.474e+00

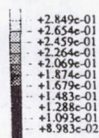
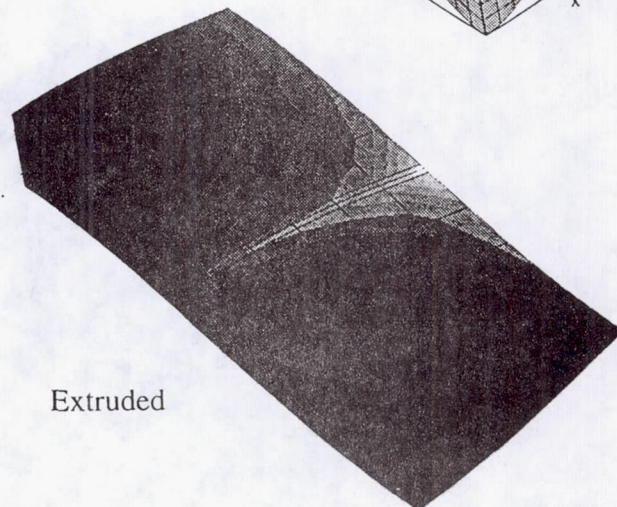
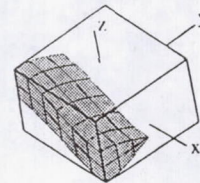
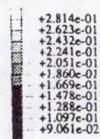
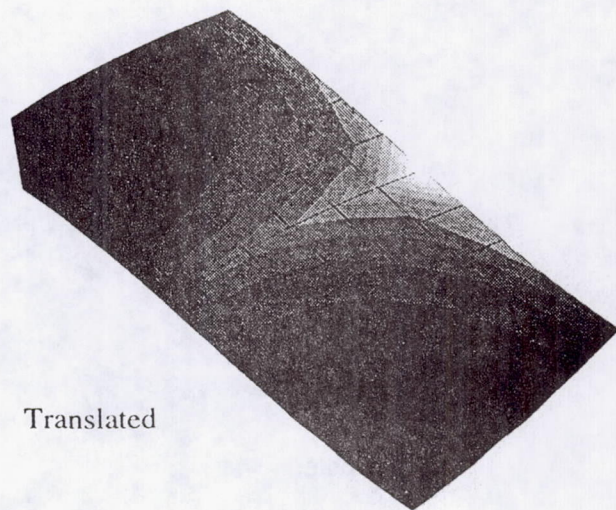


+2.501e+00  
+2.400e+00  
+2.298e+00  
+2.197e+00  
+2.095e+00  
+1.993e+00  
+1.892e+00  
+1.790e+00  
+1.689e+00  
+1.587e+00  
+1.486e+00

(c) Fill Tows

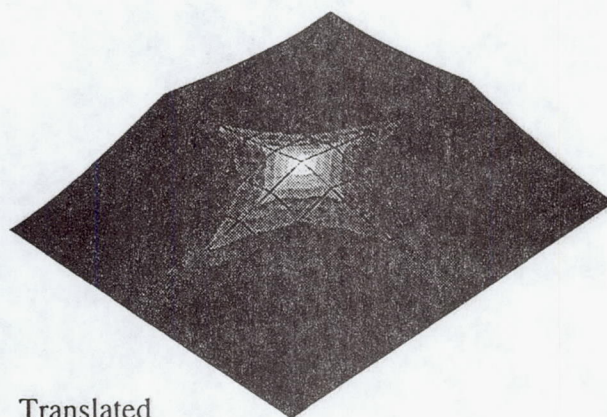
Figure 4.18: (continued)



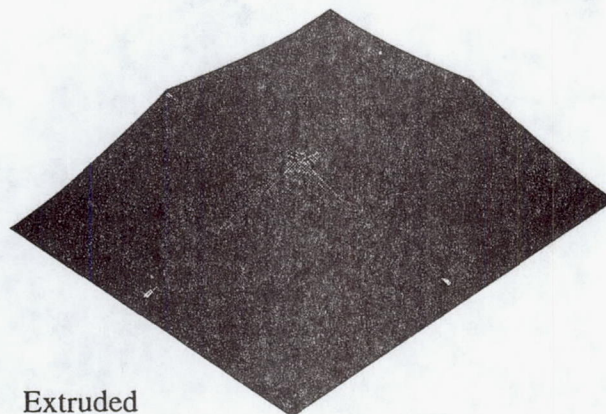
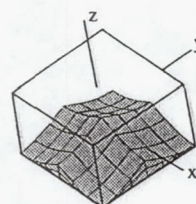
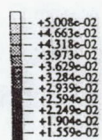


(a) Tows

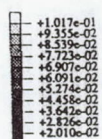
Figure 4.19: Comparison of predicted Tsai-Hill failure criteria for translated and extruded models with  $WR=1/6$  after subjecting RVE to a 1% macroscopic  $\epsilon_{xy}$  strain.



Translated



Extruded



(b) Resin

Figure 4.19: (continued)

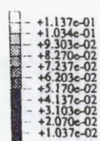
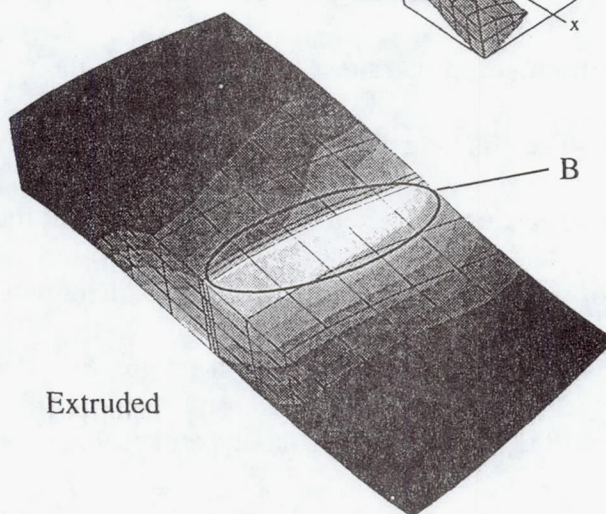
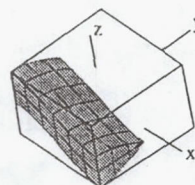
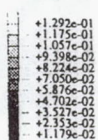
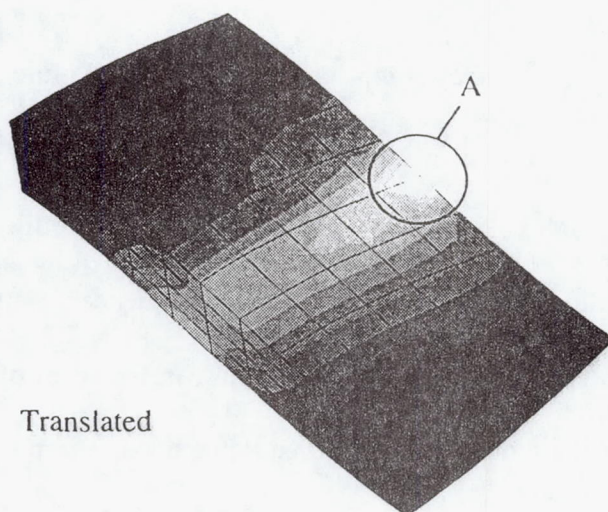


### *XZ Loading*

Figure 4.21 shows plots of the Tsai-Hill failure criteria for the two models subjected to a 1%  $\epsilon_{xz}$  shear strain. Only the resin and warp tow of each model are shown because although notable differences are apparent in the fill tow, the level of the predicted criteria is so low that it would be of no consequence. Note that there is little difference between the two models. Failure will start in the resin of both models as indicated by the levels of the plots. The difference in the maximum predicted by the translated model is 4.5% greater than that predicted by the extruded model. The difference in the applied strain to failure is 2.14% less in the translated model compared to the extruded model. The stress which is the primary cause of failure in this region is  $\sigma_{xz}$ , as it was for  $WR = 1/3$ . The normalized  $\sigma_{xz}$  stress distributions for the resin and warp tow are shown in Figure 4.22. There is little difference in the two distributions with only a 2.3% difference in the maximum stress predicted by the translated over the extruded. Since there is little difference of the models in the region of failure, there will be little difference in the stress distributions there. It is possible that a progressive failure analysis will reveal more differences in the two models for this type of loading.

Again, if the failure at this waviness is compared the 1/3rd waviness, it is seen that the 1/3rd will fail at a macroscopic strain 53.8% lower than the strain required to fail the 1/6th waviness. This is because the maximum angle which the materials in the tows are experiencing is greater in the  $WR = 1/3$ . This is also shown by the predicted moduli of the two waviness ratios. The 1/3 waviness predicts a value which is 12.4% greater than that predicted by the 1/6 waviness. As stated earlier, the failure scenario could





(a) Tows

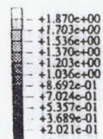
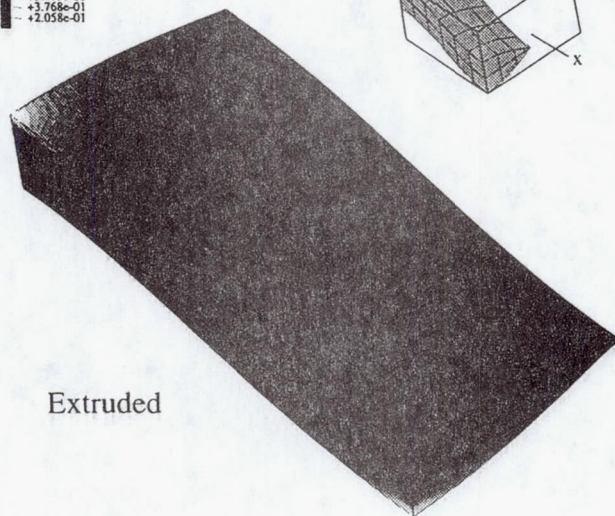
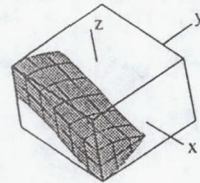
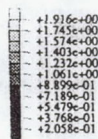
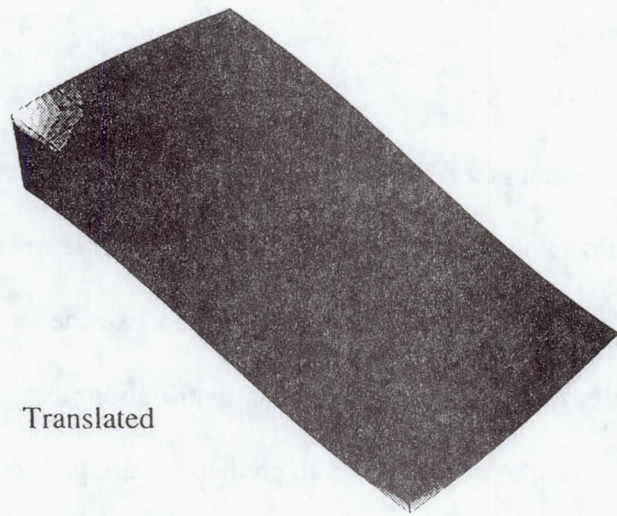
Figure 4.20: Comparison of normalized  $\sigma_{yz}$  distributions in warp tows of translated and extruded models with  $WR=1/6$  after subjecting RVE to a 1% macroscopic  $\epsilon_{xy}$  strain.



change drastically if the mats are simply stacked.

#### 4.2.3 $WR = 1/20$

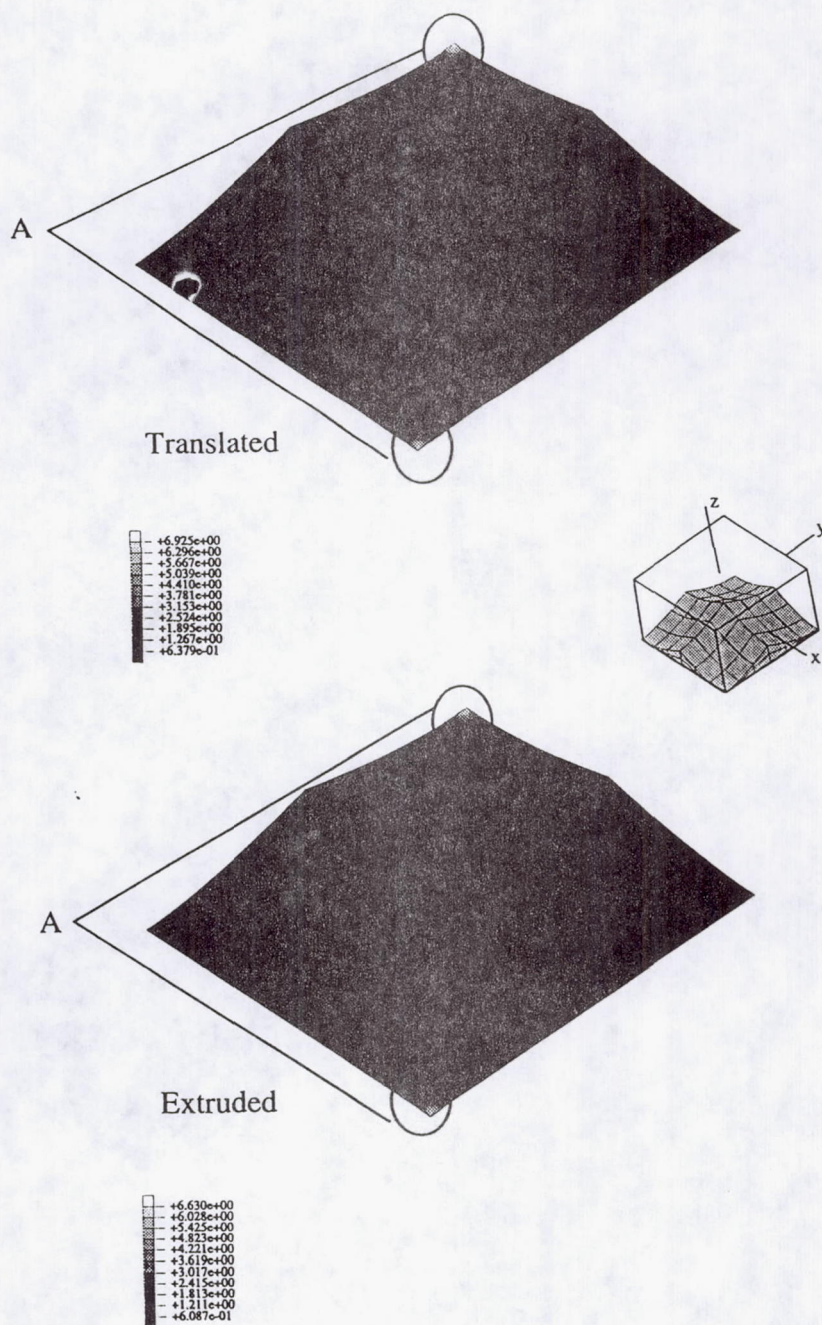
If the amount of difference continues to decrease between the two models as waviness-ratio is decreased, then there should be little or no difference in the predicted stress distributions between the translated and extruded models at this waviness-ratio. Unfortunately, comparison of the stress distributions between the two models was not practical because the extruded model predictions are very poorly due to elements near the edge of the 1/32nd model which have very bad aspect ratios. For this reason, no comparison will be made between the two models at this waviness-ratio.



(a) Warp tows

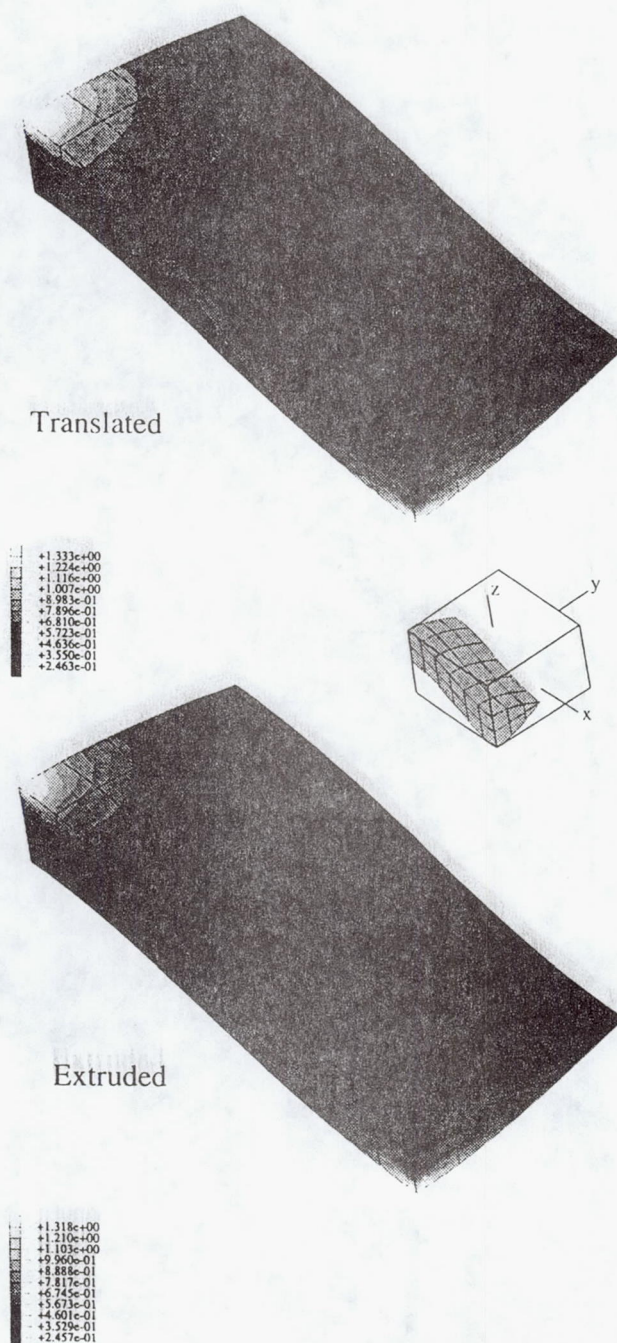
Figure 4.21: Comparison of predicted Tsai-Hill failure criteria for translated and extruded models with  $WR=1/6$  after subjecting RVE to a 1% macroscopic  $\epsilon_{xz}$  strain.





(b) Resin

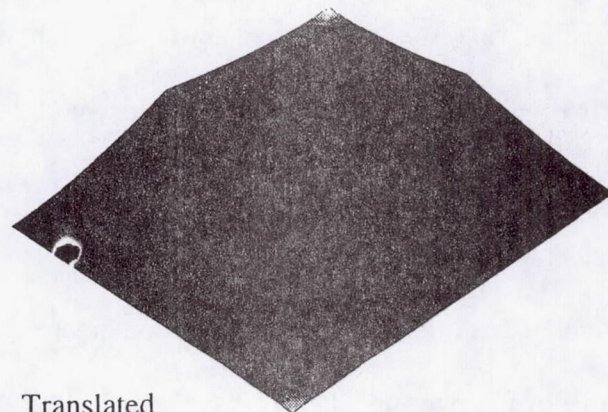
Figure 4.21: (continued)



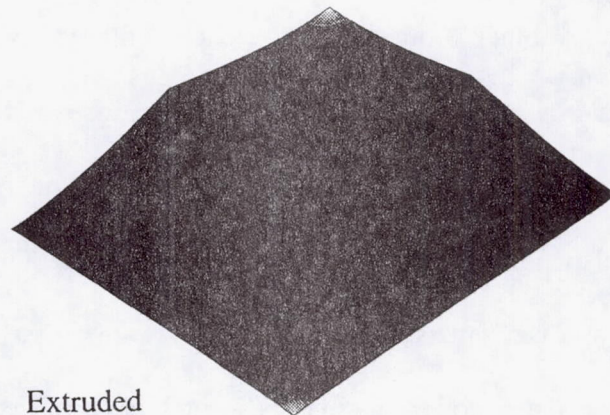
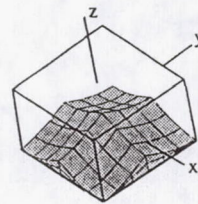
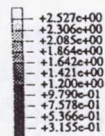
(a) Warp tows

Figure 4.22: Comparison of normalized  $\sigma_{xz}$  distributions of translated and extruded models with  $WR=1/6$  after subjecting RVE to a 1% macroscopic  $\epsilon_{xz}$  strain.

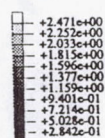




Translated



Extruded



(b) Resin

Figure 4.22: (continued)

## V. CONCLUSIONS

The objective of this study was to determine which model, the extruded or translated, reflects reality better, and whether such extensive modeling is really necessary to adequately represent the material properties associated with woven composites. To do this one must consider what was stated in the previous chapter as well as compare the geometry of each model with that of actual woven composites.

The geometry of the two models both have drawbacks. The translated model, at high waviness ratio, predicts that parallel tows will not be separated by resin. This is the major flaw of the translated model. The extruded model allows for a separation of parallel tows. This difference in behavior is largest when an  $\epsilon_{xy}$  shear strain is applied to the composite. Another geometrical difference is that the translated model predicts a thinning of the middle of the tows at high waviness-ratios which is also not correct. This is shown in the  $\sigma_{xx}$  stress gradients in the warp extension of the two models. The extruded tows also possess some deviation from reality. One is that there is a gap between the fill and warp tows. In reality, the tows are pressed against one another and no resin pockets exist. However, this does not seem to affect the stress distributions predicted with this model. And finally, both models assume a constant cross-section. This may or may not be important and should be pursued in later studies.

For the prediction of elastic moduli, either model is adequate at low waviness ratios. At higher waviness ratios however, the moduli being predicted becomes important. For  $E_z$ , there is such little difference - with due respect to the material system used in this analysis - and either model will predict values within 1% of the other. Even if a very



coarse mesh is used, there is little difference in the predicted moduli. If a high degree of accuracy is not required, then either model is adequate for  $E_x$ ,  $G_{xy}$ ,  $G_{xz}$  and the Poisson's ratios  $\nu_{xy}$  and  $\nu_{xz}$ . However, for greater accuracy, the extruded model gives a better geometric model of reality and should be used.

When stress distribution are desired, the region of interest is of primary importance in selecting one or the other model. If there is little geometric difference between the two models in the area of interest, then either model will be adequate. This was shown for extension in the warp direction and XZ shear at  $1/6$  and  $1/3$  waviness-ratios. However, if there is a substantial difference in the geometry of the region of interest, then the extruded model should provide a better approximation due to its superior modeling of reality compared to the translated model. At very low waviness-ratios, the translated model must be used unless significant refinement of the mesh is possible to eliminate bad element aspect ratios. The difference in the two models is very minor at very low waviness and either model should be adequate for stress distributions.

## VI. FUTURE WORK

The chapter narrates briefly on future research which this study has shown to be important. This study dealt with the effect of only one of many possible assumed configurations which a researcher may make. It would be fruitful to study the effect of other geometry changes on the predictions made using either numerical or analytical techniques. Some possible geometry configurations concerned with plain weaves which may be examined are: the effect of how mats are stacked, nesting of the mats, unbalanced weave configurations, different waviness ratios for fill and warp tows, cross-section shape, and non-sinusoidal tow paths. Satin weaves and other braids would also be interesting to study, but very difficult due to the size of the unit cells involved for three dimensional study.

Another aspect of woven composites which would be interesting to study is the effect changes in the materials as the composite is loaded. As the composite is loaded, the tows do undergo some amount of rotation at points inside the tow. It would be interesting to see how much of an effect this would actually cause on the predicted stress-strain curve of the composite.

Progressive failure of plain weaves would also be of interest. In this study, very localized regions of failure were predicted for XZ shear loading and very little difference was predicted between to two types of modeling. A progressive failure analysis might reveal substantial differences if it were studied.



## REFERENCES

1. Ishikawa, T. and T.-W. Chou. 1982. "Stiffness and strength behavior of woven fabric composites," *Journal of Material Science*, 17:3211-3220.
2. Whitcomb, J. D. 1991. "Three-Dimensional Stress Analysis of Plain Weave Composites," *Composite Materials: Fatigue and Fracture (Third Volume)*, ASTM STP 1110, T. K. O'Brien, Ed., Philadelphia: American Society for Testing and Materials, pp. 417-438.
3. Byun, J.-H. and T.-W. Chou. 1989. "Modelling and characterization of textile structural composites: A review," *Journal of Strain Analysis*, 24:253-262.
4. Naik, N. and P. Shembekar. 1992. "Elastic behavior of woven fabric composites: I - Lamina Analysis," *Journal of Composite Materials*, 26(15):2196-2225.
5. Whitcomb, J.D. and K. Woo. 1992. "Enhanced Direct Stiffness Method for Finite Element Analysis of Textile Composites," *CMC Report No. 92-17*, Texas Engineering Experiment Station, Texas A&M University.
6. Masters, J. E., R. L. Foye, C. M. Pasotre, and Y. A. Gowayed. 1992. "Mechanical properties of triaxially braided composites: Experimental and Analytical results," *NASA Contractor Report 189572*, Langley Research Center.
7. Paumelle, P., A. Hassim, and F. Léné. 1990. "Composites with Woven Reinforcements: Calculation and Parametric Analysis of the Properties of the Homogeneous Equivalent," *La Recherche Aéronautique*, 1:1-12.
8. Woo, K. 1993. *Stress and failure analysis of textile composites*, Ph.D. Dissertation, Department of Aerospace Engineering, Texas A&M University.
9. Mura, T. 1987. *Micromechanics of defects in solids*, 2nd edn., Dordrecht: Martinus Nijhoff.
10. Jones, R. M. 1975. *Mechanics of Composite Materials*, New York: McGraw-Hill.
11. Agarwal, B. D. and L. J. Broutman. 1990. *Analysis and Performance of Fiber Composites*, New York: Wiley Interscience.
12. Ishikawa, T. 1981. "Anti-symmetric elastic properties of composite plates of satin weave cloth," *Fiber Science Technology*, 15:127-145.
13. Ishikawa, T. and T.-W. Chou. 1982. "Elastic behavior of woven hybrid



- composites," *Journal of Composite Materials*, 16:2-19.
14. Ishikawa, T. and T.-W. Chou. 1983. "In-plane thermal expansion and thermal bending coefficients of fabric composites," *Journal of Composite Materials*, 17:92-104.
  15. Ishikawa, T. and T.-W. Chou. 1983. "Non-linear behavior of woven fabric composites," *Journal of Composites Materials*, 17:399-413.
  16. Ishikawa, T. and T.-W. Chou. 1983. "Thermoelastic analysis of hybrid fabric composites," *Journal of Material Science*, 18:2260-2268.
  17. Ishikawa, T. and T.-W. Chou. 1983. "One dimensional micro-mechanical analysis of woven fabric composites," *AIAA Journal*, 21:1714-1721.
  18. Ishikawa, T., M. Matsushima, Y. Hayashi, and T. Chou. 1985. "Experimental confirmation of the theory of elastic moduli of fabric composites," *Journal of Composite Materials*, 19:443-458.
  19. Naik, N. K. and P. S. Shembekar. 1992. "Elastic behavior of woven fabric composites: II - Laminate Analysis," *Journal of Composite Materials*, 26(15):2226-2246.
  20. Avery, William B. and Carl T. Herakovich. 1987. *A Study of the Mechanical Behavior of a 2D Carbon-Carbon Composite*. Virginia Polytechnic Institute and State University, Interim Report 66. Blacksburg, Virginia.
  21. Foye, R. L. 1988, "The Mechanics of Fabric-Reinforced Composites," *Fiber-Tex 1988*. NASA Conference Publication 3038.
  22. Woo, K. and J.D. Whitcomb. 1992. "Macro Finite Element Using Subdomain Integration," *OTRC Report 03/92-A-29-100*, Texas A&M University.
  23. Whitcomb, J. D., K. Woo, and S. Gundapaneni. 1992. "Macro Finite Element for Analysis of Textile Composites," *CMC Report No. 92-16*, Texas Engineering Experiment Station, Texas A&M University.
  24. Paumelle, P., A. Hassim, and F. Léné. 1991. "Microstress Analysis in Woven Composite Structures," *La Recherche Aérospatiale*, 6:47-62.
  25. Ma, C.-L., J.-M. Yang, and T.-W. Chou. 1986. "Elastic Stiffness of Three-Dimensional Braided Textile Structural Composites," *Composite Materials: Testing and Design (Seventh Conference)*, ASTM STP 893, J.M. Whitney, Ed., American Society of Testing and Materials, pp. 404-421.



## VITA

CLINTON DANE CHAPMAN graduated from high school at Pine Tree High School in Longview, Texas in 1986 then went on to Texas A&M University and completed a B.S. in Aerospace Engineering in 1990. After graduation, he worked as a mechanical design engineer and programmer at a small company in San Antonio called ALCOR. A year later, he went back to school at Texas A&M to get his M.S. in Aerospace Engineering while continuing consulting work at ALCOR. After completion of his M.S., the author plans to pursue his Ph.D. at Texas A&M.

To contact the author, please write to:

Clinton D. Chapman  
1605 Springdale  
Longview, Texas 75604



REPORT DOCUMENTATION PAGE			Form Approved OMB No. 0704-0188	
Public reporting burden for this collection of information is estimated to average 1 hour per response, including the time for reviewing instructions, searching existing data sources, gathering and maintaining the data needed, and completing and reviewing the collection of information. Send comments regarding this burden estimate or any other aspect of this collection of information, including suggestions for reducing this burden, to Washington Headquarters Services, Directorate for Information Operations and Reports, 1215 Jefferson Davis Highway, Suite 1204, Arlington, VA 22202-4302, and to the Office of Management and Budget, Paperwork Reduction Project (0704-0188), Washington, DC 20503.				
1. AGENCY USE ONLY (Leave blank)	2. REPORT DATE April 1994	3. REPORT TYPE AND DATES COVERED Final Contractor Report		
4. TITLE AND SUBTITLE Effects of Assumed Tow Architecture on the Predicted Moduli and Stresses in Woven Composites		5. FUNDING NUMBERS  WU-505-62-10 G-NAG3-1270		
6. AUTHOR(S)  Clinton Dane Chapman				
7. PERFORMING ORGANIZATION NAME(S) AND ADDRESS(ES)  Texas A&M University College Station, Texas 77843		8. PERFORMING ORGANIZATION REPORT NUMBER  E-8722		
9. SPONSORING/MONITORING AGENCY NAME(S) AND ADDRESS(ES)  National Aeronautics and Space Administration Lewis Research Center Cleveland, Ohio 44135-3191		10. SPONSORING/MONITORING AGENCY REPORT NUMBER  NASA CR-195310		
11. SUPPLEMENTARY NOTES  Project Manager, Christos C. Chamis, Structures Division, organization code 5200, NASA Lewis Research Center, (216) 433-3252.				
12a. DISTRIBUTION/AVAILABILITY STATEMENT  Unclassified - Unlimited Subject Category 24		12b. DISTRIBUTION CODE		
13. ABSTRACT (Maximum 200 words)  This study deals with the effect of assumed tow architecture on the elastic material properties and stress distributions of plain weave woven composites. Specifically, the examination of how a cross-section is assumed to sweep-out the tows of the composite is examined in great detail. The two methods studied are extrusion and translation. This effect is also examined to determine how sensitive this assumption is to changes in waviness ratio. 3D finite elements were used to study a T300/Epoxy plain weave composite with symmetrically stacked mats. 1/32nd of the unit cell is shown to be adequate for analysis of this type of configuration with the appropriate set of boundary conditions. At low waviness, results indicate that for prediction of elastic properties, either method is adequate. At high waviness, certain elastic properties become more sensitive to the method used. Stress distributions at high waviness ratio are shown to vary greatly depending on the type of loading applied. At low waviness, both methods produce similar results.				
14. SUBJECT TERMS  Properties; Stresses; Extrusion; Translation waviness ratio; 3D finite element			15. NUMBER OF PAGES 147	
			16. PRICE CODE A07	
17. SECURITY CLASSIFICATION OF REPORT Unclassified	18. SECURITY CLASSIFICATION OF THIS PAGE Unclassified	19. SECURITY CLASSIFICATION OF ABSTRACT Unclassified	20. LIMITATION OF ABSTRACT	